CHAPTER 17

WINDS

Section 17.1	**D.D. Grantham and I.I. Gringorten**
Section 17.2 and 17.3	**A.E. Cole and A.J. Kantor**
Section 17.4	**I.I. Gringorten and P.I. Tattelman**
Section 17.5	**F.A. Marcos**

The atmosphere's motions defy rigorous classification or modeling. The application of a particular feature of wind structure to a given engineering problem should be dictated by its physical dimensions. Extrapolation of data beyond its indicated limitations is risky. Local conditions may not always be well represented by the data in this chapter, and may produce extreme wind variations in excess of those presented, even when the local wind structure is free from perturbations such as fronts, thunderstorms, or squalls. The practicing engineer should avail himself of applicable local meteorological records whenever possible. Information other than that given below is available through the various national weather services and the World Meteorological Organization [NOCD, 1980]. Special studies prepared by Environmental Technical Applications Center (ETAC) or Air Force Geophysics Laboratory (AFGL) might provide the best answers for specific design problems.

The measure of wind, in speed and direction, presents an immediate problem in the time interval for the observation. A conventional observation of wind speed is the wind travel in 1 min, 5 min, or 1 h, that is, the 1-min, 5-min, or 1-h average. The current standard averaging time period in the United States is 1 min. In England and Canada a 10-min period is customary when wind speed records are available, otherwise the averaging period is something over 15 s. However, in published climatic data, hourly (60 min) averaged winds are often given.

As might be expected, the variance of the 1-min wind is greater than the 5-min, which in turn is greater than that of the 1-h wind, but not significantly so. On the other hand, wind speeds of shorter duration than 1 min are subject to significantly greater variability. When the wind speeds peak between lulls, in 20 s or less, they are conventionally termed *gusts*.

17.1 WIND AS A FUNCTION OF HEIGHT

A major problem with pooling the various surface wind observations is in the determination of the best method or model for adjusting wind speeds to a common height above the surface. Once established, however, the model formula can be used to describe wind speed and gusts along a vertical profile in the lowest 50 or 100 m of the atmosphere.

Wind flows in response to pressure gradients in the atmosphere. Such pressure gradients change slowly with altitude, negligibly within the first 100 m. Yet the changes in wind speed with height are pronounced. Air motion near the surface does not obey the simple pressure gradient law. Anemometers near the ground may be hardly turning, whereas those on tall buildings or towers may show moderately strong, gusty winds. Kites may be difficult to launch, but once several hundred feet high, they may fly without difficulty.

Friction caused by terrain is one of the main factors affecting the horizontal wind speed up to an altitude known as the gradient level. At this height, 300 or 600 m, the pressure gradient is said to be dynamically balanced against two other influences: the earth's rotation and the curvature of the wind path. A theoretical wind speed that closely approximates the observed wind at gradient height can be computed from the isobaric spacing and curvature on surface weather maps.

The height of the gradient level and the velocity profile up to that level vary greatly, mainly with the type of surface and the stability of the air. Stability is chiefly a function of the temperature structure in the boundary layer. One extreme of temperature structure is represented by a super adiabatic lapse rate in which temperature decreases rapidly with altitude so that air displaced upward will continue upward because it is warmer than its surroundings. The opposite extreme is a negative lapse rate or inversion, in which temperature increases with height, so that air displaced upward is cooler than its surroundings and tends to sink back to its original level. A neutral condition (adiabatic) exists when the temperature lapse rate is such that a parcel of air displaced vertically will experience no buoyant acceleration. In general, a neutral lapse rate is established by the turbulent mixing caused by strong winds at the surface.

A popular model for the shift of wind speed and direction with altitude in the boundary layer, originally developed for ocean depth, is termed the Ekman Spiral. Since its introduction, micrometeorologists have studied the energy trans-

Table 17-1. Ratio of wind speed at height H to speed at 91 m over open prairie obtained during the Great Plains Turbulence Field program.

H (meters)	Lapse Rate (dt/dz < 0)	V_H/V_{91} Inversion (dt/dz > 0)	Isothermal (dt/dz = 0)
91	1.000	1.000	1.000
30	0.965	0.689	0.872
21	0.944	0.608	0.829
15	0.915	0.538	0.792
9	0.866	0.452	0.733
6	0.825	0.403	0.686
3	0.749	0.339	0.604
1.5	0.662	0.275	0.518
0.6	0.556	0.231	0.424
0.3	0.470	0.200	0.336
0.15	0.383	0.166	0.300

fer and diffusion phenomena in the boundary layer and have found improved empirical relationships to fit wind speed data gathered at various heights above ground. Table 17-1 shows the ratio of wind speed at various heights to that at 91 m over open prairies. Values are based on actual wind measurements taken during the Great Plains Turbulence Field Program conducted at O'Neill Nebraska [Lettau and Davidson, 1957]. The ratios are shown for typical daytime lapse rates (dT/dz < 0), night-time (dT/dz > 0) and for isothermal conditions (dT/dz = 0).

17.1.1 Variation of Wind Speed with Height (Lowest 100 m)

Two alternative classes of models have been used to estimate the increase of wind speed with height: *logarithmic* and *power* models.

In one logarithmic model

$$\frac{V}{V_1} = \ell n\frac{(1 + H)}{H_o} / \ell n\frac{(1 + H_1)}{H_o} \qquad (17.1)$$

V is the mean wind speed at height H, V_1 is the mean wind speed at the reference level H_1 (anemometer level), and H_o is the *roughness parameter* a length determined by the characteristic ground surface. The boundary condition at H = 0 is V = 0. This model has the advantage that the effect of terrain is included explicity. Typical values for H_o are given in Table 17-2. Table 17-3 lists V/V_1 for a variety of roughness parameters H_o, for two reference levels, and for various heights H.

In the simplest power model the mean wind speed V at height H is approximated by

Table 17-2. Typical values of the roughness parameter, H_o.

Type of Surface	H_o (cm)
Smooth (mud flats, ice)	0.0009
Lawn, grass up to 1 cm	0.09
Downland, thin grass up to 10 cm	0.61
Thick grass, up to 10 cm	2.25
Thin grass, up to 240 cm	4.9
Thick grass, up to 240 cm	9.1

$$\frac{V}{V_1} = \left(\frac{H}{H_1}\right)^p \qquad (17.2)$$

where the exponent p depends on the height, terrain, thermal stratification and speed of the overall airflow. The parameter p is larger for rough ground, for altitudes below H_1, and for relatively small V_1. It varies within limits, approximately 0.05 to 0.8, and averages between 0.1 and 0.3. Table 17-4 lists mean values of p, determined for several locations and two types of terrain. Table 17-5 lists mean values of p that were determined for typical daytime (dT/dz < 0) night-time (dT/dz > 0), and isothermal conditions in the lowest 9 m over open prairie country (Great Plains Turbulence Field Program). The exponent p is larger when there is a stabilizing inversion and smaller when there is a positive lapse rate. According to Sherlock [1952] a typical value for p is 1/7 (or 0.143). Early workers had recognized that his p-value was applicable to typical steady or mean winds but not applicable to gustiness. Sherlock [1952] noted that gusts were better described with a value of p = 0.0625. Shellard [1965], in reducing high wind speeds and gusts to a common height of 10 m, used Equation (17.2) with p = 0.17 for mean speeds and 0.085 for gusts.

A special study was made with data from the Windy Acres Project [Izumi, 1971] consisting of 39 h of 1-s wind

Table 17-3. Ratios of wind at height H to wind at height H_1 for two reference levels and three roughness parameters H_o, calculated by Equation (17.1).

H (m)	H_o = 30 cm	H_o = 3 cm	H_o = 0.3 cm
	V/V_1 for H_1 = 6 m		
100	1.91	1.53	1.37
10	1.16	1.10	1.07
1	0.48	0.67	0.76
0.5	0.32	0.54	0.67
	V/V_1 for H_1 = 3 m		
100	2.42	1.76	1.51
10	1.47	1.26	1.17
1	0.61	0.77	0.84
0.5	0.41	0.62	0.74

Table 17-4. Mean values for heights ranging from 10 to 100 m of exponent p in Equation (17.2).

Location and Terrain	p
Fairly Level Open Country	
Ann Arbor, Michigan	0.14
Sale, Victoria, Australia	0.16
Cardington, Bedfordshire, England	0.17
Leafield, Oxfordshire, England	0.17
Fairly Level Wooded Country	
Quickborn, Germany	0.23
Upton, Long Island, New York	0.26
Akron, Ohio	0.22

speeds, taken in the summer of 1968, at 8 heights on a 32 m tower in southeast Kansas. The terrain was very flat and partly covered with wheat stubble 16 to 22 cm tall. The 1-s wind was never more than 15.3 m/s, Figure 17-1 (right side) presents resulting isopleths of p as a function of windspeed, from 1-s winds including gusts to 1-h integrated wind speeds. The exponents p were found for wind speeds of the same probability, from level to level, as opposed to the mean wind speed. Nevertheless previous results were supported. There is a systematic decrease of p, from 0.7 down to 0.12, with increasing wind speed for either 1-s, 1-min, 5-min or 1-h winds, when the lower 90% of the wind speeds are considered. For winds equal to or greater than the 90th percentile, the exponent p is almost uniform at 0.12 except for gusts or short-duration winds of 1 min or less. The Windy Acres winds became turbulent above the 95% speeds. In gusts, the value of p varies from 0.11 down to 0.08, suggesting a tendency toward a common speed throughout the turbulent layer.

Equation (17.2) can be used to standardize the height of the wind data of individual stations to one level even though they have differing anemometer levels. In the publication "Climatic Extremes for Military Equipment" [MIL-STD-210B] the value of the exponent p was adopted at 0.125 when the wind is strong but steady, and at 0.08 when the wind is strong and gusty.

The validity of a wind extrapolation to another height is dependent on the representativeness of the wind measurement at the reference level. If the anemometer mast is in a poorly defined terrain, the use of the wind profile formula is questionable. Uniformity of the terrain would improve the result. Winds observed with a land-based anemometer cannot be used to estimate the wind speed over an adjacent water surface. In certain cases the wind speed over terrain may attain a maximum speed at a level significantly below 100 m. Such cases usually occur in cold air flow, for example, nocturnal down-slope winds or sea breezes.

Table 17-5. Mean values of exponent (p) for the lowest 9 m in Equation (17.2), determined from wind profile measurements.

H (m)	p		
	Lapse Rate (dt/dz < 0)	Inversion (dt/dz > 0)	Isothermal (dt/dz = 0)
9.0	0.11	0.38	0.14
4.6	0.13	0.31	0.16
0.9	0.18	0.23	0.21

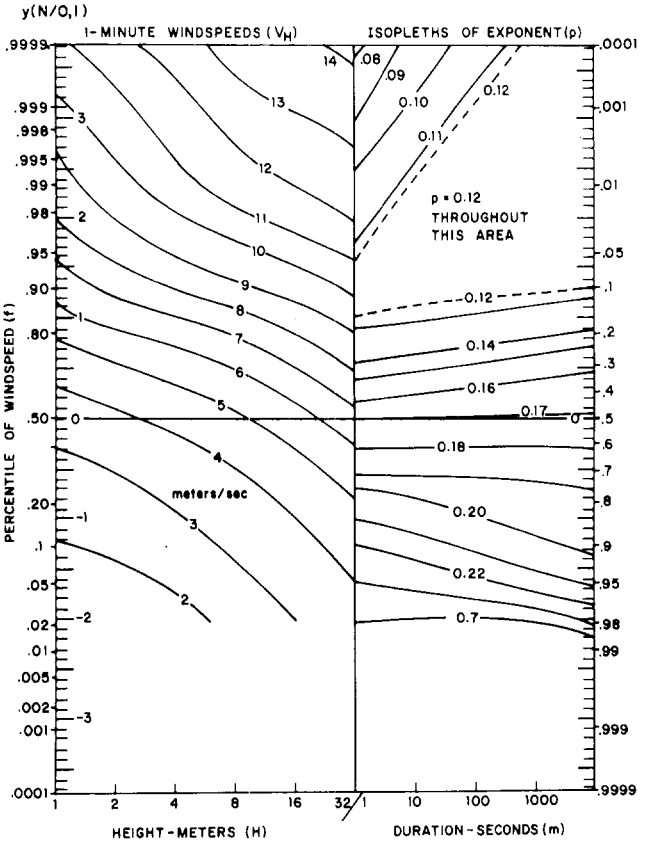

Figure 17-1. A nomogram to obtain windspeeds of duration 1 to 1000 s at a height of 1 to 32 m. (The right hand side of the Nomogram shows the exponent (p) in the wind power model (Equation 17.2) as a function of the duration of the wind, including 1-s, 1-min, 5-min, and 1-h averages, and as a function of the strength of the wind (in percentiles). Left-hand side shows percentiles of 1-min windspeed as a function of height above ground level.)

17.1.2 Wind Direction Shifts (Below 3000 m)

Normally wind direction changes with height. Changes in direction with height are termed veering if the wind turns clockwise and backing if the wind turns counter clockwise. Veering is usually expressed as the rate of turning in degree per height intervals (negative for backing).

Wind direction shifts with height are caused by surface frictional effects and by height changes of the horizontal pressure patterns controlling the mean airflow. The following discussion excludes such phenomena as slope winds, land and sea breezes, nocturnal low-level airflow conditions in the equatorial zone, and rapid, small-scale wind fluctuations.

In the free atmosphere, the mean horizontal airflow is a gradient wind, approximately parallel to the isobars, the lower pressure being to the left. Surface friction reduces the speed, causing a component of the surface wind to blow across the isobars toward lower pressure. Thus the wind direction changes with height to align itself with the gradient wind in the free atmosphere.

To a first approximation, it can be said that under strong mean wind conditions in the Northern Hemisphere, the winds will veer with height in the lower 1000 m, the magnitude of the veering being determined by the intensity of thermal advection processes. Warm air advection increases veering, and cold air advection either decreases the magnitude of frictional veering or causes backing of the winds. The conditions for veering and backing are reversed in the Southern Hemisphere. North of approximately 20°N latitude, winds in the lowest 1000 m of the atmosphere will usually display varying degrees of veering with relatively few cases of backing. Southerly surface winds will veer more with height than northerly surface winds. Above approximately 1000 m, southerly winds will continue to veer with height, while northerly winds will begin to show backing with height.

Tables 17-6, 17-7 and 17-8 indicate the order of magnitude of veering with associated general meteorological conditions. Because no advection is permitted for the situation described in Table 17-6, the veering with height is almost constant and represents the gradual decrease of the surface frictional effect with height. Once the gradient level of the free atmosphere is reached, frictional effects and hence veering become negligible in the case of no advection. Strong surface winds generally make an angle with the gradient wind of 10° to 30°; this is the overall veering found in the frictional layer of the atmosphere when little or no advection exists. The direction of the surface wind is insignificant. Total veering over the entire layer of frictional influence depends primarily on the roughness characteristics of the earth surface: the average for oceans is 5° to 15°, for continents, 25° to 45°. The average veering is usually greater in winter than in summer, and greater at northern stations than at southern stations. The averaging process masks the variability of veering that would be encountered with isolated observations in time and space. In the first 1000 m of the atmosphere, however, the importance of the general direction of the surface wind in obtaining reasonable estimates of veering appears doubtful. Above this layer southerly winds veer with height, northerly winds back with height. Maximum values of veering in the frictional layer are near 3°/30 m; isolated cases of backing of the same order of magnitude are observed.

In summary, the average total veering (or backing) in the lower 1000 m is 20° to 40°, with isolated cases of 70° to 90°. To a first approximation, it may be assumed that this veering (or backing) is evenly distributed throughout the layer. Above this layer, primarily dependent on horizontal advection conditions, winds will show veering or backing with approximately the same average order of magnitude as in the frictional layer.

Table 17-6. Typical frictional veering of wind over plain land with moderately strong gradient winds (18 m/s) and no temperature advection; 51.3°N, 12.5°E, 20 October 1931. [H. Lettau, 1950].

Altitude (100m)	Average Speed (m/s)	Angle* (deg)	Veering (deg/100m)
6.0 to 9.0	18	7	2.3
3.0 to 6.0	16	15	2.6
1.5 to 3.0	13	21	2.6
0.0 to 1.5	9	25	2.3

*Angle between the wind and the gradient wind.

Table 17-7. Average angle formed by the wind and the gradient wind, and average veering for weather stations in Germany, grouped according to topography. [H. Lettau, 1939.]

Altitude (100m)	Coastal Plains	Rolling Country	Hilly Land
	Angle (deg)		
9.0 to 15.0	0	2	3
6.0 to 9.0	2	5	10
3.0 to 6.0	10	17	25
1.5 to 3.0	22	30	36
0.0 to 1.5	29	36	43
	Veering (deg/100m)		
9.0 to 15.0	0.3	0.7	1.0
6.0 to 9.0	0.7	2.0	3.9
3.0 to 6.0	4.3	5.9	5.2
1.5 to 3.0	4.9	4.6	4.3
0.0 to 1.5	4.9	3.0	4.3

17.1.3* Diurnal Variation and Low-Level Jet Streams (below 2000 m)

The mean diurnal variation of wind speed at various heights above any given site is caused by diurnal variations of both the horizontal pressure gradient force and the frictional force. The regular variations of the former are controlled by tidal effects (solar and lunar) which produce pre-

*This is based on the section by H. H. Lettau and D. A. Haugen in the *Handbook of Geophysics for Air Force Designers*, 1957.

Table 17-8. Average veering (deg/100 m) for various ranges of height; means (1918 to 1920) for three stations in U.S.A. in the latitude zone 31° to 36° (average 33°N), and three in latitude zone 40° to 45° (average 43°N). [Condensed from W. R. Gregg, 1922.]

Altitude (100 m)	Southerly Surface Winds				Northerly Surface Winds			
	Summer		Winter		Summer		Winter	
	33°N	43°N	33°N	43°N	33°N	43°N	33°N	43°N
27.0 to 36.0		2.3	3.3	2.3		−3.3	−3.0	−2.3
15.0 to 27.0	1.0	3.3	2.3	3.3	−1.0	−3.3	−1.0	−2.3
6.0 to 15.2	1.0	2.3	2.3	3.0	−1.6	−1.3	−1.0	−2.3
3.6 to 6.0	3.0	2.3	3.3	3.3	−1.0	−1.0	3.0	3.0
1.5 to 3.6	2.3	2.3	3.0	4.3	2.3	2.3	3.0	4.3
0.0 to 1.5	2.3	2.3	3.6	4.3	1.6	2.3	3.6	4.3

dominantly a 12-hourly wave, and by differential solar heating of the air over different locations and subsequent horizontal density gradients. In the troposphere the tidal motions of the atmosphere are small (range less than 0.5 m/s). The barometeric effects of differential solar heating produce marked diurnal wind variations only in special locations (along coast lines and the rims of extended high plateaus). Over most parts of the continents, the diurnal variation of wind speed is controlled by the horizontally uniform effects of the cycle of solar heating and nocturnal cooling of the earth's surface. Consequent changes in the vertical thermal stratification of the atmosphere at 1000 to 2000 m significantly influence the effective frictional force in large-scale air flow.

Over relatively smooth land the daytime thermal stratification intensifies the vertical mixing and the nocturnal thermal stratification weakens it. This causes a wind speed maximum near the ground at about mid-afternoon and a minimum in the early morning hours. As seen in Figure 17-2, the phase of diurnal wind variation is reversed approximately 100 m above the ground, a level that varies with climatic zone, season, and surface roughness from 100 to 200 m. The amplitude of the diurnal variation of wind speed normally has two maxima, at approximately 6 and 600 m. The vertical extent of such diurnal variation varies roughly as the vertical extent of convective activity (2000 m).

Over the midwestern United States the nocturnal maximum of wind speed above approximately 100 m frequently leads to a sharp peak of the velocity profile at heights of 300 to 900 m. The peak, usually at the top of the nocturnal inversion, is significantly stronger (supergeostropic) than explained by a balance between the horizontal pressure gradient and the Coriolis forces; it is often associated with extremely large values of wind shear. These peak winds are called low-level jet streams. The supergeostrophic wind speeds (peak speeds up to 26 m/s in a pressure field resulting in 10 to 15 m/s of geostrophic speed) suggest that an inertial oscillation of the air masses is induced when the constraint imposed by the daytime mixing is released by the initiation of stable thermal stratification near sunset. Average wind profiles showing the development of a low-level nocturnal jet stream over O'Neill, Nebraska, are given in Table 17-9. A particularly large value of wind speed variation with height, recorded during the development of a low-level jet stream, was obtained by kite observation at Drexel, Nebraska on the night of 18 March 1918; the surface wind speed was 26 m/s, but at an elevation of 238 m the reported wind speed was 36 m/s, yielding an average shear of 0.14 s^{-1}.

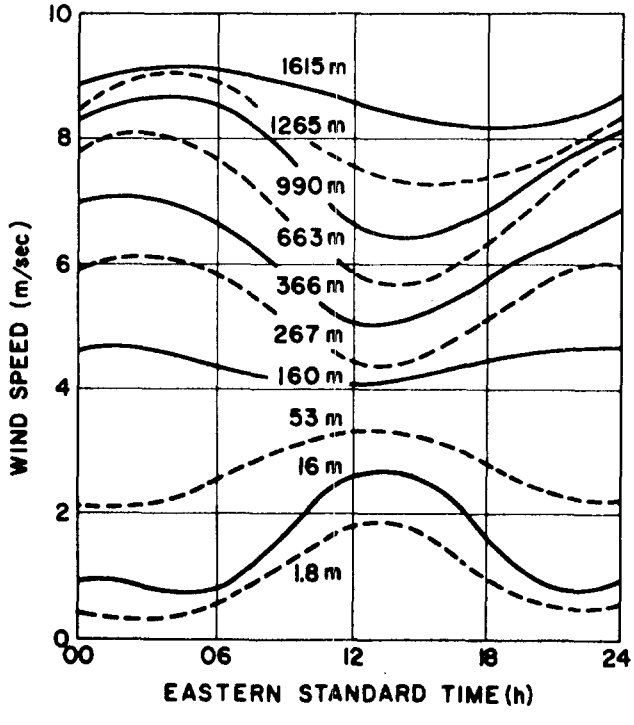

Figure 17-2. Diurnal curves (slightly smoothed) of annual mean wind speed at Oak Ridge, Tennessee, average for 1948 to 1952. (The wind speed data at heights of 1.8 and 16 m are from anemometer recordings; for other heights, data were obtained from pilot-balloon soundings at 4-h intervals [dashes are for clarity of illustration].)

Table 17-9. Average wind profiles (speed and direction at various heights) showing development of nocturnal low-level jet stream (Average of five nights of observations, Great Plains Turbulence Field Program, O'Neill, Nebraska.)

Height (km)	Mean Local Time							
	1800		2000		2200		2400	
	Speed (m/s)	Dir. (deg.)	Speed (m/s)	Dir. (deg.)	Speed (m/s)	Dir. (deg.)	Speed (m/s)	Dir. (deg.)
2.0	6.1	223	4.3	225	3.5	223	3.1	231
1.8	7.2	219	5.0	226	4.0	227	3.4	233
1.5	9.4	213	8.3	225	5.6	229	5.0	232
1.2	10.9	207	12.3	217	10.8	225	8.9	223
0.9	11.6	194	14.7	202	13.9	211	13.1	219
0.8	11.7	190	15.5	193	15.9	204	16.2	213
0.6	11.6	182	15.8	190	17.2	196	19.6	203
0.3	10.8	177	14.7	178	18.0	183	18.9	189
0.2	9.7	174	13.6	171	14.9	175	15.1	183
0.1	9.2	173	12.2	167	12.8	170	12.9	170
	0200		0400		0600		0800	
	Speed (m/s)	Dir. (deg.)	Speed (m/s)	Dir. (deg.)	Speed (m/s)	Dir. (deg.)	Speed (m/s)	Dir. (deg.)
2.0	4.0	227	3.7	214	3.3	208	4.5	208
1.8	4.2	226	3.9	220	3.7	212	4.9	208
1.5	5.4	226	4.5	227	4.8	213	6.2	204
1.2	8.5	227	8.0	228	6.7	218	8.3	203
0.9	13.5	224	12.1	228	10.5	220	11.2	213
0.8	16.5	219	14.5	225	12.7	220	12.4	215
0.6	18.9	211	17.5	217	15.6	217	13.9	215
0.5	19.9	203	18.9	209	17.2	213	15.9	213
0.3	19.0	196	18.7	199	17.3	204	14.0	204
0.2	17.1	189	16.2	191	14.5	195	12.6	195
0.1	13.4	187	13.9	189	12.7	191	11.8	191

Over the ocean, the diurnal variation of wind speed is negligible because diurnal variations in thermal stratifications are extremely small. In coastal regions where land and sea breezes are experienced, the amplitude and phase of the diurnal variation of wind speed are comparable with those over land. A reversal of phase with height is questionable, however. The vertical extent of the sea breeze is roughly 1000 m, the land breeze roughly 500 m, the overall land-sea breeze system including return flow, about 3000 m.

In mountainous regions, the daytime, up-slope valley winds (1 to 3 m/s) are normally stronger than the night-time down-slope mountain winds (0.2 to 2 m/s). The mean amplitude of the variation decreases very slightly with height. A reversal of phase with height is occasionally found. The vertical extent of the valley breeze is about that of the height of the surrounding ridges, the mountain breeze, 60 to 100 m. The whole system extends about 300 m above the height of the ridges.

The various features of local wind variation discussed here occur quite frequently. In general, they are easily observed during conditions of clear skies and light to moderate intensity of the large-scale airflow. It should be remembered, however, that when the diurnal variations are not readily observed, it may be because they are superimposed on the large-scale airflow. Empirical wind structure models not accounting for possible diurnal variations could then be in error.

17.2 LARGE SCALE WIND STRUCTURE

This section provides information on the vertical and horizontal distribution of winds for altitudes up to 90 km. The wind data for altitudes up to about 26 km are based on routine rawinsonde observations taken by the National Weather Service (NWS). The root mean square (rms) observational errors in vector wind measurements using FPS-16, T-19, or similar tracking radar for altitudes up to 26

km are 1 m/s plus 2% the vector wind speed. The information presented on winds between 26 and 60 km was obtained from Meteorological Rocket Network (MRN) observations. Most of the available observations are for locations in the Northern Hemisphere. The estimated rms observational errors at these altitudes are 2 m/s plus 3% of the vector wind. The wind distribution at altitudes between 60 and 90 km are based on data obtained from grenade and inflatable falling sphere experiments. The estimated rms error for the falling sphere observations, which make up the largest portion of the data, is 2 to 3 m/s between 60 and 90 km.

17.2.1 Seasonal and Day-to-Day Variations

The broad features of the seasonal change in winds between the surface and 90 km are reasonably well established. Figure 17-3 is a meridional cross section of the observed mean monthly zonal wind components for January and July from the surface to 80 km. The seasonal change in the stratospheric and mesospheric wind fields differs from tropospheric seasons in timing and length of season. At middle and high latitudes, long periods of easterly and westerly flow are separated by shorter periods of transition as shown by the curves of the mean monthly 50-km zonal wind components in Figure 17-4 for White Sands, 32°N, Wallops Island, 38°N, and Ft. Churchill, 59°N. The mean monthly

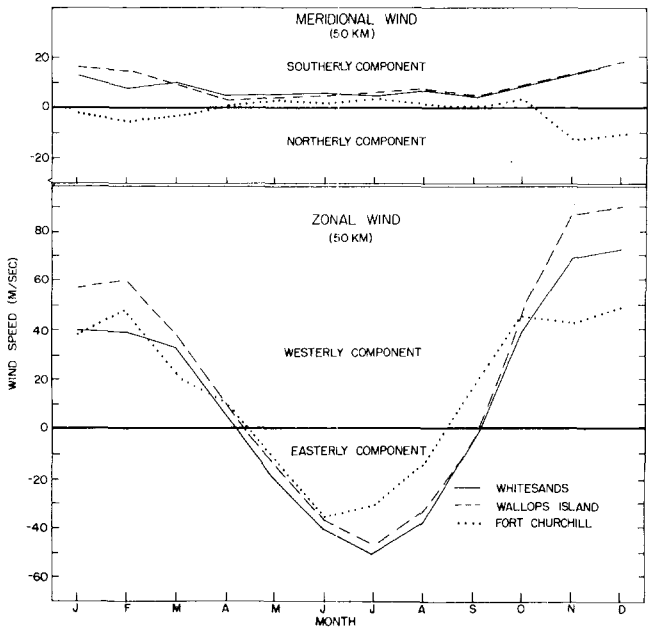

Figure 17-4. Annual variation of meridional and zonal wind at White Sands, Wallops Island and Ft. Churchill.

meridional components (Figure 17-4) are less variable and maintain a slight southerly (positive) component at most locations throughout the year.

Profiles of mean monthly zonal wind speeds (m/s) for each of the midseason months at Ascension Island, Wallops

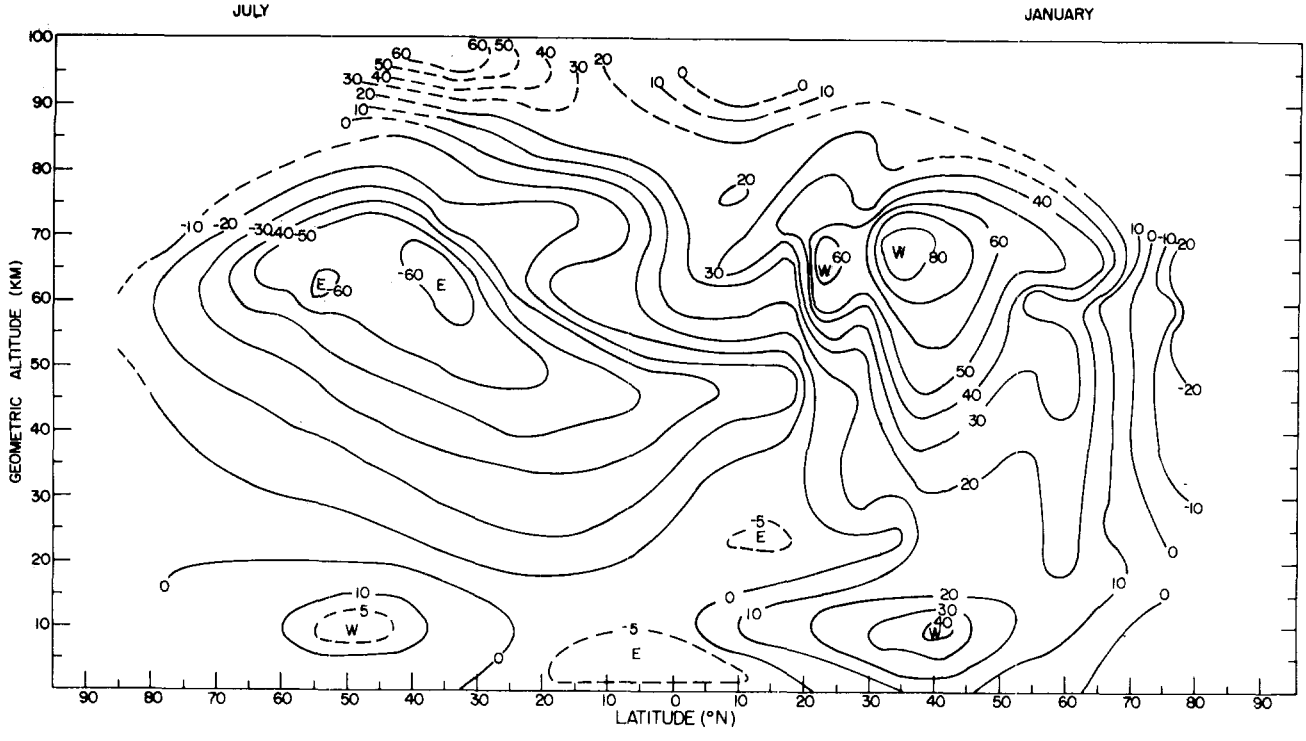

Figure 17-3. Meridional cross section of zonal wind speed (m/s).

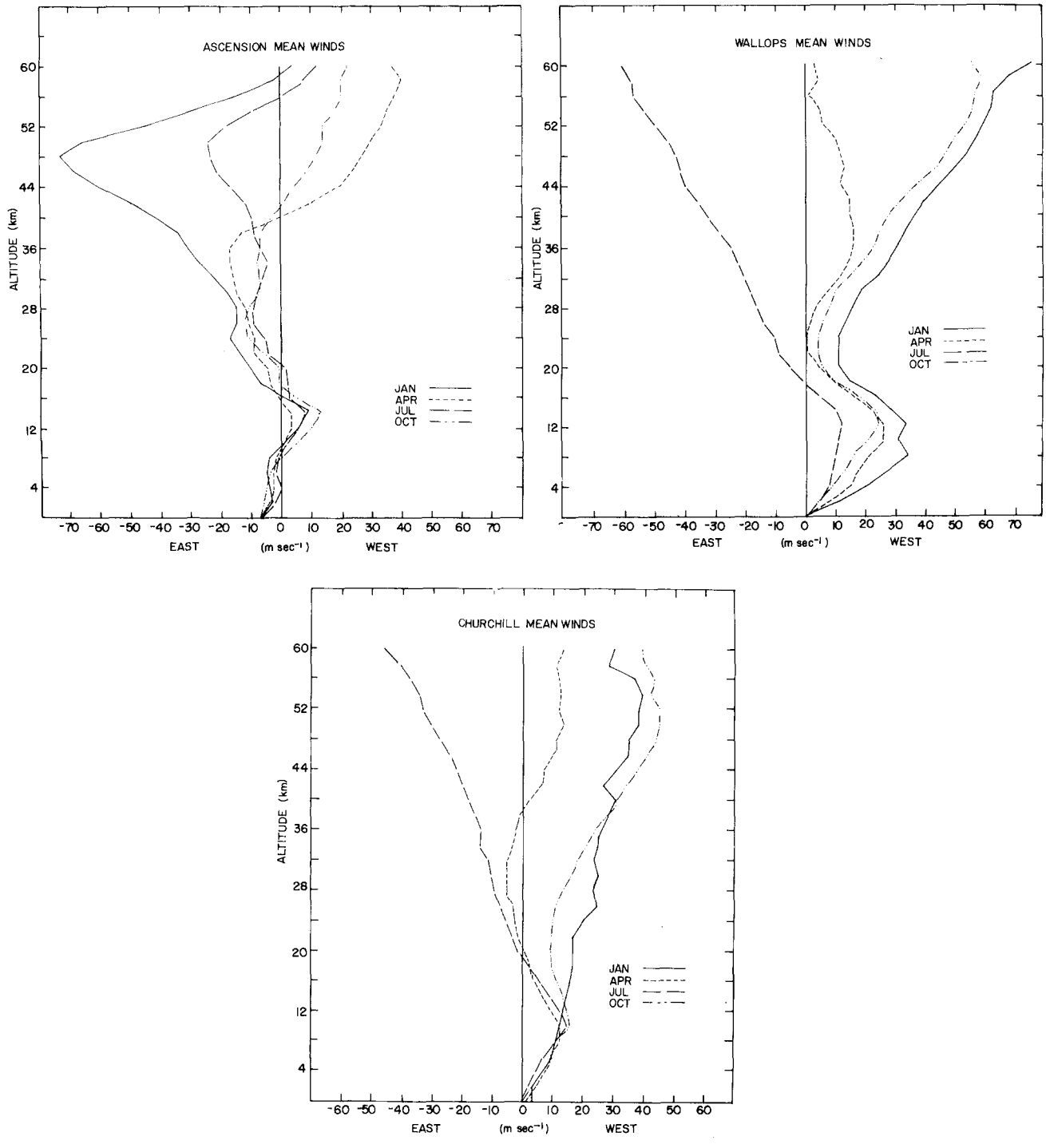

Figure 17-5a. Seasonal effects on the zonal wind profiles at Ascension Island, Wallops Island and Ft. Churchill.

Island and Fort Churchill, from a report by Kantor and Cole [1980] are plotted in Figure 17-5 for altitudes up to 60 km. The seasonal variations in the mean monthly zonal winds are largest at Wallops Island, a midlatitude location, and at altitudes above 30 km. The largest day-to-day variations around the mean monthly values (Figure 17-6) occur during the winter months at altitudes above 20 km at middle and high latitudes.

17.2.2 Time and Space Variations

The change and movement of pressure patterns in the atmosphere cause standard wind observations (for example, the mean wind over 1 min) to vary from time to time at a given place, and from place to place at a given time. In general, as shown in Figure 17-7, the amount of change in wind between two observations increases with the time in-

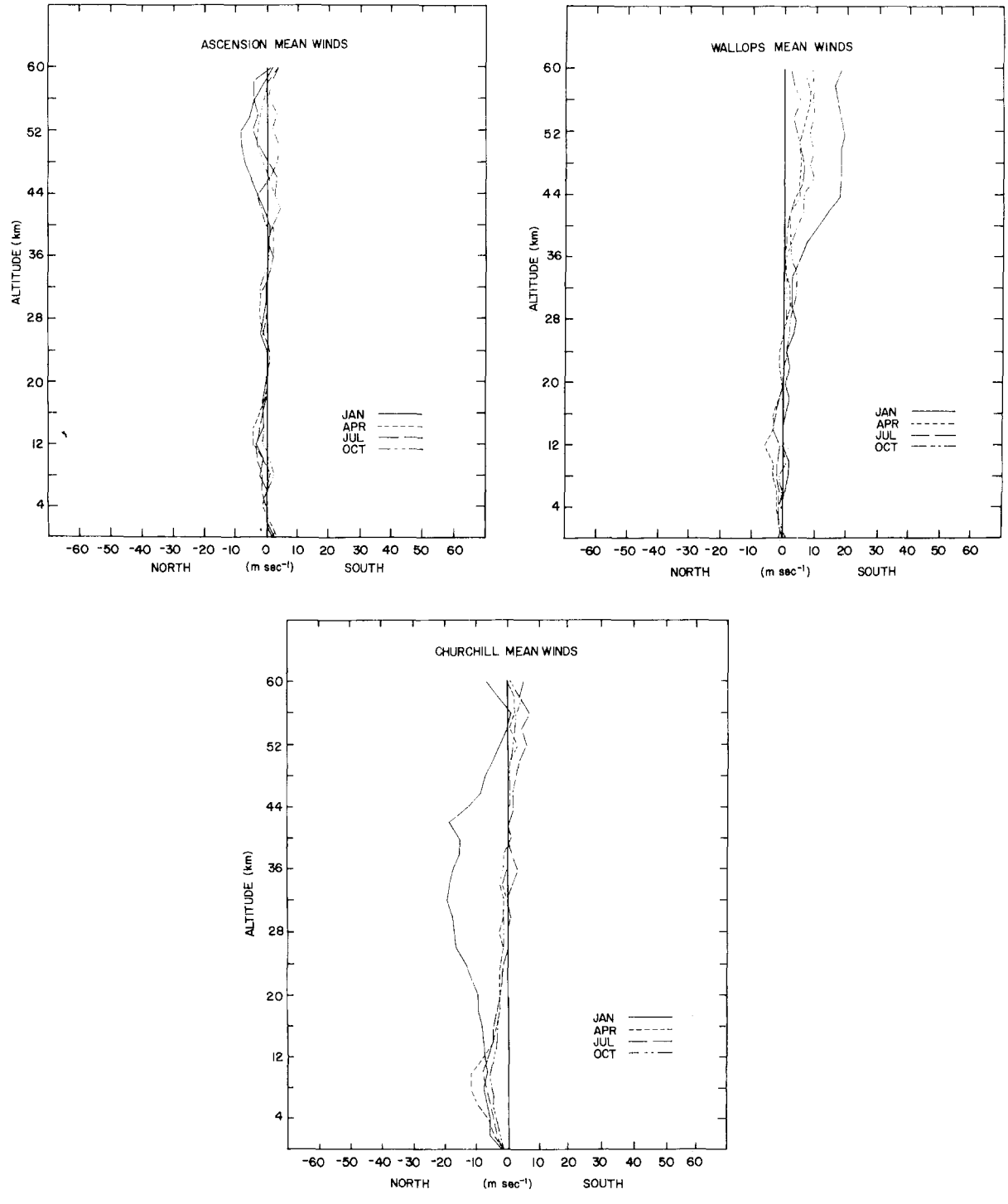

Figure 17-5b. Seasonal effects on the meridional wind profiles at Ascension Island, Wallops Island and Ft. Churchill.

terval between them and with the distance between observing points. The rate of increase in wind change with increasing time or space interval between observations is, in turn, a variable depending upon season, geographic location, average wind speed, nature of the sample, and, to some extent, height above the ground.

Most of the wind variability data pertaining to the free atmosphere below 30 km are derived from standard pilot balloon or rawinsonde observations. Lower limits of resolution of these observations are such that minimum intervals for wind variability are about 15 min or 1.6 km. The small-scale fluctuations appear to be fairly random, and their combined effect on ballistic or synoptic-scale forecasting problems normally cancel out and, thus, are neglected.

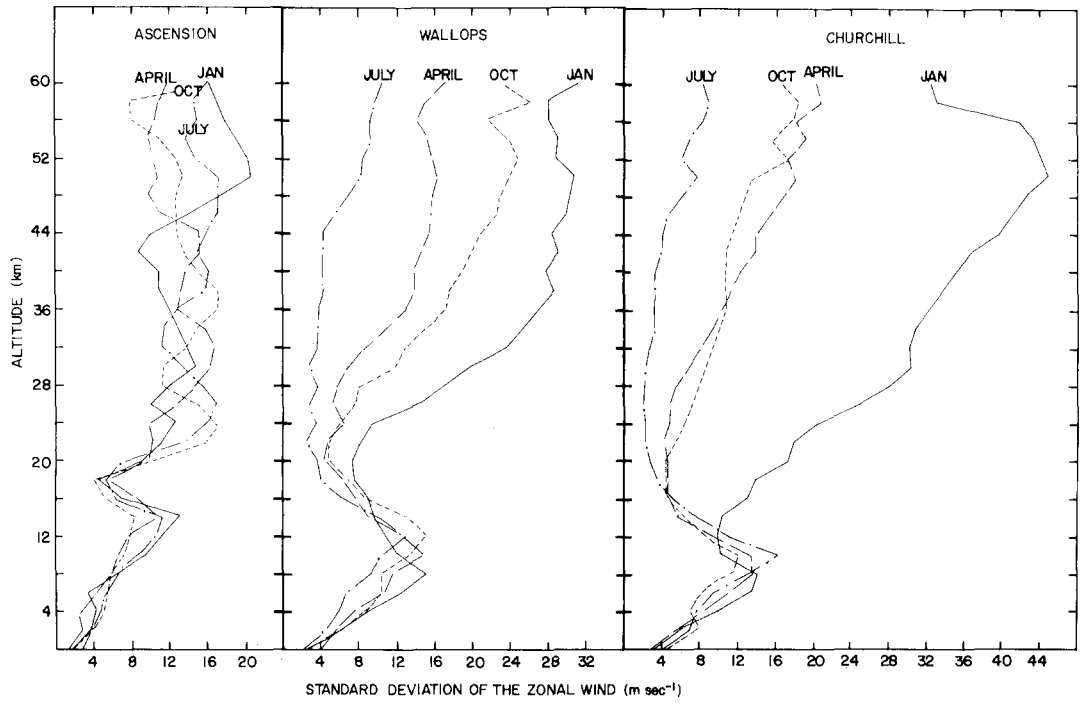

Figure 17-6a. Day-to-Day variability around mean monthly zonal winds for the midseason months at Ascension Island, Wallops Island, and Ft. Churchill.

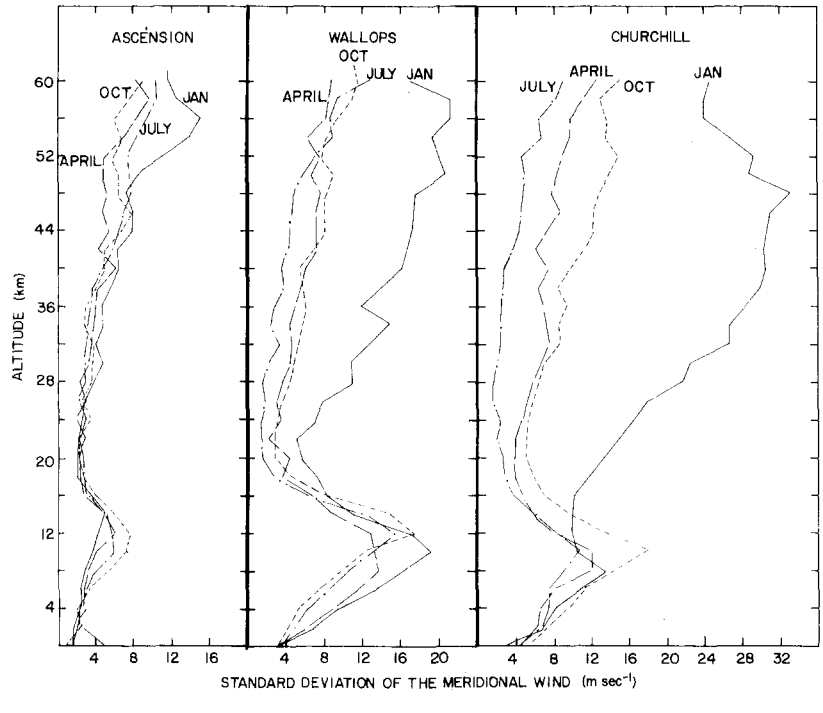

Figure 17-6b. Day-to-Day variability around mean monthly meridional winds for the midseason months at Ascension Island, Wallops Island and Ft. Churchill.

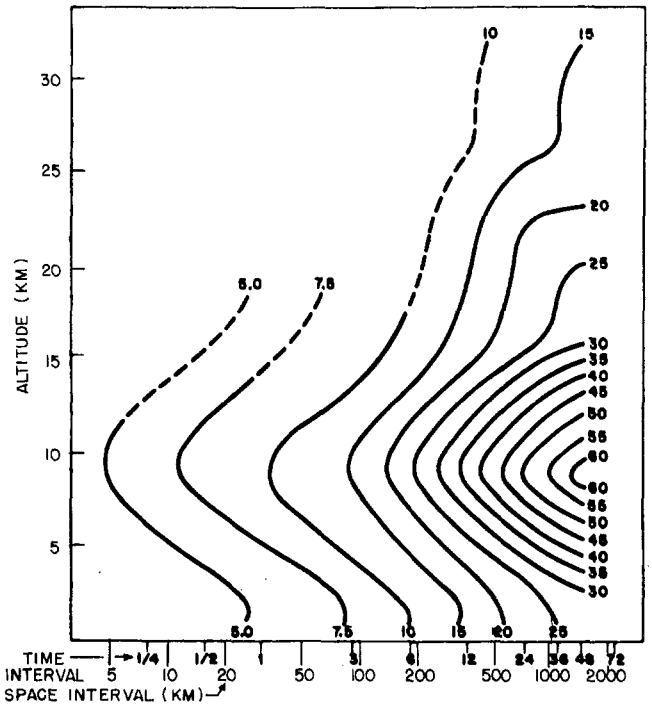

Figure 17-7. Isopleths of time and space variabilities of changes in the mean vector wind with altitude; the rms (63rd percentile) values, in kilometers, of observed changes for various time lags between observations, and of derived changes for various distances are given on each curve [Ellsaesser, 1960].

Observations of VHF and UHF radar backscatter from turbulence in the clear atmosphere, conducted at several locations during the past several years, permit much more detailed measurement of the time variation of vector winds than was previously attainable. Depending on the radar wavelength and the power-aperture product [Gage and Balsley, 1978], measurements are obtainable from near the surface to an altitude of about 100 km. Several radars which were originally designed for ionospheric research have been used for observations of the neutral (non-ionized) atmosphere, and a few radars have been built specifically for tropospheric and stratospheric wind measurements. The latter include NOAA radars in Colorado and Alaska and the SOUSY-VHF-Radar operated by the Max-Planck-Institut fur Aeronomie in the Federal Republic of Germany. Examples of data are presented by Green et al. [1979], Balsley and Gage [1980], Rottger [1979], and in numerous other publications. A radar of this type has been incorporated into the NOAA Prototype Regional Observation and Forecasting System (PROFS).

Several measures of wind variability are possible. The most useful measure is the (RMS) of the vector change in wind; others commonly used are the mean and the median absolute vector differences. All of these are scalar measures computed from the magnitudes of the difference vectors. They are related in a circular normal distribution which is usually a good approximation to the frequency distribution of wind changes.

17.2.2.1 Time Variability up to 30 km. The time rate of change of wind in the frictional layer is affected by the topography and the thermal structure. The results in Table 17-10 are for steady southerly flow conditions from seven observational periods, all but one of which extended over 24 h (pilot balloon, rawinsonde, and smoke-puff observations are combined). The effect of thermal stratification is indicated by comparision of the day and night values for time differences up to 8 h.

The change in wind variability above the frictional layer with increasing time between observations and with altitude is illustrated in Figure 17-7. Figure 17-8 shows the effect of latitude and season for a 24-h lag between wind observations.

For relatively short periods during which the pattern of the winds is fairly stable, the variability of the wind is given directly by

$$S_t = Kt^P, \qquad (17.3)$$

where S_t is the rms change in wind during the time interval t, and K is a constant. The exponent p depends on r_t, the correlation coefficient between winds separated by the time interval t. At short lags where r_t is 1, p is 1; at greater lags where r_t is 0, p is 0.5. For t in hours and S_t in m/s

$$S_t = 1.8\ t^{0.5} \qquad (17.4)$$

is a suitable generalization for middle latitudes and for lag intervals of 30 min to about 12 h. Although this empirical relation is an acceptable average, K actually depends on the mean wind speed. The mean wind varies with season, altitude, and geographic location (see Figure 17-5); hence, values of K other than 1.8 will on some occasions be more applicable to engineering problems. Values of K from 1.5 to 6.3 are tabulated by Arnold and Bellucci [1957]. An analysis of the relationship of K to the mean wind in a stable flow pattern shows that K increases from about 0.5 at speeds of 2 m/s to perhaps 2 or 3 at speeds of 16 m/s and higher.

An indirect model relates the variability in time to r' and to the climatological dispersion of the winds. This relationship is given by

$$S_t = \sigma_t\sqrt{2(1 - r_t)}, \qquad (17.5)$$

where σ_t is the standard vector deviation of the winds (rms deviation from the vector resultant wind). The vector stretch correlation coefficient between the initial wind having components u and v and the wind after a time interval t, having components x and y, is given by

Table 17-10. Mean and standard deviation of absolute value of vector velocity differences at various time intervals, Δ t, in the lower 1829 m over smooth open terrain (Great Plains Turbulence Field Program).

Height (1000 m)	Velocity Differences (m/s)					
	Δt = 2 hours		Δt = 4 hours		Δt = 8 hours	
	Day	Night	Day	Night	Day	Night
1.8	3.0 ± 1.7	3.3 ± 2.4	5.0 ± 2.6	4.5 ± 3.2	7.4 ± 2.4	4.0 ± 2.9
1.4	2.6 ± 1.5	2.8 ± 1.9	4.2 ± 2.5	4.2 ± 2.6	5.4 ± 2.8	5.1 ± 3.3
0.9	2.6 ± 1.7	3.9 ± 2.5	4.1 ± 2.2	5.6 ± 2.6	5.4 ± 1.9	7.5 ± 3.1
0.5	3.1 ± 2.2	4.0 ± 2.8	4.8 ± 3.1	6.5 ± 3.5	6.8 ± 2.8	9.6 ± 3.1
0.4	3.0 ± 1.9	4.0 ± 3.0	4.8 ± 3.1	6.9 ± 4.5	7.1 ± 3.5	6.2 ± 3.5
0.2	2.6 ± 2.4	3.4 ± 3.1	4.3 ± 2.9	6.0 ± 5.4	6.2 ± 3.1	8.9 ± 4.9
	Δt = 12 hours		Δt = 16 hours	Δt = 20 hours	Δt = 24 hours	
1.8	5.6 ± 2.9		6.4 ± 3.1	7.5 ± 3.5	6.5 ± 3.3	
1.4	6.3 ± 3.1		6.6 ± 3.0	5.9 ± 2.1	4.8 ± 2.6	
0.9	7.8 ± 3.0		7.7 ± 3.5	5.9 ± 2.8	4.4 ± 2.6	
0.5	10.2 ± 3.9		8.8 ± 4.1	6.9 ± 4.0	4.9 ± 3.3	
0.4	10.4 ± 4.1		8.8 ± 3.6	7.1 ± 4.9	4.6 ± 2.9	
0.2	8.3 ± 3.7		7.2 ± 3.8	6.0 ± 4.9	4.3 ± 3.9	

$$r_t = \frac{\sum(ux + vy)}{\sqrt{\sum(u^2 + v^2)\sum(x^2 + y^2)}}. \qquad (17.6)$$

This parameter undergoes an exponential decay with increasing lag for intervals up to 24 h or more, and then appears to oscillate about zero. The relation,

$$r_t = \exp(-0.0248t), \qquad (17.7)$$

with t in h, is widely used. This equation, in conjunction with Equation (17.5) and values of σ_t allows an estimate of the wind variability for a desired lag interval that pertains specifically to the place, season, and altitude of interest. This model has two serious limitations; it will not permit r_t to become negative, nor does the constant coefficient of t allow for variations in the rate of decay of the correlation. At sufficiently large time intervals, r_t does become negative, and r_t is so close to zero for lags in excess of 72 hours that the model becomes unreliable. In some cases r_t becomes negative at shorter lags, and the lag at which this occurs varies from place to place. Investigations of the rate of decay of correlation show that it varies geographically, seasonally, and probably with altitude. The variation has been mapped only for the United States at 5.5 km [Ellsaesser, 1960].

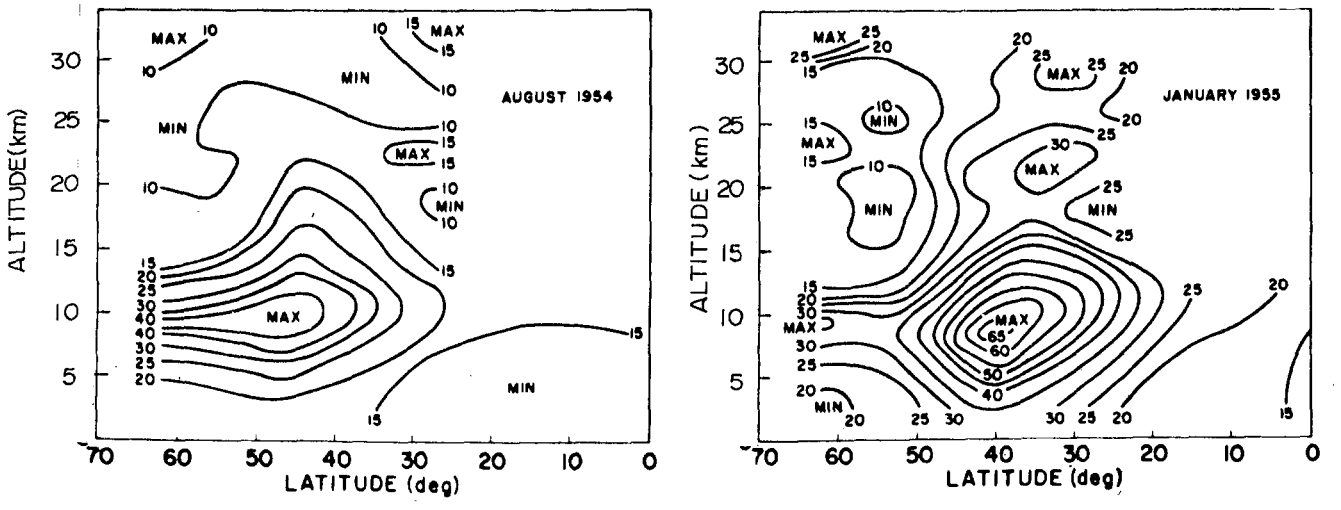

Figure 17-8. Distribution in latitude and altitude of the vector wind variability (St) for a 24-h time lag between observations along the meridian 75°W in summer and winter (August 1954 data are for East Africa): rms values in knots are shown on curves [Ellsaesser, 1960].

Attempts to develop a more precise model of the variability of winds with time have resulted either in only moderate improvement or extremely complex models. Thus Equation (17.7) is considered the most useful approximation. When precision in estimating the wind variability with time is required, a special climatological study must be made.

17.2.2.2 Spatial Variability up to 30 Km. In general, varability increases with increasing distance between observation points, and the rate of increase with distance depends on geographic location, season, and altitude. A change in the wind with time can be thought of as resulting in part from the movement of wind-field patterns over the observing point, and thus as analogous to the spatial variability.

Extending this analogy to the models, the space variability of wind S_d is given by $K'd^P$, where d is the distance between observing points. The parameter K′ varies with season, geographic location, and altitude, but no detailed examination has been made of the way in which these factors act. Arnold and Bellucci [1957] tabulated values of K′ from 1.1 to 6.1. They consider the expression, representative for middle latitudes.

$$S_d = 1.5d^{0.5}, \qquad (17.8a)$$

where S_d is in mph and d in miles, or converted to metric units

$$S_d = 0.53d^{0.5} \qquad (17.8b)$$

where S_d is in m/s and d in km.

The indirect model provides several empirical curves for the decay of the correlation coefficient of winds with increasing separation between observing points. These curves indicate differing rates of decay depending upon latitude and upon the orientation of the line connecting the observing points. The analogy between time and space variability of the winds extends to these curves. Figure 17-7 indicates that, for temperate latitudes, a general approximation to the space variability of winds can be obtained by taking 3 hours as equivalent to 92.6 km. The space variability is then estimated in a manner similar to time variability from $\sigma_d \sqrt{2(1 - r_d)}$; where r_d is the correlation coefficient between winds separated by the distance interval d.

17.2.2.3 Time and Space Variations—30 to 60 km. Observations show that pronounced diurnal and semi-diurnal oscillations exist in the winds at altitudes above 30 km. Sufficient data, however, are not available to permit the development of a satisfactory model for all latitudes and seasons. The results of an analysis of a series of wind observations taken at Wallops Island during a 48-h period in May 1977, shown in Figure 17-9, provide an indication of the magnitude of the diurnal oscillation at a midlatitude location. The X's in Figure 17-9 are average values of the north-south and east-west wind components at the indicated local times. The curves are based on a harmonic analysis of the meridional (N-S) and zonal (E-W) wind components. The amplitude of the combined diurnal and semidiurnal oscillations of the N-S component, increases with altitude above 30 km, reaching a maximum of 10 to 11 m/s between 50 and 55 km. The diurnal variations of the E-W component

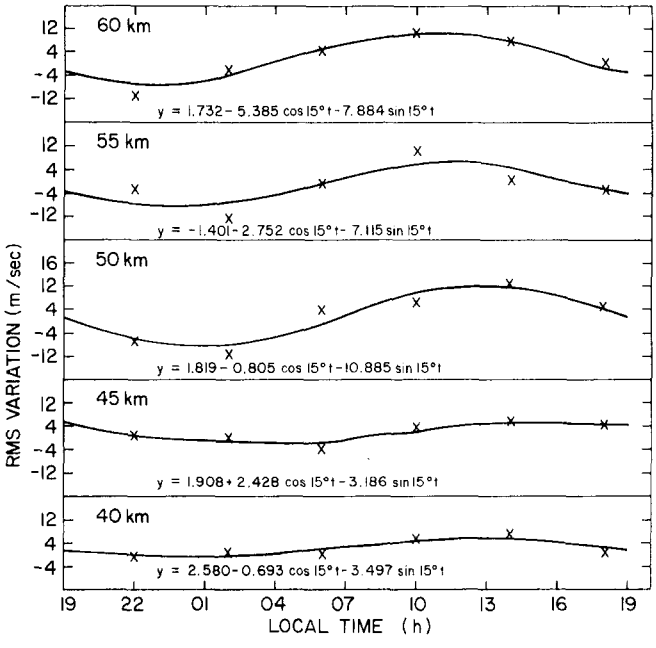

Figure 17-9a. Diurnal wind variations at Wallops Island in May (N-S).

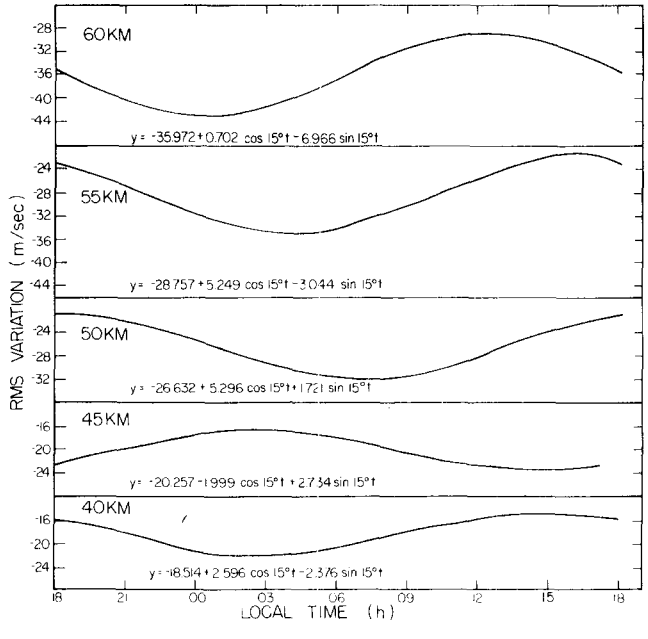

Figure 17-9b. Diurnal wind variations at Wallops Island in May (E-W).

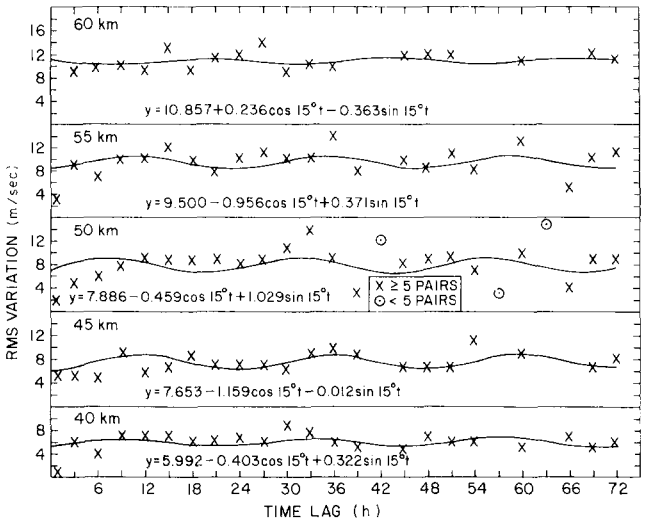

Figure 17-10. Rms differences between north-south winds observed 1 to 72 h apart in Ascension, Ft. Sherman and Kwajalein.

are not as well defined at 40 and 45 km. At altitudes of 50 km and above, however, the amplitudes are between 12 and 14 m/s. The magnitude of the diurnal oscillations are somewhat smaller in tropical and arctic regions.

Rms differences between wind components observed from 1 to 72 h apart have been analyzed at altitudes between 30 and 60 km to obtain estimates of the variations in these components with time. Rms differences between the N-S wind components observed from 1 to 72 h apart at Ascension, Ft. Sherman and Kwajalein are shown in Figure 17-10. Data for all seasons for these three stations have been combined. The values display a relatively stable rms variation of roughly 10 to 12 m/s for periods up to 72 h at 55 and 60 km and about 6 or 7 m/s at altitudes of 40 and 45 km. There is an indication of a diurnal cycle with an amplitude of 1 to 2 m/s at these altitudes as shown by the 24-h harmonic curves which have been fitted to the individual values. Most of the observed variability can be attributed to random measurement errors as there is little difference in the rms variations between observations taken 6 h apart and those taken 72 h apart.

In summer conditions are approximately the same at all latitudes, with little change in rms values with time. In winter, however, the rate at which the rms values increase with time varies with latitude. The larger day-to-day changes in the synoptic patterns at middle and high latitudes are reflected in well-defined increases in the rms variability with time. At 50 km, for example, rms values for the N-S components at White Sands Missile Range (32°N) increase with time from 6 to 8 m/s to 16 or 18 m/s in 72 h. At Poker Flats (64°N) and Ft. Churchill (59°N), they increase from 6 or 8 m/s to 25 m/s. The diurnal cycle in observed data is masked by the synoptic changes and instrumentation errors during the winter months at middle and high latitudes.

17.3 WIND PROFILES

17.3.1 Wind Shear

Wind shear is the derivative of the wind vector with respect to distance and is itself a vector. The shear of the horizontal wind is of primary interest and is the one discussed in this section. The terms vertical wind shear and horizontal wind shear are commonly used in referring to the shear of the horizontal wind in the vertical and horizontal directions, respectively. Horizontal wind shear is the derivative of the horizontal wind with respect to an axis parallel to the earth's surface. Its applications are restricted largely to meteorological analysis. Vertical wind shear is expressed as $\Delta W/\Delta y$, where Δ is the change of the horizontal wind in the altitude interval Δy; the unit of shear is s^{-1}. Although direction is also necessary to specify the shear vector, it is usually ignored; for design purposes shear is normally applied in the most adverse possible direction.

The climatology of vertical wind shear is applicable to problems dealing with design and launch of vertically rising vehicles and jet aircraft, radioactive fallout investigations, and many phases of high-altitude research. Most investigations of shear climatology are for specific locations in order to satisfy design and operational requirements of missiles and other vehicles at or near launch sites. For vehicles with other than a vertical flight path, vertical wind shear can be determined by multiplying the shear by the cosine of the angle between the vertical axis and the vehicle trajectory.

Measurements of vertical wind shear indicate that average shear behaves inversely with layer thickness (scale-of-distance). This is illustrated in Figure 17-11, which is based on a relatively large number of observations during

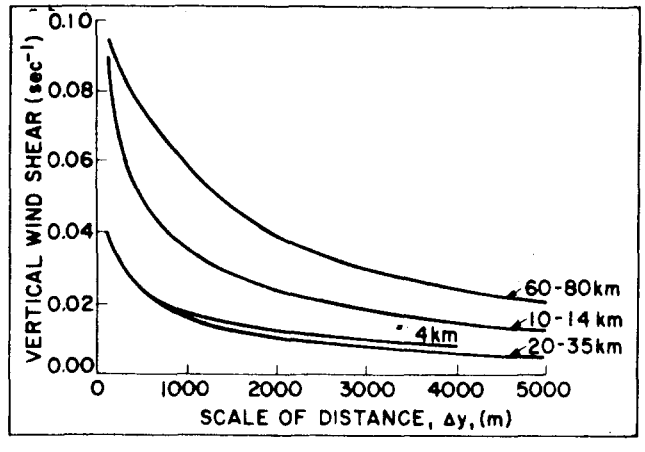

Figure 17-11. Selected vertical wind shear spectrums (4, 10–14, 20–35, and 60–80 km altitude) for use with 5% and 1% probability level wind profile envelope, Cape Canaveral, Florida [Scoggins and Vaughan, 1962].

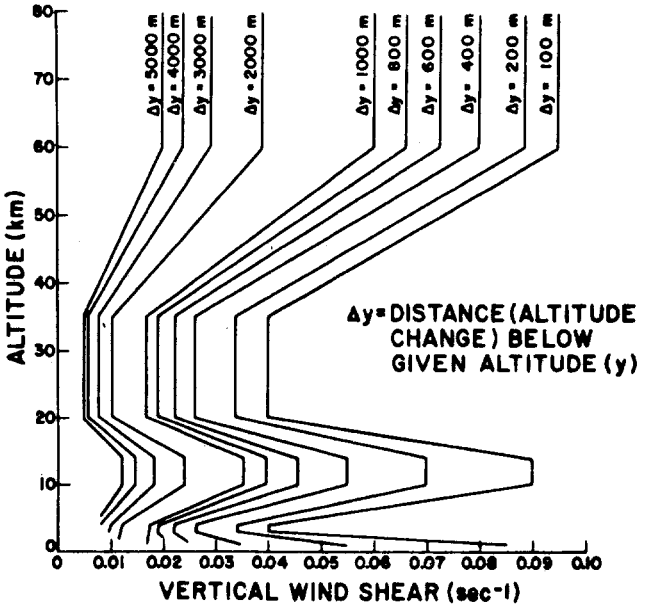

Figure 17-12. 1% probability-of-occurrence vertical wind shear spectrum as function of altitude and scale-of-distance for association with the 5% and 1% wind speed profile envelope for Cape Canaveral, Florida [Scoggins and Vaughan, 1962].

the windiest months over Cape Canaveral, Florida. Figure 17-12, based on the same data, shows the variation of shear with altitude and with layer thickness; it provides, as an example, the vertical wind shear spectrum at Cape Canaveral with a 1% probability of occurrence.

Wind shears for scales-of-distance $\Delta y \geq 1000$ m in thickness are computed directly from rawinsonde and rocketsonde observations, whereas smaller scale shears can be calculated directly only from special fine-scale observations. However, shears associated with scales-of-distance $\Delta y < 1000$ m can be estimated from the following relationship [Fichtl, 1972]:

$$\Delta u = \Delta u_{1000} \left(\frac{1000}{\Delta y} \right)^{0.3}, \qquad (17.9)$$

where Δu is the shear, Δu_{1000} is the 1000 m shear, and Δy is the scale-of-distance in m for thickness < 1000 m.

Wind shear statistics for various locations differ primarily because of prevailing meteorological conditions, orographic features, and data sample size. As a result, significant differences exist in the shear structure for different locations. Consistent shear data for five vehicle launch and/or landing sites are presented in Tables 17-11 through 17-15 for the Eastern Test Range, Florida; Vandenberg AFB, California; Wallops Island, Virginia; White Sands Missile Range, New Mexico; and Edwards AFB, California. To get actual shear (s^{-1}) from the indicated wind speed changes, divide by the appropriate scale-of-distance. Table 17-16 gives envelopes of the 99% wind speed change for the five locations combined. The data contained in Table 17-16 are applicable when design or operational capability is not restricted to a specified launch site or may involve several geographical locations. Equation (17.9) was used to construct Tables 17-11 through 17-16 for scales-of-distance < 1000 m.

17.3.2 Interlevel Correlations

Deviations in the assumed vertical wind profile over a target or reentry point affect the range and cross-range of a ballistic missile. These effects must be considered in the design of guidance systems for entry vehicles and for targeting ballistic missiles.

The mean effect E of mean monthly or mean seasonal winds on the range and cross range of a missile can be determined for a particular location by computer-simulated flights through mean monthly component wind profiles if

Table 17-11. Envelopes of 99% wind speed change (m/s), 1–80 km altitude region, Eastern Test Range [Kaufman, 1977].

Wind Speed at Reference Altitude (m/s)	Scales of Distance (m) Thickness									
	5000	4000	3000	2000	1000	800	600	400	200	100
≥ 90	77.5	74.4	68.0	59.3	42.6	36.4	29.7	22.4	13.8	8.5
= 80	71.0	68.0	63.8	56.0	40.5	34.7	28.5	21.4	13.2	8.1
= 70	63.5	61.0	57.9	52.0	38.8	33.1	27.0	20.3	12.5	7.7
= 60	56.0	54.7	52.3	47.4	36.0	31.0	25.3	18.9	11.7	7.2
= 50	47.5	47.0	46.2	43.8	33.0	28.3	23.2	17.5	10.7	6.6
= 40	39.0	38.0	37.0	35.3	29.5	25.3	20.6	15.5	9.6	5.9
= 30	30.0	30.0	29.4	26.9	22.6	19.4	15.8	11.9	7.3	4.5
= 20	18.0	17.5	16.7	15.8	14.6	12.5	10.2	7.5	4.7	2.9

Table 17-12. Envelopes of 99% wind speed change (m/s), 1–80 km altitude region, Vandenberg AFB [Kaufman, 1977].

Wind Speed at Reference Altitude (m/s)	Scales of Distance (m) Thickness									
	5000	4000	3000	2000	1000	800	600	400	200	100
≥ 90	66.9	62.5	57.8	51.5	37.5	32.1	26.1	19.7	12.0	7.4
= 80	64.1	60.8	56.6	48.8	36.9	31.5	25.6	19.1	11.6	6.8
= 70	62.0	59.2	54.8	48.1	36.0	31.0	25.0	18.6	11.2	6.5
= 60	57.1	54.5	51.3	45.4	32.7	28.5	23.0	17.1	10.2	5.3
= 50	49.6	47.8	45.7	42.1	30.1	25.9	21.8	15.6	9.2	5.0
= 40	39.4	38.8	37.9	35.5	25.9	23.5	19.6	14.9	8.8	4.8
= 30	30.0	29.4	28.3	26.3	20.5	18.6	15.8	12.2	8.0	4.6
= 20	20.0	19.8	19.5	18.4	15.0	13.1	10.9	9.0	6.3	4.3

Table 17-13. Envelopes of 99% wind speed change (m/s), 1–80 km altitude region, Wallops Island [Kaufman, 1977].

Wind Speed at Reference Altitude (m/s)	Scales of Distance (m) Thickness									
	5000	4000	3000	2000	1000	800	600	400	200	100
≥ 90	72.5	67.0	60.2	50.5	37.6	32.3	26.3	19.8	12.2	7.5
= 80	66.5	62.5	57.5	48.8	37.0	31.7	25.9	19.5	12.0	7.4
= 70	61.2	58.5	53.8	46.5	35.8	30.7	25.1	18.9	11.6	7.1
= 60	54.4	52.5	50.0	44.4	34.5	29.6	24.2	18.2	11.2	6.9
= 50	46.2	44.2	42.3	38.8	33.0	28.3	23.2	17.4	10.7	6.6
= 40	36.7	35.6	34.5	32.3	27.6	23.7	19.3	14.5	8.9	5.5
= 30	27.2	26.3	25.3	24.2	20.6	17.7	14.7	10.8	6.7	4.1
= 20	17.8	17.3	16.8	16.4	15.2	13.0	10.6	8.0	4.9	3.0

Table 17-14. Envelopes of 99% wind speed change (m/s), 1–80 km altitude region, White Sands Missile Range [Kaufman, 1977].

Wind Speed at Reference Altitude (m/s)	Scales of Distance (m) Thickness									
	5000	4000	3000	2000	1000	800	600	400	200	100
≥ 90	70.7	67.0	61.2	52.4	42.0	36.0	29.4	22.1	13.6	8.4
= 80	66.0	63.0	57.7	50.0	40.2	34.5	28.1	21.2	13.0	8.0
= 70	60.2	57.0	53.0	46.5	38.0	32.6	26.6	20.0	12.3	7.6
= 60	52.6	50.0	46.5	42.3	35.5	30.5	24.9	18.7	11.5	7.1
= 50	45.0	43.0	40.2	37.0	32.0	28.3	23.1	17.4	10.7	6.6
= 40	36.5	35.5	34.8	33.5	29.3	25.1	20.5	14.5	9.5	5.5
= 30	27.4	27.0	26.4	24.8	22.0	19.3	15.8	11.8	7.3	4.5
= 20	18.4	17.7	17.3	16.5	15.0	12.9	10.5	7.9	4.9	3.0

Table 17-15. Envelopes of 99% wind speed change (m/s), 1–80 km altitude region, Edwards AFB [Kaufman, 1977].

Wind Speed at Reference Altitude (m/s)	Scales of Distance (m) Thickness									
	5000	4000	3000	2000	1000	800	600	400	200	100
≥ 90	75.2	72.0	67.3	59.0	42.8	36.7	30.2	22.5	13.9	8.5
= 80	68.0	66.3	62.5	55.5	40.8	35.0	28.6	21.5	13.2	8.1
= 70	60.4	59.0	56.8	51.4	38.7	33.2	27.0	20.4	12.5	7.7
= 60	53.0	51.8	49.3	45.0	36.0	30.9	25.2	19.0	11.7	7.2
= 50	44.8	43.6	41.5	38.4	32.0	27.5	22.4	16.9	10.4	6.4
= 40	36.5	35.5	34.5	33.0	27.0	23.2	18.9	14.2	8.8	5.4
= 30	28.0	27.3	26.9	26.3	21.4	18.4	15.0	11.3	6.9	4.3
= 20	18.0	17.7	17.4	16.7	15.2	13.0	10.6	8.0	4.9	3.0

the appropriate influence coefficients for the missile at various levels are given:

$$E = \sum Ci\ V_i \qquad (17.10)$$

where Ci is the influence coefficient at the ith level that describes the portion of the total response of a missile assignable to that level, and V_i represents the mean of the component wind speed at that level. The variation around this average effect caused by day-to-day fluctuations in the winds is obtained from

$$\sigma^2_{INT} = \sum_{i,j} C_i\ C_j\ r_{ij}\ \sigma_i\ \sigma_j \qquad (17.11)$$

where σ^2_{INT} is the integrated variance for all levels considered, C_i and C_j are the influence coefficients at the ith and jth levels, σ_i and σ_j are the standard deviations of the component wind at these levels, and r_{ij} is the correlation between the component wind at the ith level and that at the jth level. The square root of the solution to this equation yields the standard deviation for each component of the ballistic wind. The two components can be combined and used to determine the probability of occurrence of deviations of any desired magnitude from a trajectory or impact point based on mean monthly winds. In these computations, it is assumed that the cross-component correlations are zero at and between levels, and the wind frequency distributions are essentially circular normal.

The wind climatology necessary for determination of ballistic effects consists of statistical arrays of mean monthly north-south and east-west wind components, their standard deviations, and interlevel correlations between the same component at different levels. This information has been prepared in matrix form for a relatively large number of locations. Examples for levels between the surface and 60 km are shown in Table 17-17 for the month of January at Ft. Churchill, Wallops Island and Ascension Island. Winds are lighter in summer at middle and high latitudes. For targeting purposes, the wind data must pertain to the locations of interest. For design purposes, however, a representative sample of data from the various climatic regions should be used.

Table 17-16. Envelopes of 99% wind speed change (m/s), 1–80 km altitude region, for All five locations [Kaufman, 1977].

Wind Speed at Reference Altitude (m/s)	Scales of Distance (m) Thickness									
	5000	4000	3000	2000	1000	800	600	400	200	100
≥ 90	77.5	74.4	68.0	59.3	42.8	36.7	30.2	22.5	13.9	8.5
= 80	71.0	68.0	63.8	56.0	40.8	35.0	28.6	21.5	13.2	8.1
= 70	63.5	61.0	57.9	52.0	38.8	33.2	27.0	20.4	12.5	7.7
= 60	57.1	54.7	52.3	47.4	36.0	31.0	25.3	19.0	11.7	7.2
= 50	49.6	47.8	46.2	43.8	33.0	28.3	23.2	17.5	10.7	6.6
= 40	39.4	38.8	37.9	35.5	29.5	25.3	20.6	15.5	9.6	5.9
= 30	30.0	30.0	29.4	26.9	22.6	19.4	15.8	12.2	7.3	4.6
= 20	20.0	19.8	19.5	18.4	15.2	13.1	10.9	9.0	6.3	4.3

Table 17.17a. Zonal Winds from the surface to 60 km at Ft. Churchill.

Correlation at Pairs of Levels for Jan 1969–1976
Fort Churchill, Manitoba
East-West Wind M/S West +
KM Kilometers Above Sea Level
MEAN Average of Observed Values
STDV Standard Deviation of Values Times 10
N Number of Values at Each Altitude

KM	.035	2	4	6	8	10	12	14	16	18	20	22	24	26	28	30	32	34	36	38	40	42	44	46	48	50	52	54	56	58	60
MEAN	4	4	7	10	12	13	14	15	16	17	17	17	20	25	24	25	24	25	25	28	30	26	31	35	35	38	39	39	37	27	30
STDV	32	64	98	132	140	103	99	106	129	137	170	199	207	248	281	305	301	308	324	337	353	366	395	410	427	447	440	435	418	330	324
N	50	50	51	52	52	52	51	50	49	46	44	43	38	52	53	52	53	53	53	53	53	49	52	53	52	53	52	53	49	44	43
2	54	**																													
4	33	81																													
6	23	67	95																												
8	18	59	87	96																											
10	17	45	71	82	92																										
12	15	36	55	64	76	91																									
14	5	15	34	43	60	80	91																								
16	0	6	23	30	48	68	82	96																							
18	4	10	18	16	26	54	72	86	92																						
20	3	5	15	15	24	50	66	80	87	97																					
22	4	6	12	11	21	46	62	74	82	95	98																				
24	1	−6	−5	−7	5	36	55	68	76	90	94	98																			
26	−1	6	13	17	30	46	59	66	74	82	87	90	92																		
28	−2	5	10	14	28	44	59	65	73	81	86	69	90	99																	
30	2	4	9	12	25	43	56	64	73	76	81	84	84	96	98																
32	6	10	9	10	22	38	49	55	63	70	75	77	79	92	94	97															
34	5	12	11	12	23	38	46	52	58	66	71	74	76	88	91	94	98														
36	6	12	9	10	20	35	40	45	51	55	60	63	64	79	83	88	93	96													
38	3	10	4	7	16	29	32	37	42	44	50	54	57	73	76	81	89	92	98												
40	3	15	6	9	16	25	23	23	26	27	34	37	41	60	63	70	78	83	91	95											
42	1	12	1	4	8	9	1	8	11	10	19	23	26	42	46	54	66	70	81	88	95										
44	10	17	6	7	10	14	6	6	7	8	16	20	26	37	40	49	62	67	75	82	90	96									
46	6	7	−1	0	3	7	−3	−2	0	2	9	13	21	30	31	40	53	58	67	74	83	90	96								
48	15	9	0	1	0	3	−8	−7	−8	−6	0	5	15	23	23	32	46	52	61	68	78	85	92	97							
50	13	9	−1	−4	−6	0	−11	−9	−10	−7	−3	1	14	19	17	25	41	46	55	62	71	78	86	91	96						
52	11	4	−5	−7	−8	1	−10	−7	−9	−7	−3	1	13	14	13	22	37	43	53	59	67	76	82	88	93	97					
54	14	1	−7	−9	−9	−4	−16	−8	−8	−9	−5	4	12	7	6	14	27	31	41	49	56	68	75	82	88	92	95				
56	12	2	−14	−13	−13	−13	−26	−20	−22	−25	−20	−14	1	2	0	9	23	28	39	48	57	73	76	80	86	90	90	95			
58	15	−2	−18	−18	−16	−10	−12	−11	−11	−21	−21	−16	15	6	−2	5	18	20	27	38	42	53	58	65	75	80	81	86	93		
60	15	−5	−23	−22	−19	−13	−14	−13	−12	−17	−14	−7	28	12	5	10	23	26	32	43	44	51	58	68	75	79	79	85	91	94	

**Multiply tabular values by 0.01 to obtain correlation coefficients

Table 17.17b. Zonal Winds from the surface to 60 km at Wallops Island.

Correlation at Pairs of Levels for Jan 1969–1976
Wallops Island, VA
East-West Wind M/S West +
KM Kilometers Above Sea Level
MEAN Average of Observed Values
STDV Standard Deviation of Values Times 10
N Number of Values at Each Altitude

KM	.015	2	4	6	8	10	12	14	16	18	20	22	24	26	28	30	32	34	36	38	40	42	44	46	48	50	52	54	56	58	60
MEAN	1	12	21	28	34	31	33	28	23	15	11	11	11	14	16	19	24	28	31	34	37	40	45	50	54	57	59	62	63	68	76
STDV	30	61	90	123	150	120	109	96	88	76	74	81	95	140	170	199	236	254	269	286	279	291	287	300	303	308	290	291	282	282	313
N	44	44	44	43	41	29	25	22	21	20	21	19	22	42	43	44	44	44	44	44	44	44	44	44	44	44	44	44	40	34	25
2	25	**																													
4	31	85																													
6	39	68	94																												
8	34	59	85	94																											
10	−4	31	60	77	91																										
12	−21	18	32	44	68	77																									
14	−21	17	49	62	83	89	87																								
16	−14	4	32	51	67	76	66	88																							
18	−13	−29	5	31	53	72	62	75	75																						
20	−18	−34	−5	12	12	49	52	76	85	93																					
22	−11	−17	5	17	14	55	57	81	89	93	98																				
24	−3	−19	−11	10	21	57	63	72	73	87	92	95																			
26	7	16	14	18	20	39	46	40	42	67	30	38	88																		
28	12	17	19	26	30	45	44	32	24	61	21	32	83	95																	
30	10	18	18	26	32	44	39	27	20	51	17	30	72	89	96																
32	14	18	23	37	41	48	38	25	20	53	18	28	66	82	91	97															
34	11	16	24	38	42	46	36	21	19	52	18	23	59	73	83	90	97														
36	8	16	26	37	40	41	42	29	23	55	22	33	53	63	75	83	90	96													
38	3	11	22	30	31	38	46	32	25	52	20	29	48	55	66	72	79	86	95												
40	1	18	29	33	30	28	36	25	12	36	−2	4	33	46	57	60	68	75	84	93											
42	2	13	23	24	20	9	16	8	−3	23	−19	−17	18	32	40	41	50	58	68	81	95										
44	−3	9	18	18	13	−1	14	9	5	15	−21	−21	13	18	22	23	33	41	53	69	86	96									
46	−2	10	18	17	14	−13	5	4	2	7	−25	−32	5	3	4	5	15	24	35	52	72	85	95								
48	−2	6	14	13	8	−16	0	7	9	7	−16	−22	1	−5	−5	−5	4	12	23	41	61	76	88	97							
50	−8	0	8	6	1	−20	−7	7	9	14	−2	11	−1	−8	−10	−11	−4	4	13	30	50	67	80	89	96						
52	−3	7	15	12	5	−13	−3	12	13	13	−6	12	−3	−10	−10	−11	−4	4	14	31	51	67	79	87	94	98					
54	−1	13	19	14	6	−16	−9	5	5	0	−18	−21	−11	−10	−9	−9	−3	5	15	30	52	66	76	84	91	92	97				
56	−1	20	20	12	5	−16	−10	5	10	11	−11	−17	−6	2	0	−3	−1	6	11	24	47	60	70	76	85	87	93	96			
58	9	23	19	14	15	−9	0	4	1	9	−6	−9	18	18	19	17	17	21	21	32	52	59	63	66	76	78	84	89	93		
60	0	28	31	26	32	−4	−1	9	2	−8	−6	−13	9	9	12	8	10	16	12	18	39	45	52	60	73	78	84	87	90	96	

**Multiply tabular values by 0.01 to obtain correlation coefficients

Table 17.17c. Zonal Winds from the surface to 60 km at Ascension Island.

Correlation at Pairs of Levels for Jan 1969–1976
Ascension Island
East-West Wind M/S West +
KM Kilometers Above Sea Level
MEAN Average of Observed Values
STDV Standard Deviation of Values Times 10
N Number of Values at Each Altitude

KM	.079	2	4	6	8	10	12	14	16	18	20	22	24	26	28	30	32	34	36	38	40	42	44	46	48	50	52	54	56	58	60
MEAN	−6	−3	−4	−5	−4	1	6	9	0	−7	−10	−14	−17	−15	−15	−18	−22	−27	−31	−34	−41	−50	−60	−68	−73	−65	−45	−29	−15	−2	4
STDV	16	37	42	34	67	98	113	130	70	45	92	113	126	102	120	147	139	134	118	110	111	88	100	139	177	206	204	189	178	173	161
N	42	43	43	43	43	43	43	43	43	43	43	43	41	43	42	43	43	43	43	43	43	43	43	43	43	43	43	43	39	30	26
2	12	**																													
4	33	30																													
6	23	33	28																												
8	23	28	7	55																											
10	15	8	−9	30	77																										
12	11	−3	−5	37	58	86																									
14	−4	−22	−23	14	40	68	82																								
16	−8	0	−16	22	34	59	67	82																							
18	−12	19	−24	12	7	10	5	8	20																						
20	−2	18	−14	−10	−18	−10	1	0	4	48																					
22	2	22	−2	−4	8	7	14	11	11	38	85																				
24	9	28	21	17	40	26	25	16	13	27	47	84																			
26	12	−14	22	−10	19	29	27	25	−6	−23	−7	18	42																		
28	15	−18	11	−1	18	21	12	24	1	−30	−61	−39	−4	61																	
30	1	−23	−4	−5	11	19	9	27	13	−35	−72	−65	−37	34	89																
32	3	−22	−11	4	18	28	15	30	22	−20	−73	−68	−40	26	81	95															
34	3	−24	−16	5	14	20	5	12	5	−17	−75	−77	−53	7	65	76	86														
36	3	−26	−5	9	7	7	−4	4	0	−18	−74	−78	−60	−12	50	59	68	91													
38	−9	−33	−14	5	−7	−7	−6	2	−6	−20	−59	−71	−64	−24	30	39	45	73	87												
40	−14	−9	−22	14	−11	−14	−12	−16	−19	17	−20	−35	−40	−37	2	−1	13	45	58	76											
42	−13	23	3	7	−16	−10	−5	−14	−3	42	22	5	−7	−34	−27	−27	−15	4	8	19	57										
44	−5	21	16	−3	0	−2	8	−7	1	25	34	28	17	−21	−41	−48	−40	−19	−9	−3	26	53									
46	−2	2	19	−12	−1	−12	−4	−7	7	12	21	24	18	−23	−34	−35	−36	−34	−21	−18	−16	−2	51								
48	3	6	3	−8	−1	−24	−13	−16	−11	9	33	35	19	−31	−48	−50	−51	−41	−27	−22	−15	0	46	75							
50	4	20	−8	0	9	−21	−18	−22	−19	3	22	23	10	−34	−36	−36	−36	−26	−17	−13	2	9	37	44	82						
52	−1	31	−16	10	13	−17	−14	−19	−17	−4	7	5	−9	−36	−31	−26	−23	−10	−3	4	26	24	32	16	51	78					
54	−11	40	−13	16	6	−14	−10	−20	−11	−7	3	−2	−17	−47	−42	−31	−27	−15	−6	6	33	31	27	0	23	44	82				
56	−24	42	−3	10	−5	−23	−15	−16	−5	−13	1	−7	−14	−45	−45	−23	−27	−27	−20	−8	1	14	5	−2	22	34	50	72			
58	−14	14	5	13	22	−1	9	2	−10	−13	1	2	7	−10	−34	−30	−33	−28	−21	−8	−5	−11	28	6	34	41	34	35	75		
60	−5	4	0	8	18	−9	1	−2	−15	−11	−4	2	7	−4	−28	−28	−30	−19	−8	−6	−12	−20	28	13	40	42	21	10	46	83	

**Multiply tabular values by 0.01 to obtain correlation coefficients

17.4 DESIGN DATA ON WINDS

Wind statistics are presented in a variety of ways, each of which is intended for maximum usefulness for particular aspects of design and operational problems. In "Upper Wind Statistics," Crutcher [1959] presents northern hemisphere charts of some 15 wind variables or statistics. For surface winds, in the "Climatic Atlas of the United States," the National Weather Service [1968] presents monthly and annual charts of the prevailing direction, mean wind speed, the fastest wind on record and its direction, and wind roses that give the frequency distribution of the wind by direction including frequency of calm, the mean wind vector and direction. There is also a table of the frequencies of 9 categories (Beaufort) of wind speeds for some 120 U.S. stations.

Generally speaking, any data source on surface wind speed is limited to providing several key parameters from which the general frequency distribution of the wind, in speed and direction, can be estimated or reconstructed. But to do so, a practical model of the distribution of the wind speed must be adopted. Three such models are the gamma distribution, Weibull distribution, and the circular normal bivariate distribution. Each has its merits and drawbacks.

17.4.1 Hourly Surface Wind Speeds

The distributions of surface wind speeds, observed every hour on the hour, have been studied by many climatologists and statisticians whose conclusions and consequent models differ. Some favor the distribution of wind speeds as given by the circular bivariate normal distribution, others the log-normal, still others the gamma distribution. A historical record of at least 5 years should be used to obtain good estimates of wind speed distributions, especially small probabilities (for example 1%). Although there are about 600 city and airport stations in the United States where hourly records are kept, they generally represent wind fields inadequately. A location that is close to a weather reporting station should have similar wind characteristics, but terrain effects including manmade effects, and proximity to large bodies of water superimpose a spatial variability that is difficult to generalize. Fairbanks, Alaska, for example, has a mean wind speed in January of 0.9 m/s with standard deviation 1.7 m/s. Yet Big Delta, only 121 km away, has a mean wind speed of 5.4 m/s and standard deviation 4.9 m/s.

The following are alternative models of windspeed frequency distribution:

Model Alternative 1: A gamma distribution. In terms of the mean wind speed $\overline{V}_s$ and standard deviation s_s, the probability density function of the wind speed V_s is given in terms of a transformed variable y by

$$f(y) = 0.5\, y^2\, e^{-y}, \qquad (17.12)$$

$$\text{where } \frac{(y-3)}{\sqrt{3}} = \frac{V_s - \overline{V}_s}{s_s}. \qquad (17.13)$$

The cumulative probability of wind speed, $P(V_s)$, equal to or less than V_s is given by

$$P(V_s) = 1 - e^{-y}\left(1 + y + \frac{y^2}{2}\right). \qquad (17.14)$$

As an example, in the month of January, the noontime Bedford, Mass., wind has a mean hourly speed $\overline{V}_s$ of 5.1 m/s and standard deviation s_s of 3.5 m/s. Equation (17.14) gives the cumulative probability for several values of the wind speed as follows:

V_s m/s	y	Estimated $P(V_s)$	Observed Distribution
calm	0.445	0.011	0.115
1.5	1.219	0.125	0.168
3.1	1.993	0.321	0.322
5.2	3.03	0.583	0.592
8.2	4.57	0.834	0.838
10.8	5.89	0.932	0.946
13.9	7.41	0.978	0.989
17.0	8.96	0.9936	0.999

This kind of approximation is good for moderate to strong wind speeds and is generally useful except for very light winds or calm conditions.

Model Alternative 2: A Weibull Distribution. A recent study [Bean and Somerville, 1979] has produced the model

$$P(V_s) = c + (1 - c)\,[1 - \exp(-\alpha v_s^{\beta})] \qquad (17.15)$$

where c is the probability of calm, and α and β are parameters of the Weibull distribution that are determined either to make the model fit the observed frequencies of wind speed (in a least squares sense), or are estimated in other effective ways. The records of many stations indicate a high probability of "calm," which makes this formulation desirable.

Records like the "Revised Uniform Summaries of Surface Weather Observations" (RUSSWO) (Compiled by the Environmental Technical Applications Center, Scott AFB, Ill.) contain the relative frequencies f_i of each of 11 or fewer winds speeds V_s. Where x_i, the middle value in the category, is used for the ith category of V_s, formulas have been found for α and β as follows:

$$\hat{\alpha} = \frac{\sum f_i}{\sum f_i\, x_i^{\beta}}$$

$$\hat{\beta} = \left[\frac{\sum f_i \cdot x_i^{\beta} \ln x_i}{\sum f_i\, x_i^{\beta}} - \frac{\sum f_i \ln x_i}{\sum f_i}\right]^{-1} \qquad (17.16)$$

To solve for α and β, an initial guess is entered for β in the right-hand side of Equation (17.16), and the equation is solved for a first estimate of β. With this revised estimate, the equation is solved again for a second and better estimate, and so on, until the value of β is stabilized.

The RUSSWO for Bedford, Mass., January at noontime, gives f_i for categories of V_s (or x_i) which, when entered in Equation (17.16) produced the following values after several iterations:

$$\hat{\beta} = 1.961$$

$$\hat{\alpha} = 0.02512$$

When these values for α and β are entered in Equation (17.15) together with $c = 0.115$, the probabilities $P(V_s)$ become

V_s (m/s)	$P(V_s)$	Observed Distribution
calm	0.115	0.115
1.5	0.166	0.168
3.1	0.297	0.322
5.2	0.527	0.592
8.2	0.816	0.838
10.8	0.9395	0.946
13.9	0.989	0.989
17.0	0.9987	0.999

Model Alternative 3: The circular normal distribution. The assumption of the circular normal distribution for the wind implies that the zonal u and meridional v components each have a normal Gaussian distribution with individual means $\bar{u}$ and $\bar{v}$ but with the same standard deviation s. The two components are independently distributed. As a consequence the probability density function of each is

$$f(u) = \frac{\{\exp[-(u-\bar{u})^2/2]\}}{\sqrt{2\pi}}$$

$$f(v) = \frac{\{\exp[-(v-\bar{v})^2/2]\}}{\sqrt{2\pi}}. \qquad (17.17)$$

The magnitude of the mean wind vector ($\bar{V}$) is given by

$$|\mathbf{V}| = \sqrt{\bar{v}^2 + \bar{u}^2}. \qquad (17.18)$$

The standard vector deviation (s_v) is simply

$$s_v = s\sqrt{2} \qquad (17.19)$$

The mean wind speed $\bar{V}_s$ and the standard deviation of the wind speed s_s are not easily derived from the components. The cumulative probability $P(V_s)$ of the wind speed, however, can be given in terms of $\bar{V}$ and s or s_v. One of the most applicable formulas is

$$P(V_s) = e^{-y} \sum_{n=0}^{10} \frac{y^n}{n!} \left[1 - e^{-x} \sum_{m=0}^{n} \frac{x^m}{m!} \right], \qquad (17.20)$$

where $x = V_s^2/s_v^2$,

$y = |\bar{\mathbf{V}}|^2/s_v^2$.

In the example of Bedford, Mass. January noontime winds, the RUSSWO table of wind speed versus wind direction yields

$$|\bar{\mathbf{V}}| = 2.9 \text{ m/s}$$

$$s_v = 5.1 \text{ m/s}$$

or $s = 3.6$ m/s

as opposed to $V_s = 5.1$ m/s

$s_s = 3.7$ m/s.

When the values for $|\bar{\mathbf{V}}|$ and s_v are used in Equation (17.20) the probabilities $P(V_s)$ become

V_s m/s	$P(V_s)$	Observed
1.5	0.063	0.168
3.1	0.231	0.322
5.2	0.521	0.592
8.2	0.853	0.838
10.8	0.964	0.946
13.9	0.9936	0.989
17.0	0.9965	0.999

The distribution of the wind V around the mean wind vector ($\bar{\mathbf{V}}$) is sometimes of prime interest as it would be in targeting. It is the difference between the actual vector wind and the mean vector wind and has the distribution

$$P(V) = 1 - \exp\left(-\frac{v^2}{s_v^2}\right) \qquad (17.21)$$

Thus a circle of radius equal to one standard vector deviation, drawn about the tip of the mean wind vector, would encompass 63% of the population of winds. Half of the wind vectors will fall within a circle of radius 0.83 times the standard vector deviation.

17.4.2 Surface Wind Direction

Winds tend to have a modal direction, like the trade winds or the prevailing westerlies. Using the model of the bivariate normal distribution, the estimate of the frequency

$P(\theta_1 \leq \lambda < \theta_2$ of the wind direction λ between directions θ_1 and θ_2 is given by

$$P(\theta_1 \leq \lambda < \theta_2) = (1/\sqrt{2\pi}) \cdot \sum_{u=0}^{umax} [\exp - \frac{(\bar{u} - u)^2}{2} \delta u][F(x_2)) - F(x_1)] \quad (17.22)$$

where $u = V/s$,

V is the wind component in the direction (θ_0) of the mean wind vector $\bar{V}$, and s is the standard deviation of the appropriate wind component,

$\bar{u} = |\bar{V}|/s$,
δu is a small increment of u,
$x_2 = \tan(\theta_2 - \theta_0)$,
$x_1 = \tan(\theta_1 - \theta_0)$,

and F(x) is approximated by

$$F(x) = 1 - 0.5(1 + c_1x + c_2x^2 + c_3x^3 + c_4x^4)^{-4}$$

where

$c_1 = 0.196854$
$c_2 = 0.115194$
$c_3 = 0.000344$
$c_4 = 0.019527$

In the example for Bedford, Mass., January noontime wind $\theta_o = 300°$. After correcting for calm frequency of 0.115, the computed frequencies of wind directions were as follows:

Direction	$P(\theta_1 \leq \lambda < \theta_2)$	Observed
N	0.082	0.067
NNE	0.056	0.041
NE	0.027	0.040
ENE	0.027	0.013
E	0.022	0.019
ESE	0.019	0.010
SE	0.018	0.014
SSE	0.020	0.009
S	0.025	0.022
SSW	0.032	0.051
SW	0.036	0.067
WSW	0.070	0.063
W	0.098	0.108
WNW	0.122	0.143
NW	0.126	0.110
NNW	0.110	0.106

17.4.3 Surface Wind Gusts

Studies on the relationship of gusts to the steady wind speed are in general agreement; however, quantitative results have varied depending on the data and the analytical methods used. Sissenwine et al. [1973] reviewed the results of many of these; he also presented a comprehensive analysis of gustiness based on actual wind records during periods of strong winds, observed at 14 airfields in the Northern Hemisphere between 14° and 77° latitude. Tattelman [1975] analyzed the same data to develop 50%, 75%, 90%, and 98% gust factor curves for 5-min, 1-min, and 30-s average (or steady) wind speeds. Gust speeds reported in weather observations are normally considered to be about 2-s averages, but for designers of various sized equipment, other short duration gusts may be applicable.

Since resolution of the wind records was approximately 2 s the shortest period gusts were considered to be 2-s wind speeds. Gust factor (GF) curves were fitted using the equation

$$GF = 1 + Ae^{-BV}, \quad (17.23)$$

where A and B are constants, and V is the speed of the steady wind. The values for B were dertermined by a least squares fit of all the data to the 5-min, 1-min, and 30-s speeds. Using these values of B, the value for A was determined for each percentile curve by a least squares fit to the mid-class wind speed values (for example, 12.6 m/s for V = 10.3–14.9 m/s) and weighted for the number of observations at each point. Figure 17-13 shows curves of the 30-s gust factor as related to the 5-min steady speed, and the 1-min gust factor related to the 5-min speed using all the data. Figure 17-14 shows the relationship between the 2-s gust factor and the 5-min steady speed. Curves in both

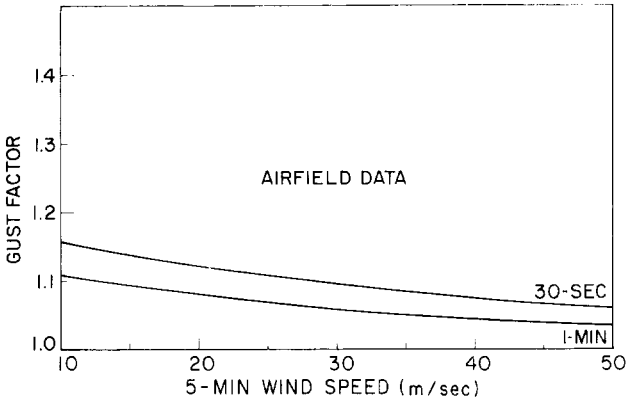

Figure 17-13. Curves of the 30-s and 1-min gust factor to 5-min wind speed for the airfield data fitted to $GF = 1 + Ae^{BV}$ [Tattelman, 1975].

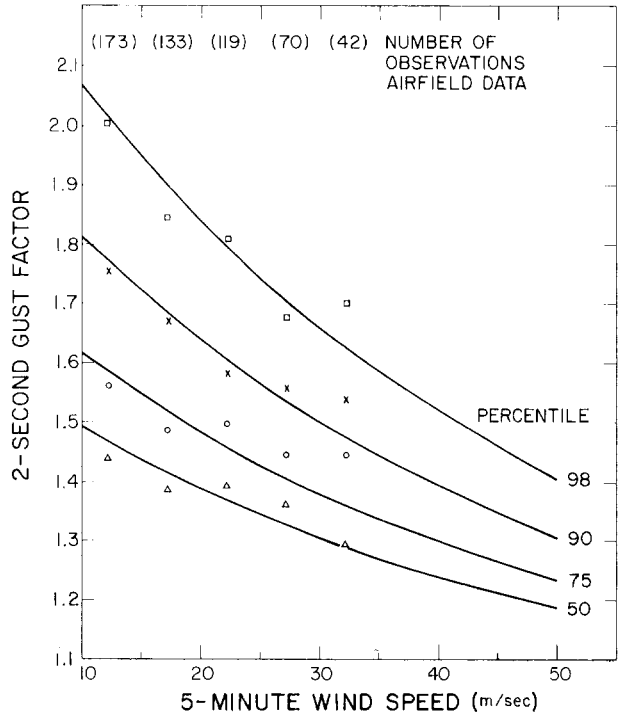

Figure 17-14. Relationship between the 2-s gust factor and the 5-min wind speed at indicated percentiles for the airfield data. (Data were fitted to $GF = 1 + Ae^{-Bv}$ and weighted for the number of observations at each mid-class value).

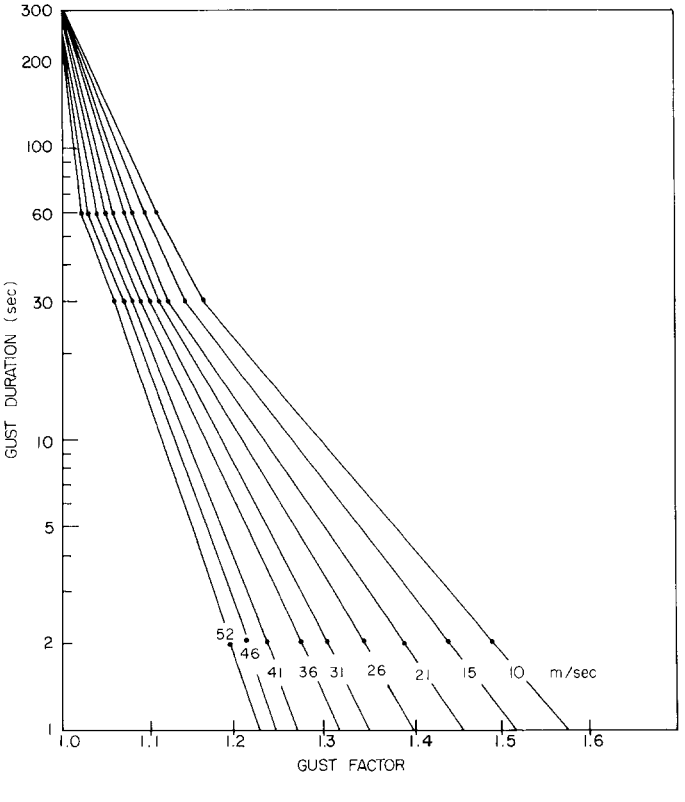

Figure 17-15. Expected (50%) gust factors versus gust duration and 5-min steady speed.

figures extend beyond the limit of the wind data, for which the highest steady speed is 35 m/s.

Sherlock [1947] found that a gust must have a duration such that its size is about 8 times the downwind dimension of a structure in order to build a force on the structure commensurate with the gust speed. Because the orientation of most equipment will not be taken into consideration, the shortest horizontal dimension of the equipment should be considered as the downwind dimension. For example, if a structure has a 5-m downwind dimension, a gust must be 40 m long to build up full dynamic pressure. Therefore, a speed of 40 m/s would build up full force on such a structure in only 1 s; a speed of 20 m/s would require 2 s. Figure 17-15 shows the expected (50%) gust factors versus gust duration and 5-min steady speed to aid in calculating the design windspeed for structures of differing downwind dimensions. The curves were drawn to four points: a gust factor of 1.0 at 300 s, the 60-s and 30-s gust factors for each speed from Figure 17-13, and the 2-s, 50% gust factors from Figure 17-14. Lines on Figure 17-15 were extended from the 2-s gust factors to include 1-s gust factors.

Tattelman [1975] also presented curves of the 50%, 75%, 90%, and 98% wind speed range (the difference between the maximum and minimum 2-s speed) as a function of time interval and mean 5-min wind speed. The 90% wind speed range is shown in Figure 17-16. The dashed lines indicate extrapolation beyond the limits of the data. The gust factor and wind speed range curves in this section are considered applicable to most airport locations at the average height of the data used, 15 m.

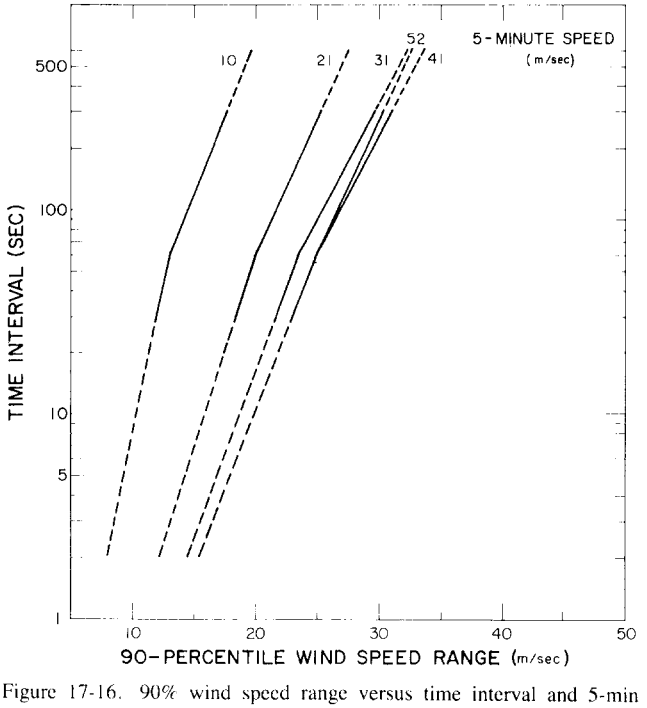

Figure 17-16. 90% wind speed range versus time interval and 5-min speed.

17.4.4 Extreme Surface Wind Speeds

Various statistics are used for the daily maximum wind speed. One statistic is the maximum 5-min wind of the 288 5-min intervals of one day. Another popular measure is the *fastest mile,* which is the reciprocal of the shortest interval (in 24 h) that it takes one mile of air to pass a given point. The *strongest gust* is the highest reading of an instantaneous recording anemometer. There is no unique relation between these units. The Washington, D.C. records show that, for speeds greater than 15 m/s, the maximum 5-min wind speed is roughly 0.93 times the fastest mile and roughly 0.67 times the strongest gust. The maximum 1-min wind speed is roughly 0.71 times the strongest gust. Canadian and British records show the maximum 1-h wind speed to be 0.62 times the strongest gust.

A model distribution of the annual extreme has been the subject of conflicting viewpoints. The most favored distribution is the Fisher-Tippett Type I, now generally known as the Gumbel Distribution. If x is the symbol for the annual extreme, then the cumulative probability of x is given by

$$P(x) = \exp[-\exp(-y)] \qquad (17.24)$$

where y is the *reduced variate,* whose mean is $\bar{y} = 0.5772$ and whose standard deviation is $\sigma_y = 1.28255$.

A relatively simple equation can be used to relate x to y:

$$\frac{(y - \bar{y})}{\sigma_y} = \frac{(x - \bar{x})}{s_x} \qquad (17.25)$$

where $\bar{x}$ and s_x are the mean and standard deviation, respectively, of the annual extremes (x).

The work that is implied to make adequate estimates of percentiles of x is to find the sample mean and standard deviation of a set of N extremes for N years. Other approaches, although more rigorous, require ordering the N extremes by magnitude and/or estimating parameter values by successive approximations. Estimates also might depend directly on sample size.

To judge the risk of an extreme event in n years, then Equation (17.24) above is replaced by

$$P(x;n) = \exp[-n\exp(-y)]. \qquad (17.26)$$

To estimate x for probability P in n years, or an n-year risk (1-P), and knowing the annual extreme mean $\bar{x}$ and standard deviation (s_x), Equation (17.25) then gives

$$\hat{x} = \bar{x} + s_x \frac{(y - \bar{y})}{\sigma_y}, \qquad (17.27)$$

where

$$y = \ell n\,(n) - \ell n(-\ell n\,(P)). \qquad (17.28)$$

As an example, a 19-yr record at Denver, Colorado shows an average annual 5-min wind speed maximum 15 m above ground level of 19.6 m/s and standard deviation 2.5 m/s. If a tower is to be built to last for 25 years, with 99% certainty of survival throughout the 25 years, then the critical wind speed, given by Gumbel model (Equations (17.28), (17.27)), is estimated at 33.7 m/s.

An estimate is subject to sampling variations, in the above example a 19-yr sample. One standard error of this estimate s(x) is approximately

$$s(\hat{x}) = s_x\sqrt{\alpha/N}$$

where N is the number of years, and α is given by

$$\alpha = 0.710 + 0.116y + 0.669\,y^2.$$

In the Denver example, the standard error of the estimate (33.9 m/s) is approximately $s(x) = 3.8$ m/s, or 11% of the estimate itself. A brief meteorological record of annual extremes permits estimates only within confidence bands that vary with the size of the record.

Publications by climatic agencies such as NOAA Environmental Data Service and the Canadian Meteorological Service give extreme values. Yet each permanent installation might require a special study for a particular site and/or for a particular design problem. For example, the extreme annual wind speed at Logan airport (Boston) would be an underestimate, by about 33%, of the extreme on Blue Hill, 19 km to the south-southwest. Even the record at the exact location of interest may not be representative of the wind effects on a tall (or short) structure.

Table 17-18 gives means and standard deviations of annual extreme wind speeds and peak gusts at some representative stations around the world including stations that are typically in the paths of hurricanes. The 1% risk in 10 yrs was computed by the above formula, assuming the Gumbel distribution. This column is virtually the same as for the 1000-yr return period, and thus is the speed that has only 1/10 of 1% chance of being exceeded each year. There is a noticeable difference between the extreme speeds at airports and at city stations, attesting to the effects of tall buildings in the cities. The reduction of speed might be as high as 55%, but averages roughly 25%.

Tornadoes are severe whirlwinds, typically a hundred meters in diameter, which fortunately are rare accompaniments of severe thunderstorms. They are most common in Australia and the United States where they number some 140 to 150 per year, most frequent in spring in the plains area of the United States between the Rockies and the Appalachians. The wind speeds are generally less than 110 m/s in the lowest 10–20 m above the ground. Speeds up to 140 m/s occur occasionally in very severe tornadoes; higher wind speed estimates are generally suspect [Golden, 1976]. These high wind speeds place them outside the distributions

Table 17-18. Extreme annual wind speed (fastest m/s) at 15.2 m above ground at the given stations; (A) denotes airport station.

Station	Years of Record	Mean (m/s)	S.D. (m/s)	1% Risk in 10 yr (m/s)
Tampa, Fla (A)	1941–56	23	3.9	42
Miami, Fla	1943–58	24	8.0	64
Wilmington, N.C. (A)	1951–58	30	7.1	65
Hatteras, N.C.	1912–57	28	6.0	58
Dallas, Tex (A)	1941–58	23	2.9	38
Washington, D.C. (A)	1949–58	22	3.8	41
Dayton, Ohio (A)	1944–58	27	3.8	46
Atlanta, Ga. (A)	1933–58	22	3.3	39
Abilene, Tex (A)	1945–58	28	6.1	59
Columbia, Mo (A)	1949–58	25	2.8	39
Kansas City, Mo	1934–58	25	3.1	40
Buffalo, N.Y. (A)	1944–58	26	3.7	44
Albany, N.Y. (A)	1938–58	23	3.8	42
Boston, Mass (A)	1936–50	26	5.4	53
Chicago, Ill. (A)	1943–58	23	2.5	35
Cleveland, Ohio (A)	1941–58	26	2.6	39
Detroit, Mich (A)	1934–58	22	2.6	34
Minneapolis, Minn (A)	1938–58	23	5.0	48
Omaha, Nebraska (A)	1936–58	26	5.9	55
El Paso, Tex (A)	1943–58	26	2.0	36
Albuquerque, N.M. (A)	1933–58	27	4.6	50
Tucson, Ariz	1948–58	22	3.2	38
San Diego, Calif	1940–58	16	2.7	30
Cheyenne, Wyo	1935–58	28	3.1	43
Rapid City, S.D.	1942–58	30	3.0	44
Bismarck, N.D.	1940–58	30	2.3	41
Great Fall, Mont.	1944–54	29	1.6	37
Portland, Ore	1950–58	25	3.0	41
New York, N.Y.	1949–58	26	2.1	37
Pittsburgh, Pa.	1935–52	23	2.8	37
	Number of Years of Data			
Fairbanks, Alaska	9	17	3.7	35
Nome, Alaska	11	27	4.1	47
Elmendorf AFB, Alaska	14	20	3.2	36
Shemya Island, Alaska	10	31	7.8	45
Hickam AFB, Hawaii	17	20	3.8	38
Clark AB, Philippines	13	17	5.5	45
Lajes Field, Azores	13	28	7.6	65
Albrook AFB, Canal Zone	18	12	1.8	21
San Pablo, Spain	11	34	6.8	68
Wheelus AB, Libya	14	22	5.3	48
Stuttgart, Germany	15	18	2.1	29
Keflavik, Iceland	9	38	4.8	62
Thule, Greenland	14	36	5.5	63
Tainan, Formosa	39	24	9.5	71
Taipei, Formosa	39	26	9.8	75

Table 17-18. *(Continued)*

Station	Years of Record	Mean (m/s)	S.D. (m/s)	1% Risk in 10 yr (m/s)
Itazuke AB, Japan	14	19	4.5	42
Misawa AB, Japan	11	21	3.2	37
Tokyo Intl. Airport, Japan	15	23	5.5	46
Kimpo AB, Korea	8	19	3.6	37
Bombay, India	6	22	6.3	54
Calcutta, India	6	25	3.3	42
Gaya, India	6	23	3.0	38
Madras, India	6	20	3.4	37
New Delhi, India	6	23	1.7	31
Poona, India	6	17	2.7	31
Central AB, Iwo Jima	17	35	16.9	119
Kadena AB, Okinawa	14	37	11.3	93

discussed previously. Their small dimensions and infrequent occurrence make it impossible to state precise probabilities of occurrence at specific locations. Statistics of occurrence on an areal basis have been developed by Abbey [1976] and Kelly et al. [1978].

Hurricanes, while much more frequent, larger, and more predictable, still cause problems for the statistical analyst. Recent studies at the National Bureau of Standards suggest that the Gumbel (Type I) distribution of extreme winds does not provide as good a description of the extreme wind distributions when they must include hurricane winds. The departures of the winds from the Gumbel estimates tend to be on the weaker side. This means that the estimates of Table 17-18 should be used with caution. Hurricanes may strike at some stations while missing others, so that the record extreme wind speeds of one station may not represent the potential risk of still stronger winds at another nearby station or even at the same station. We conclude, however, that the Gumbel distribution is the best single model for all extreme winds data including hurricane winds.

Directly recorded data for record wind extremes are rare due to damage or destruction of the wind measuring instruments and power outages, during an event such as a tornado or hurricane. Newspaper reports give estimates whose reliability is unknown and variable. Some might be from a weather station where visually observed wind-speed dials were still in operation even though the recorder lost power. Others might be calculated from the amount of force required to blow over a building or tree or to drive a metal rod through a wooden post.

The recognized worldwide maximum wind speed measured at a surface station is a 5-min speed of 91 m/s and a 1-s gust of 101 m/s measured at Mt. Washington, New Hampshire Observatory on 12 April 1934. Mt. Washington is 1915 m above mean sea level and the anemometer was mounted at 11.6 m.

Operationally speaking, the greatest wind extremes are typically in northern Scotland. In the windiest month the 1% extreme is set at 22 m/s (a 1-min wind at 3 m above ground level). Gusts accompanying this extreme are estimated, by the shortest dimension of equipment, at

Dimension (m)	Speed (m/s)
<0.6	32
1.5	30
3.0	29
7.6	27
15.2	26
30.5	25

17.4.5 Structure of Jet Streams

Belts of exceptionally strong winds are jet streams. (The term as commonly used applies to the strong westerly winds found at the base of the stratosphere.) Because the meteorological disturbances vary in size and intensity and are moving, the jet streams vary in extent, severity, and location. Geographically-oriented descriptions obscure significant features. As Figure 17-17 shows, this is overcome by relating the features to the position of the core. In winter, the centers (or cores) of jet streams are found at altitudes between 9 and 12 km in latitudes 25° to 70° in each hemisphere. In summer, jet streams are weaker, higher (11 to 14 km), and farther poleward (35° to 75° latitude). Generally speaking, a jet stream is several thousand kilometers long,

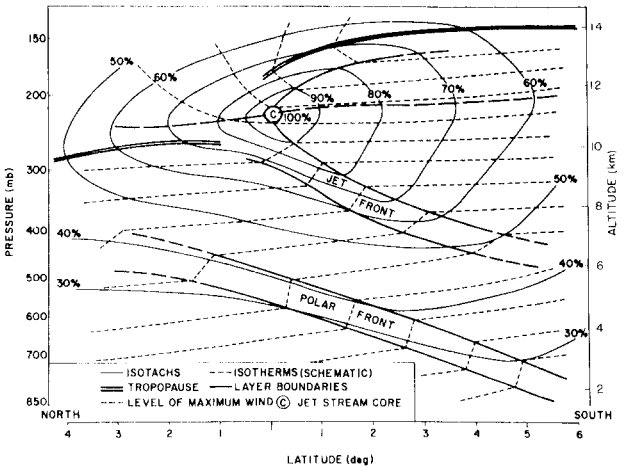

Figure 17-17. Idealized model of the jet stream, average structure in a cross section perpendicular to the flow. (Percent of the core speed is given for each isotach; wind direction is into the page.)

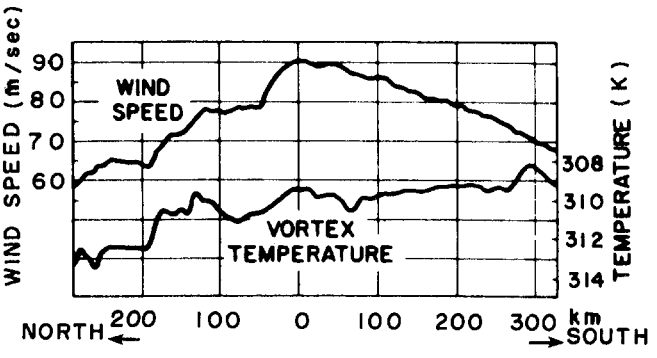

Figure 17-18. Example of wind and temperature fields near the jet stream.

several hundred kilometers wide, and several kilometers deep.

The typical structure of jet streams is shown in Figure 17-17; this is a cross section showing isotachs (lines of equal wind speed blowing "into the page") labeled in percent of the wind speed at the jet core. Core wind speeds range from 50 m/s to as much as 130 m/s on rare occasions. Speeds of 75 m/s are common in winter. Figure 17-17 also shows the thermal field, the tropopause, and the level of maximum wind. Typical wind and temperature variations across jet streams at a constant altitude or vertically through jet streams can be determined from this figure.

Individual jet streams are variable and may differ considerably from the typical. In some cases, two or even three jet cores may be found paralleling each other, separated by distances of several hundred km. In addition to these deviations from the average, eddies of various sizes are present in the wind and temperature fields, as shown in Figure 17-18. Extreme horizontal changes of wind and temperature are of the order of 20 m/s and 5 K in a 16-km distance measured perpendicular to the jet stream. Variations parallel to jet streams are an order of magnitude smaller.

Clear air turbulence is closely related to jet stream structure; measurements show that it is more likely in certain regions than in others [McLean, 1962]. At the level of maximum wind (where vertical shear changes sign), turbulence was observed about 14% of the time. From Figure 17-19 it can be seen that turbulence is most likely to be found north of the jet stream core near the polar tropopause and above the core along the tropical tropopause. Indication of a maximum is also found in the jet stream front.

Other wind currents which exhibit properties similar to those shown in Figure 17-17 are the low-level jet and the tropical easterly jet stream which is observed in certain areas (for example, southern India) at an altitude of about 14 km in summer.

Frequently it is too expensive to design equipment to operate under extreme conditions. In such cases, calculated risks are assumed or alternate methods of operation are devised for periods when such conditions exist. If high wind speeds or strong shears normally associated with them adversely affect the operation of a particular vehicle that is released vertically into the atmosphere, it may be desirable to select several release sites spaced far enough apart to ensure that operational conditions will exist above one of the stations when the critical wind speed or shear is exceeded above the others. In such cases, Figure 17-17 will be useful in selecting alternate sites; it indicates the average rate with which wind speed decreases with distance on both sides of the jet stream core. For example, with a 100 m/s wind at the jet stream core, Figure 17-17 indicates that, on the average, a belt of winds exceeding 70 m/s can be expected to extend more than 300 km south and nearly 200 km north of the core. Consequently, if the maximum wind likely to occur over a region is 100 m/s and the vehicle is only designed to withstand speeds up to 70 m/s alternate release

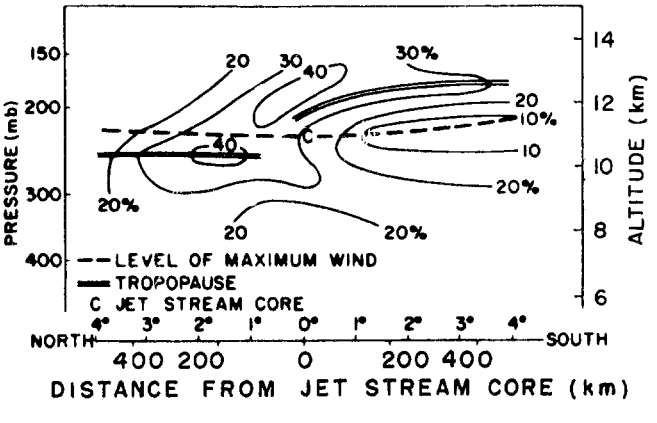

Figure 17-19. Turbulence in various sectors of a typical jet stream cross section. (Frequency (%) of occurrence is shown for each contour.)

sites should be selected at least 500 km apart. As the jet stream axis occasionally approaches a north-south orientation, selected sites should be more than 500 km apart in longitude as well as in latitude.

17.5 THERMOSPHERIC WINDS

Neutral air motions are a major key to our understanding of the upper atmosphere at thermospheric altitudes. A variety of phenomena associated with the neutral and ionized atmosphere need to be explained in terms of a unifying description of thermospheric dynamics. Neutral density, composition, and temperature characteristics are related to geomagnetic storm-induced circulation processes and seasonal and diurnal tides. Aspects of ionospheric structure depending directly on winds and compositional transport include maintenance of the nighttime ionosphere, spread F-layers, scintillations, and geomagnetic storm effects.

The dynamics of the upper atmosphere are controlled mainly by solar EUV and UV heating, waves and tides propagating upward from the mesosphere, ion drag interactions with the ionosphere, and energy and momentum sources associated with auroral region processes (magnetospheric convection and particle precipitation). The major heat source, due to solar electromagnetic radiation, is deposited mainly at low and midlatitudes and is reasonably well understood. At high latitudes, magnetospheric convection effects are important even during geomagnetically quiet times. They dominate the high latitude circulation during geomagnetic storms. Magnetospheric convection processes are extremely variable and are not well understood (see Chapter 8). The phenomenon involves ionospheric plasma driven into motion by electric fields interacting with the neutral atmosphere via collisions. The neutral constituents gain energy through Joule dissipation of currents and gain momentum through ion-neutral drag [Straus, 1978; Mayr et al., 1978].

Most of our present knowledge of thermospheric neutral winds is based on calculations made by using semiempirical dynamic models of the neutral atmosphere. The pressure gradients inherent in these density models provide the pressure forces that drive the thermospheric circulation. At thermospheric altitudes the collision frequency is sufficiently high that the air may be regarded as a fluid subject to hydrodynamic equations of motion. Therefore, the equations of fluid motion can be integrated to determine the wind system that should result from the pressure distribution. These equations are the same as those used by meteorologists to study the lower atmosphere, but are modified to include two additional terms that are important in the thermosphere: a viscous force and an ion drag force. Kinematic molecular viscosity transfers momentum between various altitude regions and thus smoothes out vertical gradients in wind velocity. It is inversely proportional to density and is large enough above 300 km to prevent development of large vertical and horizontal shears. Ion drag is a collisional interaction between charged particles and neutral particles. Outside the auroral zone, where electric fields are small, the ions above 120 km can be assumed to corotate with the earth. A neutral wind flowing through the ions experiences a collisional drag that is a maximum at the peak of the ionospheric layer. A global distribution of electron density [for example Ching and Chiu, 1973] is used to determine the ion drag in various model calculations.

The important terms in the equations of motion of the neutral air velocity U are

$$\frac{d\mathbf{U}}{dt} = \mathbf{F} - 2\,\boldsymbol{\Omega} \times \mathbf{U} - \nu_{ni}(\mathbf{U} - \mathbf{V}) + \frac{\mu}{\rho}\nabla^2\mathbf{U} + \mathbf{g}$$

(Acceleration) = (Pressure gradient force) − (Coriolis term) − (Ion Drag) + (Viscous Drag) + (Gravity)
where

$$\frac{d\mathbf{U}}{dt} = \frac{\partial \mathbf{U}}{\partial t} + (\mathbf{U} \cdot \nabla)\mathbf{U}$$

and **V** is the ion drift velocity, $\boldsymbol{\Omega}$ is earth's angular velocity, **F** is the driving force per unit mass due to pressure gradients determined from a model, ν_{ni} is the appropriate neutral-ion collision frequency, μ is the coefficient of kinematic viscosity, ρ is the atmospheric density, and **g** is the acceleration due to gravity. Since this equation contains the ion velocity and the collision frequency that is proportional to the ion concentration, it is necessary to take into consideration the equation of motion and continuity equation for the ions. Methods of solutions to this set of equations for thermospheric altitudes have been extensively described by Rishbeth [1972]. (Note that the definition of winds does not include the corotation of the atmosphere. Results in this chapter are presented in a coordinate system that rotates with the earth). The accuracy of all models of global winds systems is limited by lack of experimental data and self-consistent model solutions. Complete specification of the wind fields requires solving a large set of non-linear partial differential equations in three dimensions that relate the hydrodynamic and electrodynamic properties of the neutral and ionized components in the atmosphere to the energy, mass, and momentum sources of the magnetosphere-ionosphere-thermosphere system.

A brief review of thermospheric wind properties deduced from experimental data is given in Section 17.5.1. The remainder of this chapter describes winds data derived from various models, which are only briefly described here. References provided should be consulted for the theoretical aspects and for detailed descriptions of the results. Numerous plots excerpted from the relevant journal articles, summarize these data. The development over the past decade

of a general circulation model at the National Center for Atmospheric Research (NCAR) is traced historically. Variations in circulation as a function of season, solar cycle, altitude, and latitude are given in Section 17.5.2. Local time variations are shown in Section 17.5.3. Results of including the effects of magnetospheric convection are shown in Section 17.5.4. This section also includes the recent work, described in a series of papers, of the University College of London group in determining the influence of magnetospheric convection. At present, the effects of heating by particle precipitation at high latitudes and by upward propagating atmospheric tides and momentum deposition by tides at lower latitudes are not included in the above models. There are insufficient data on which to build an adequate model of particle precipitation. Tidal phenomena have been extensively described by Forbes and Garrett [1979] and by Forbes [1982a,b] and should eventually be incorporated as part of thermospheric dynamic models.

17.5.1 Observational Summary and Limitations

Direct measurements of winds in the thermosphere are difficult to make and there have been insufficient observations for development of empirical models. Techniques include ground-based Fabry-Perot spectrometer measurements of the 6300 Å line in the airglow [for example, Hays and Roble, 1971; Sipler et al., 1982] and incoherent scatter radar techniques [for example, Evans, 1975], rocketborne chemical release experiments [for example, Kelley et al., 1977], and satellite data from mass spectrometers [for example, Spencer et al., 1976] and accelerometers [DeVries, 1972; Marcos and Swift, 1982]. These limitations are being ameliorated at F region altitudes with Dynamics Explorer satellite data from the Fabry-Perot Interferometer [Hays et al., 1981] and Winds and Temperature Spectrometer [Spencer et al., 1981]. An extensive review of recent thermospheric wind measurements has been given by Roble [1983]. General features of wind patterns deduced from these experimental data in this reference are summarized below for different latitude regions. For more detailed information on various experimental techniques and results obtained, the reader should consult Roble [1983] and references therein.

The general circulation at midlatitudes at F region heights is controlled mainly by solar heating during quiet geomagnetic conditions and high latitude heat sources during storms. Experimental data obtained when geomagnetic activity is low indicate a flow from the high temperature dayside of the thermosphere to the low temperature nightside. Daytime poleward meridional winds are 50–100 m/s and nighttime equatorward winds are about 100–200 m/s. These values depend on ion drag and season. Zonal winds are generally found to be westward before local noon and eastward in the afternoon. A nighttime transition occurs in early morning (winter) or near midnight (summer). During geomagnetic storms, data show the influence of high latitude heat sources. Observed effects include enhanced nighttime winds, earlier nighttime transition of zonal winds from eastward to westward, a tendency for a midnight "surge" of winds, and occasionally enhanced poleward daytime winds. Fabry-Perot data at Fritz Peak, Colorado, showed nighttime peak equatorial winds of 650 m/s were linearly related to the time rate of change of the equatorial ring current, and peak equatorial meridional and westward zonal winds were related to the square of the auroral electrojet index.

At near-equatorial latitudes the circulation is primarily controlled by solar heating, upward-propagating tides from below 100 km, large-scale neutral gas-plasma interactions (such as $\mathbf{E} \times \mathbf{B}$ drifts), and effects related to geomagnetic storms. A unique feature in this region is the equatorial midnight temperature bulge discovered in incoherent scatter and satellite data. This persistent but variable feature has been attributed to a complex interaction between the upward-propagating semidiurnal tide and ion-neutral momentum coupling associated with the diurnal variation of ion density. A general trend observed is that nighttime equatorward winds weaken and sometimes reverse after midnight in response to this bulge. Other features of the low latitude circulation include seasonal variations with stronger equatorward winds in summer than in winter, and zonal winds that are eastward throughout the night during winter and spring but have a westward reversal during early morning hours in the summer.

At high latitudes, F region data indicate magnetospheric convection is the dominant factor controlling wind systems. Fabry-Perot measurements [Hays et al., 1979] show early evening westward winds in the direction of magnetospheric convection and give evidence of a heat source located near local midnight. Heppner and Miller [1982], analyzing 39 chemical-release rocket experiments at high latitudes, found that winds in the magnetic dusk sector above 160 km follow the magnetospheric convection pattern with a time lag of about two hours. They also observed a 140–160 km altitude transition region in the wind pattern. Meriwether et al. [1982] used airglow data to show strong magnetospheric convection-driven winds with superimposed variability probably due to particle precipitation. Dynamics Explorer (DE) satellite data analyzed by Killeen et al. [1982] show wind velocities of 600–800 m/s. They further show that the DE data can be described as a superposition of a "background" solar-driven wind field and a wind field driven by high latitude energy and momentum sources. DE data of Spencer et al. [1982] showed zonal winds of about 1 km/s related to convecting ions. These strong zonal winds frequently correlated with vertical motions having velocities of 100–250 m/s. Knutson et al. [1977] also found evidence of large vertical winds, up to 65 m/s, in the early morning sector of the auroral zone, with no simple correlation with Kp.

17.5.2 Diurnally Averaged Winds

17.5.2.1 Seasonal Variations at Solar Maximum. The zonal mean (diurnally averaged) thermospheric circulation has been calculated for solar maximum equinox and solstice conditions respectively by Dickinson et al. [1975, 1977] using a two-dimensional (time-dependent) model run under steady state conditions. Their model utilized a zonally averaged version of lower atmospheric dynamic meteorology equations. Heat and momentum sources used were solar EUV and UV heating, high latitude heating due to auroral processes (assumed distributed uniformly in longitude) and a momentum source resulting from correlation of the diurnal variation of winds and ion drag. This model uses a 5° latitude-by-longitude grid with 24 constant-pressure surface layers extending in altitude from about 100 to 500 km. (Note that the altitude of a constant pressure surface can vary.) Their results showed that while the winds are driven primarily by heating due to solar EUV and UV absorption, a high latitude heat source was also required to give an equatorward mean meridional circulation in agreement with incoherent scatter observations [Evans, 1972]. Equinoctial circulation properties are schematically represented in Figure 17-20. This figure shows the mass flow of the cellular motion above about 80 km. Figure 17-20a shows the circulation during a very quiet geomagnetic period. Upward motion occurs over the equatorial subsolar point and flows poleward to high latitudes where sinking motion occurs. The small reverse circulation at high latitudes is due to a small high-latitude heat source as well as persistent solar heating over the polar regions. During average geomagnetic activity (Figure 17-20b) the equatorward circulation is larger. Below ~150 km the strong solar UV heating still maintains a poleward flow. At higher altitudes the flow is equatorward to about 20° latitude. During large geomagnetic storms (Figure 17-20c) the equatorward circulation extends to the equator and circulation below 150 km is also modified. The situation is similar during solstice. Under geomagnetically quiet conditions (Figure 17-21a) the asymmetry in solar heating drives a summer-to-winter circulation. For average geomagnetic conditions (Figure 17-21b), the high-latitude heat source reinforces the summer-to-winter circulation in the summer hemisphere but forces a reverse circulation in the high latitude winter hemisphere, with transition from

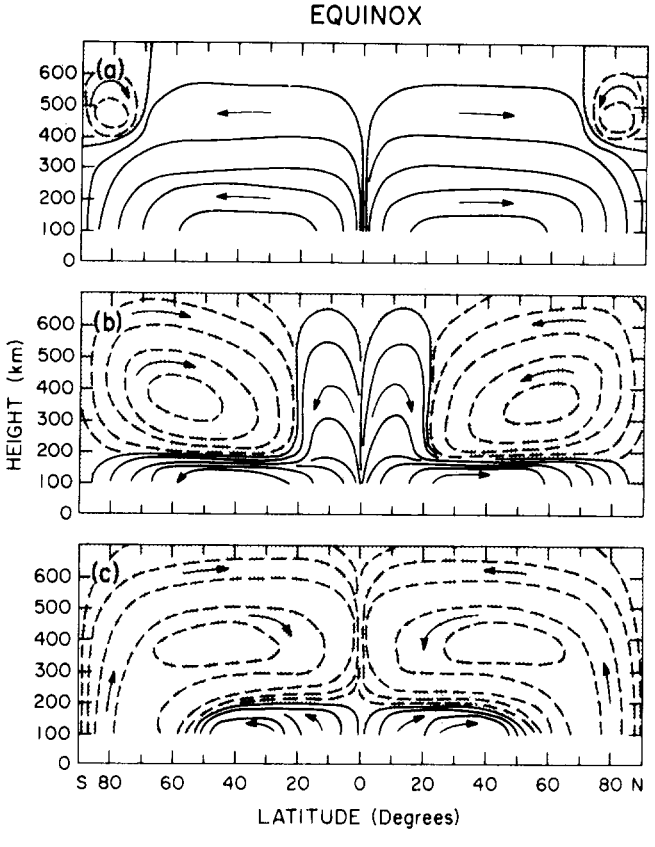

Figure 17-20. Schematic diagram of the zonal mean meridional circulation in the earth's thermosphere during equinox for various levels of auroral activity (a) extremely quiet geomagnetic activity, (b) average activity (10^{18} erg/s), and (c) geomagnetic substorm (10^{19} erg/s). The contours schematically illustrate the mass flow, and the arrows indicate the direction of the motion [Roble, 1977].

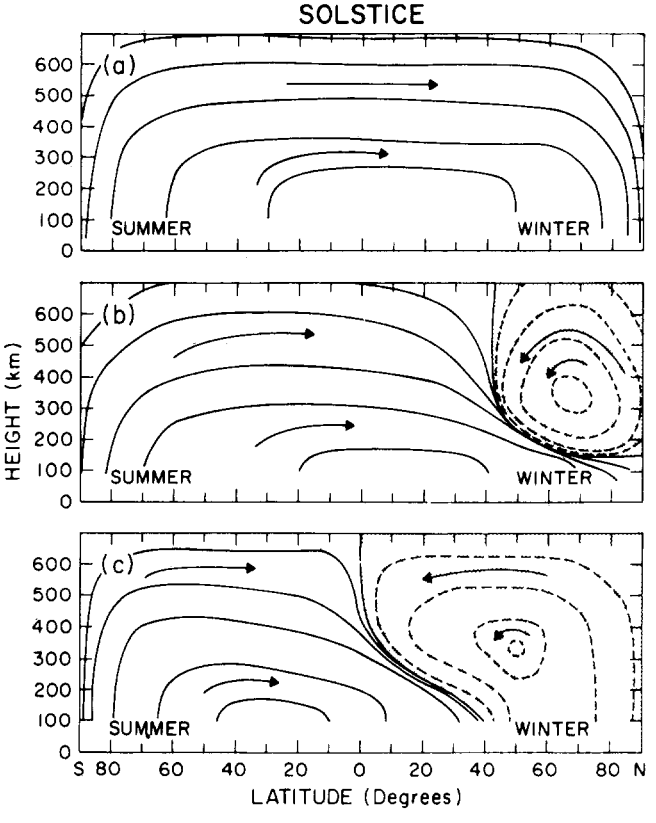

Figure 17-21. Schematic diagram of the zonal mean meridional circulation in the earth's thermosphere during solstice for various levels of auroral activity (a) extremely quiet geomagnetic activity, (b) average activity (10^{18} erg/s), and (c) geomagnetic sugstorm (10^{19} erg/s). The contours schematically illustrate the mass flow, and the arrows indicate the direction of the motion [Roble, 1977].

one cell to another in the midlatitude winter hemisphere. Below ~150 km the summer-to-winter circulation is maintained at all latitudes. During large geomagnetic storms (Figure 17-21c) the circulation is equatorward above 300 km in both hemispheres, with an asymmetry at lower altitudes.

Roble et al. [1977] have extended this analysis to determine seasonal circulation patterns for solar maximum (F = 165 units) and solar minimum conditions (F = 80 units). A solstice-type circulation is maintained except for about a week either side of equinox. This circulation is most intense at solstice and weakens as equinox is approached. The transition period is controlled in part by the high-latitude heat source which in turn is related to geomagnetic activity. For higher geomagnetic activity the transition from equinox to solstice circulation occurs more rapidly. The derived diurnally average meridional, zonal, and vertical winds for solar maximum conditions are shown in Figures 17-22–17-24 respectively. These results correspond to average geomagnetic conditions.

During equinox the meridional flow (Figure 17-22a) below 150 km is directed from the equator to both poles at about 5 m/s. At higher altitudes the pole-to-equator flow has a maximum velocity of about 50 m/s near 60° latitude in both hemispheres. By October 6 (Figure 17-22b) the circulation below 150 km is almost completely reversed in the summer hemisphere. The summer-to-winter circulation intensifies from 50 to 200 m/s as the season progresses toward the solstice conditions of Figure 17-22c and d. Above ~200 km an intensification of the summer hemisphere equatorward circulation penetrates into the winter hemisphere and forces the boundary between the two oppositely directed winds poleward as the season progresses toward solstice. This boundary is near the equator at equinox and at ~60° latitude for solstice. Also, the strongest equatorward winds in the high latitude winter hemisphere decrease from about 50 m/s at equinox to about 30 m/s at solstice.

The derived zonal winds during equinox (Figure 17-23a) are relatively weak above 200 km. As the season progresses (Figure 17-23b and c) there is a gradual increase in wind speeds above ~150 km in the summer hemisphere and below 150 km in the winter hemisphere. At solstice (Figure 17-23c) there are generally westward winds in the summer hemisphere and eastward winds in the winter hemisphere. In the winter hemisphere the velocity at ~120 km increases to 120 m/s. Above 200 km the maximum solstitial velocities increase to 60 m/s in the summer hemisphere and 40 m/s in the winter hemisphere.

Vertical velocities shown in Figure 17-24 are given in units of cm/s. Below ~120 km the vertical velocity at equinox (Figure 17-24a) is upward in the equatorial region and downward at middle and high latitudes. By October 6 (Fig-

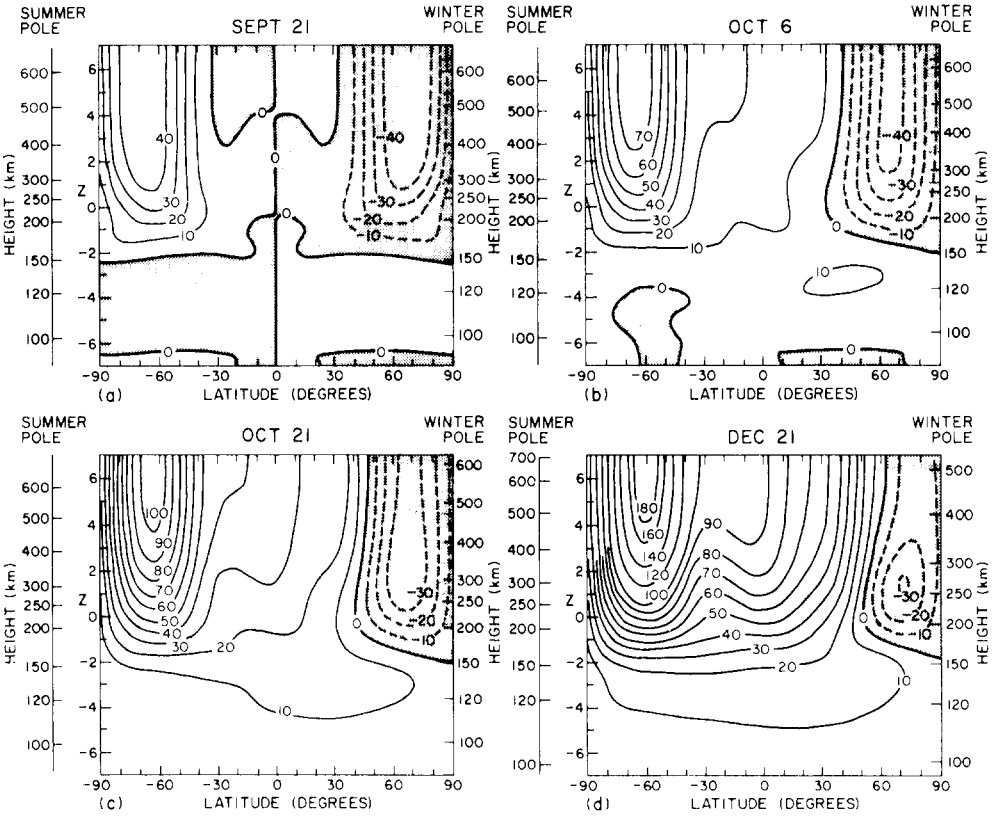

Figure 17-22. The calculated zonal mean contours of meridional wind component (in m/s) for 4 days representing the seasonal variation during solar maximum (a) equinox, September 21, (b) October 6, (c) October 21, and (d) winter solstice, December 21 [Roble et al. 1977].

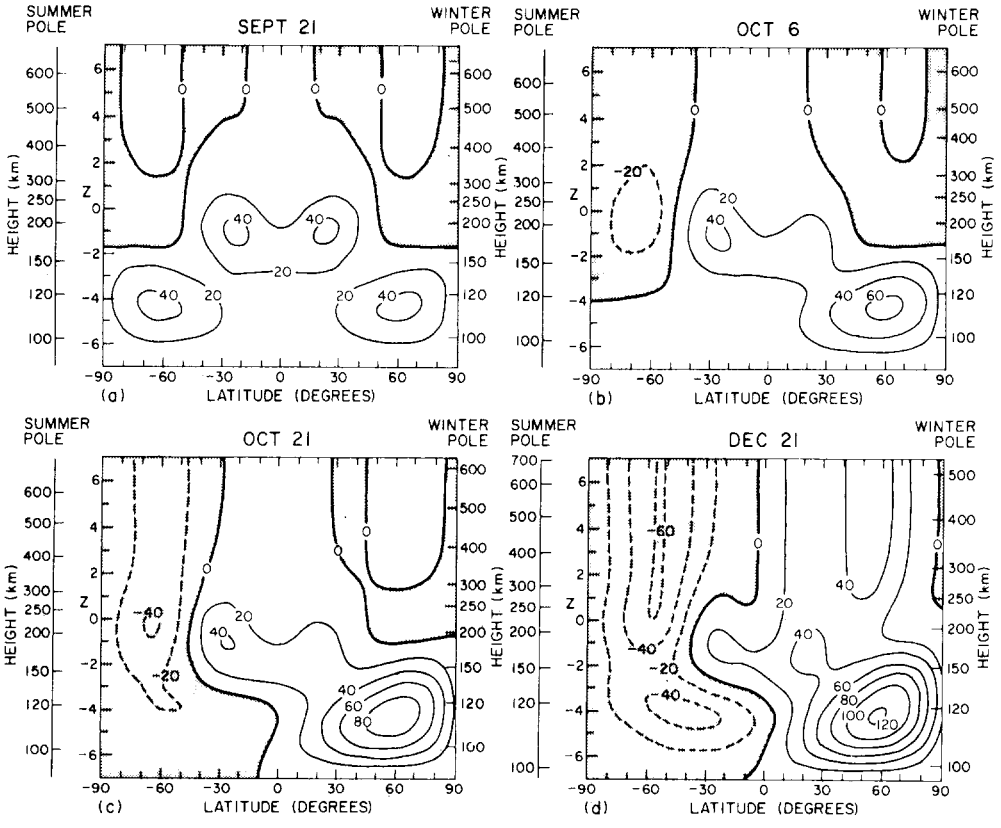

Figure 17-23. The calculated zonal mean contours of zonal wind component (in m/s) for 4 days representing the seasonal variation during solar maximum (a) equinox, September 21, (b) October 6, (c) October 21, and (d) winter solstice, December 21 [Roble et al, 1977].

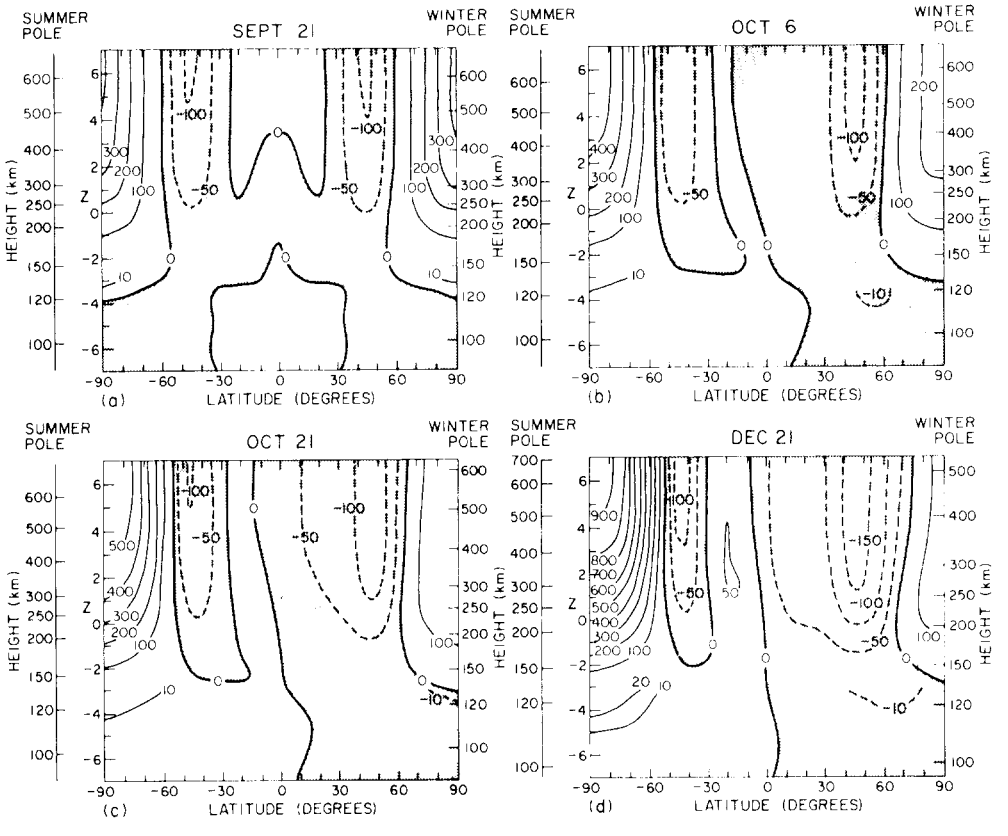

Figure 17-24. The calculated zonal mean contours of vertical wind component (in cm/s) for 4 days representing the seasonal variation during solar maximum (a) equinox, September 21, (b) October 6, (c) October 21, and (d) winter solstice, December 21 [Roble et al, 1977].

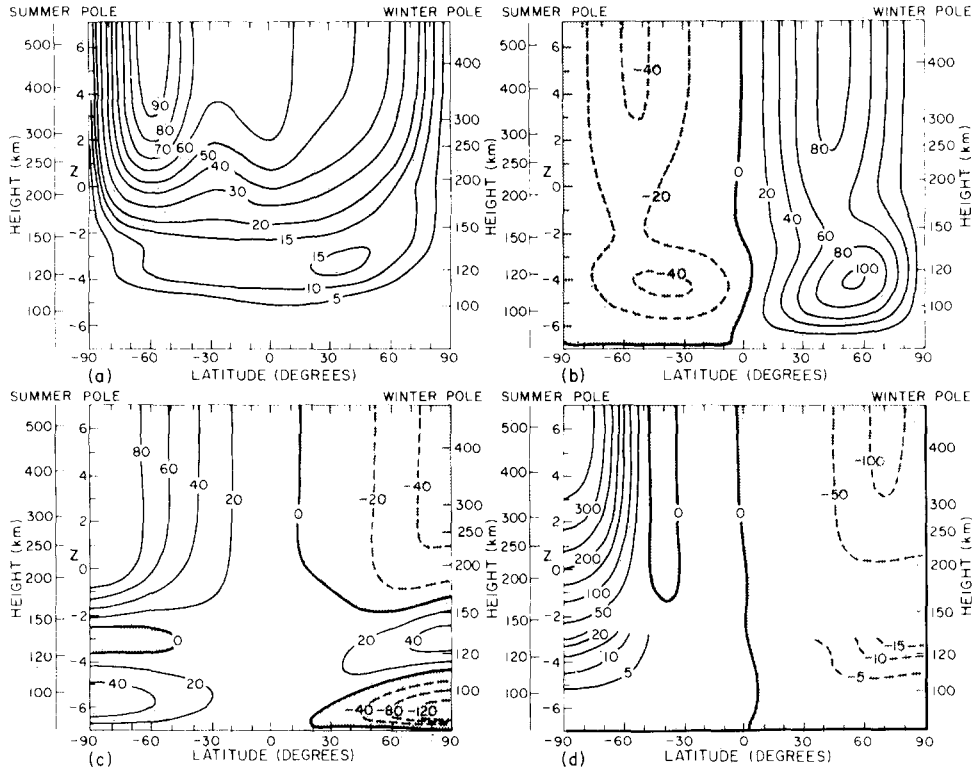

Figure 17-25. Calculated contours of the perturbation zonal mean temperature and winds for December solstice during solar minimum: (a) meridional winds (in m/s), (b) zonal winds (in m/s), (c) temperature (in K) and (d) vertical winds (in cm/s) [Roble et al, 1977].

ure 17-24b) these motions become upward in the summer hemisphere and downward in the winter hemisphere. This pattern intensifies as solstice is approached (Figure 17-24c and d). Maximum upward velocities occur at high latitudes and maximum downward velocities occur at mid-latitudes. The main seasonal effect above ~200 km is the increasing asymmetry between hemispheres as the season progresses. At high latitudes the summer hemisphere upward velocities are about six times greater than those in the winter hemisphere.

17.5.2.2 Solstice Variations at Solar Minimum. Results of calculations for solar minimum (F = 80) December solstice conditions are presented as Figures 17-25a–d for the meridional wind, zonal wind, perturbation temperature, and vertical wind, respectively. The high latitude heat source required to obtain reasonable agreement between the model and experimental data was 4.4 times smaller than that required for solar maximum conditions.

The meridional winds (Figure 17-25a) are directed from the summer to winter hemisphere at all altitudes and latitudes. A maximum velocity of 90 m/s occurs near 330 km at 60° latitude in the summer hemisphere. The magnitude of the winds in the summer hemisphere are lower than those at solar maximum by about a factor of two. The derived high latitude heat source in the winter hemisphere is not sufficiently large to drive a reverse circulation. Poleward winds are encountered at all latitudes in the winter hemisphere. The zonal winds (Figure 17-25b) are westward in the summer hemisphere and eastward in the winter hemisphere. These winds are similar in magnitude to those of solar cycle maximum. In general, the zonal jets near 120 km are slightly greater during solar maximum than during solar minimum. At higher altitudes the converse is true. Perturbation temperature data are shown in Figure 17-25c but are not discussed here. Vertical velocity results are shown in Figure 17-25d. In the summer hemisphere the winds are generally directed upward except for a small region of downward velocities near 40° above ~175 km. Downward winds occur at all latitudes in the winter hemisphere. Vertical velocities are smaller during solar minimum than during solar maximum.

17.5.3 Local Time Variations

A time-dependent "Three-dimensional General Circulation Model" (TGCM) developed by Dickinson et al. [1981] permits specification of winds in latitude-local time coordinates. This model uses the same geophysical inputs as in Dickinson et al. [1975, 1977] and Roble et al. [1977]. Results are presented in Figures 17-26 and 17-27 for solar

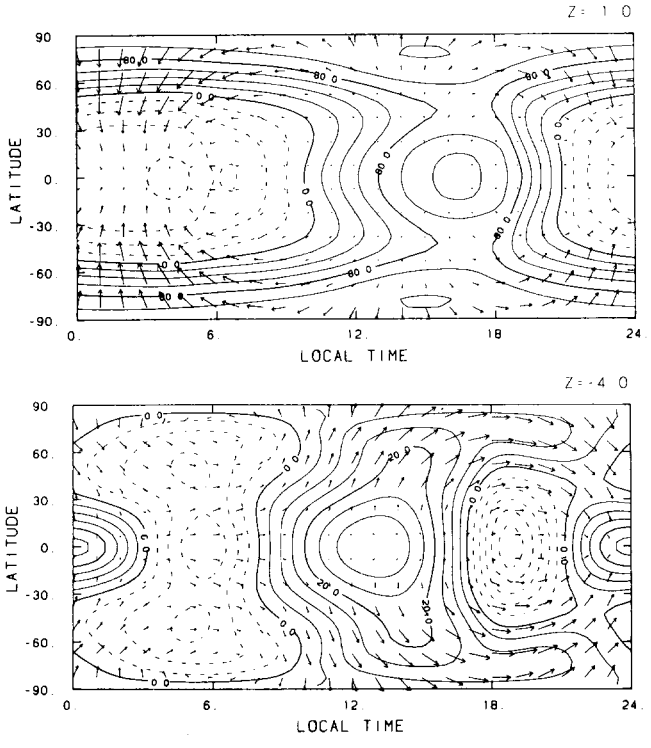

Figure 17-26. Calculated global distribution of winds and perturbation temperature (K) along two constant pressure surfaces: (a) z = 1 at approximately 300 km and (b) z = −4 at approximately 120 km for equinox conditions during solar cycle maximum. Both solar heating and a high-latitude heat source are included. The maximum wind arrow is 130 m/s in (a) and 90 m/s in (b). [Dickinson et al., 1981].

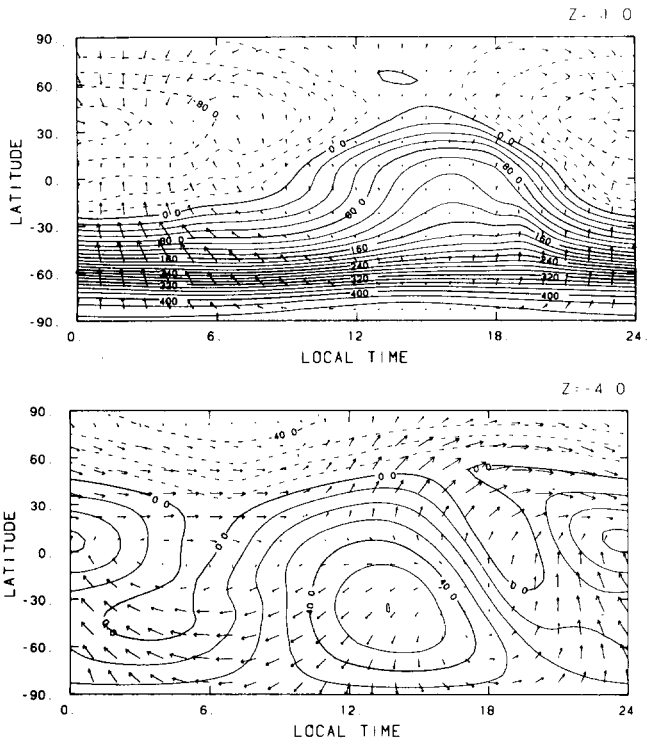

Figure 17-27. Calculated global distribution of winds and perturbation temperature (K) along two constant pressure surfaces: (a) z = 1 at approximately 300 km and (b) z = −4 at approximately 120 km for solstice conditions during solar cycle maximum. Both solar heating and a high-latitude heat source are included. The maximum wind arrow is 180 m/s in (a) and 75 m/s in (b) [Dickinson et al., 1981].

maximum equinox and solstice conditions, respectively, at altitudes of 120 km and 300 km. Solid lines shown in these figures represent a calculated perturbation temperature from global mean values derived from the model and are fully described in Dickinson et al. [1981]. The present discussion considers only the wind results, depicted by arrows.

At 300 km the equinoctial winds blow from the daytime high pressure region near 1700 LT into the nighttime low pressure region near 0400 LT as shown in Figure 17-26a. Maximum winds of 130 m/s occur at night when ion drag is smallest. At 120 km (Figure 17-26b) the maximum arrow corresponds to 90 m/s. The low latitude dynamic structure exhibits a semi-diurnal variation. At high latitudes the circulation remains nearly diurnal.

Results for solstice (southern hemisphere summer) at 300 km are shown in Figure 17-27a. High latitude heating greatly enhances the flow toward the winter hemisphere. The maximum wind vector is in the nighttime summer hemisphere with an equatorward velocity of 180 m/s. At 120 km (Figure 17-27b) the complex circulation pattern again shows a pronounced semi-diurnal oscillation at low latitudes and a dominent diurnal variation at high latitudes. The maximum velocity of 90 m/s occurs for high latitude night conditions.

17.5.4 Magnetospheric Convection Effects on Neutral Winds

More detailed and higher resolution models of thermospheric dynamics have resulted from incorporating electric field models to provide both an energy and momentum source at high latitudes. This permits including the important influence of high-latitude plasma convection. The magnitude of the magnetospheric convection is defined by the electric potential drop across earth's polar cap. Values to 150 kV are possible during strong geomagnetic storms. Correlation of polar cap convection potential drop with more conventional indicators of geomagnetic activity including the Kp and AE (auroral electrojet) indices has been studied by Reiff et al. [1981]. They found that AE had a correlation coefficient of 0.71 with the electric field data while Kp had a relatively weak correlation coefficient of 0.55.

Roble et al. [1982] have used the electric field model of Volland [1975, 1979a,b] in their Thermospheric General Circulation Model. Results have been initially presented to compare two cases: (1) solar EUV and UV heating only and (2) solar heating plus a 20 kV cross-tail potential to simulate low geomagnetic conditions. These runs assume equinox

and solar cycle maximum conditions and coincident geographic and geomagnetic poles. Circulation and temperature data are shown on polar plots for 50°N to 90°N geographic latitude. As in Figures 17-26 and 17-27, arrows represent wind magnitude and direction, and heavy solid lines represent perturbation temperatures.

Figures 17-28 a and b show the circulation pattern predicted at 130 km and 300 km, respectively, in response to solar heating only. These results are the same as obtained for Figures 17-26 and 17-27, but in polar plot format. The characteristic dayside to nightside flow is found at the 130 km level (Figure 17-28a). At high latitudes the daily variation pattern is mainly diurnal while a semidiurnal component is indicated at low latitudes. A counter-clockwise circulation is centered near 0600 LT and 75°N latitude. Maximum winds of 75 m/s occur in the polar region. At the 300 km level (Figure 17-28b) the strongest winds are again in the polar region. However, the day-to-night flow is now rotated to the left of that for the 130 km case.

The effect of including a 20 kV cross-tail potential is shown in Figure 17-29. In the lower thermosphere (Figure 17-29a) the dawn-dusk temperature contrast is enhanced in the polar region but the winds are only slightly changed (from a maximum of 75 m/s to 80 m/s). However, in the upper thermosphere (Figure 17-29b) the overall temperature contours are not significantly modified, but the polar region winds are greatly affected in magnitude and direction. Maximum winds increase from 120 m/s to 200 m/s over the poles. Also, the pattern of circulation in the polar cap is in the direction of the plasma drift associated with magnetospheric convection. At lower latitudes the influence of magnetospheric convection is much smaller.

The TGCM [Roble et al., 1982] was then modified to include displaced geographic and geomagnetic poles. Data are given below for a 20 kV and 60 kV (moderate geomagnetic activity) case. Figure 17-30 shows circulation patterns for the 20 kV case at 130 km and 300 km for 0600 UT and 1800 UT. At 130 km (Figures 17-30a and b) the counter-clockwise circulation on the morningside is near 80° latitude and 0° longitude at 0600 UT. Figure 17-30b (1800 UT) shows it has a UT dependence due to the displaced poles. The 300 km circulation patterns are shown in Figures 17-30c and d. These are analyzed as zonal and meridional components in Figure 17-31. Maximum zonal winds (Figures 17-31a and b) are about 200 m/s in the polar region at 1800 UT and are about 150 m/s at 0600 UT. Maximum meridional winds (Figures 17-31c and d) at high latitudes are also generally about 50 m/s greater at 1800 UT than at 0600 UT. Model results obtained by increasing the cross-tail potential to 60 kV (moderate geomagnetic activity) are shown in Figure 17-32. At 120 km (Figures 17-32a and b) the maximum wind velocity increases to 102 m/s. The counterclockwise wind rotation around the low temperature vortex also increases in magnitude. At 300 km (Figures

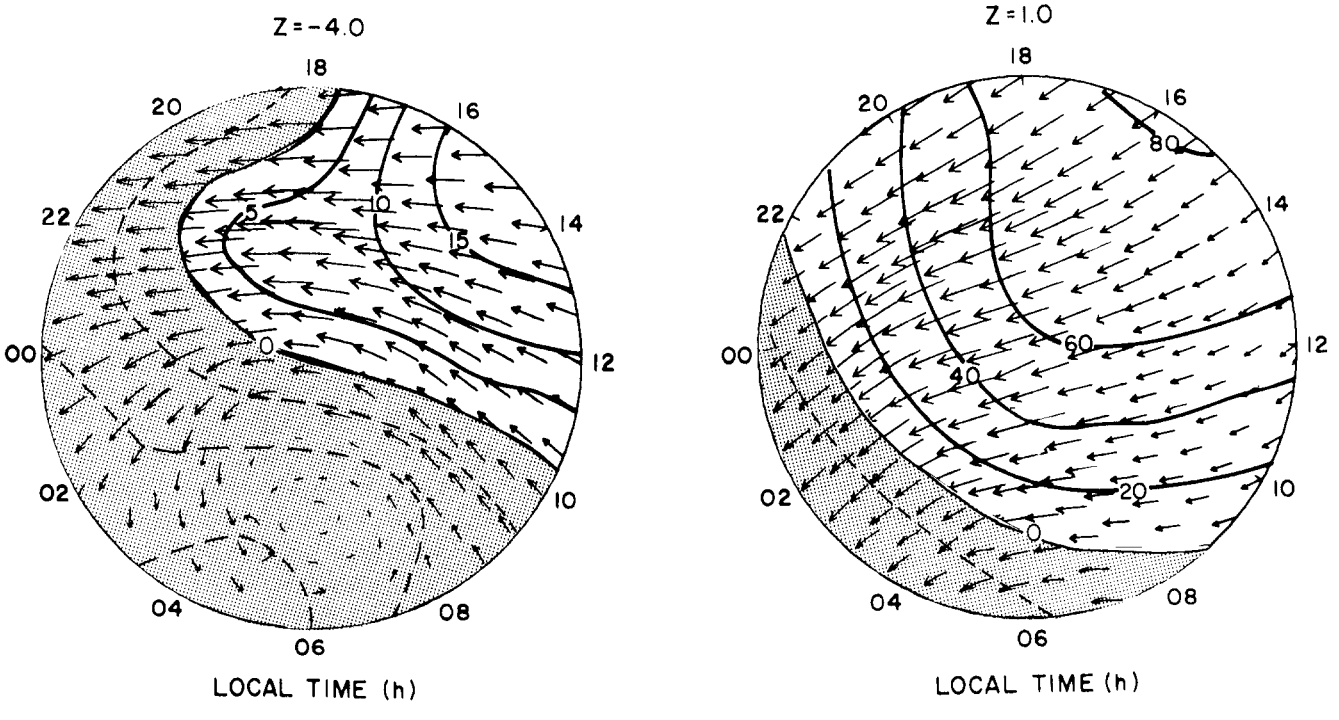

Figure 17-28. Polar plots giving the direction and magnitude of the calculated northern hemisphere high-latitude circulation and contours of perturbation temperature (K) along (a) the z = −4 (130 km) and (b) z = +1 (300 km) constant-pressure surfaces for the case of solar heating alone. Coincident poles are assumed. The wind speed associated with the maximum arrow is 75 m/s in (a) and 150 m/s in (b) [Roble et al., 1982].

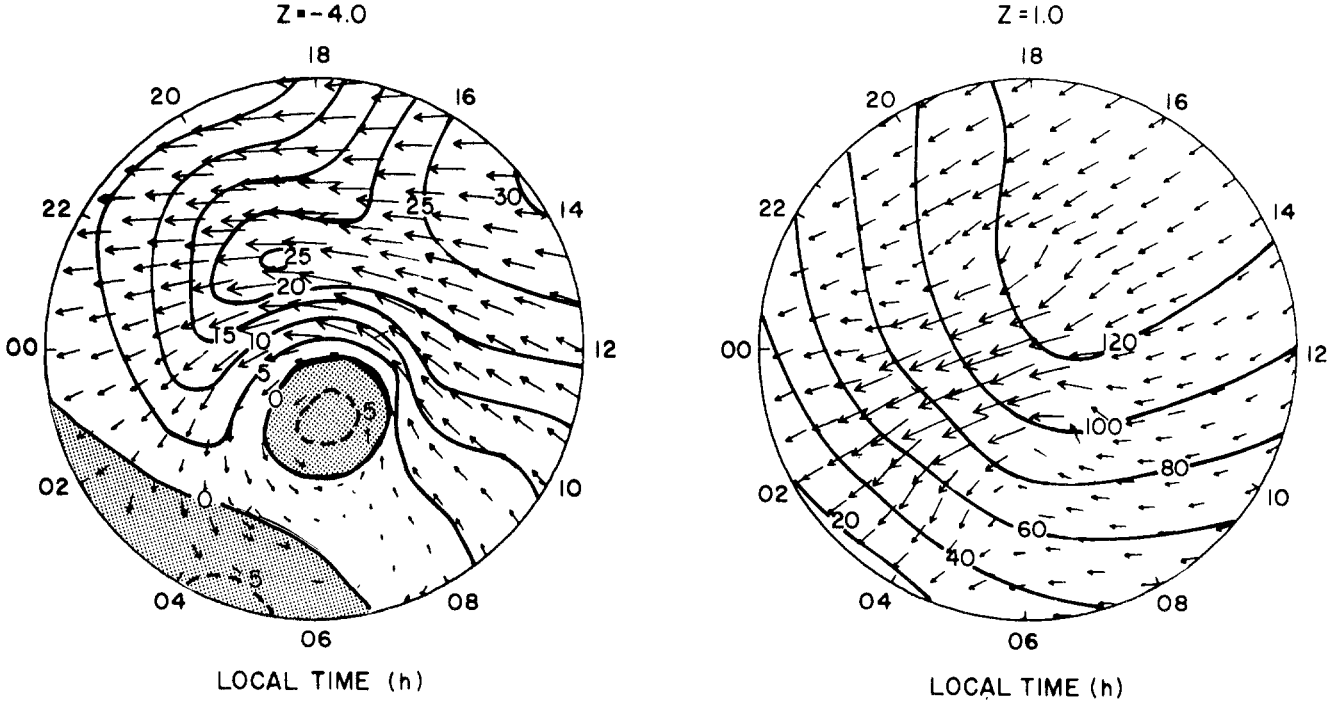

Figure 17-29. Polar plots giving the direction and magnitude of the calculated northern hemisphere high-latitude circulation and contours of perturbation temperature (K) including magnetospheric convection with a cross-tail potential of 20 kV along (a) the z = −4 (130 km) and (b) z = +1 (300 km) constant-pressure surfaces for the case of solar heating alone. The wind speed associated with the maximum arrow is 80 m/s in (a) and 225 ms^{0} in (b) [Roble et al., 1982].

17-32c and d) the winds in the magnetic polar cap increase to 380 m/s. These winds are enhanced by ion drag with the incremental winds tending to follow the twin ion drift vortices associated with magnetospheric convection. The double vortex wind system at F-region heights extends downward into the lower thermosphere. However, there is a significant shift in the pattern with the main features at 120 km associated with the cold low-pressure and warm high-pressure regions.

Roble et al. [1983] have extended the TGCM to examine seasonal variations for solar cycle maximum conditions. This version of the model assumes coincident geographic and geomagnetic poles; universal time effects are not included. Results are shown for the three cases: (1) solar EUV and UV heating only, (2) solar heating plus a 20 kV cross-tail potential, and (3) solar heating plus a 60 kV cross-tail potential.

Results for southern hemisphere summer at the altitude of approximately 130 km are given in Figure 17-33. With solar heating only (Figure 17-33a) the circulation is again from the high temperature noon sector toward the midnight sector where maximum wind velocities of about 75 m/s occur. With a 20 kV cross-tail potential (Figure 17-33b) there is very little change in the circulation pattern. The maximum wind speed is 77 m/s. For the 60 kV case (Figure 17-33c) the circulation pattern changes, reflecting the influence of the larger magnetospheric convection ion velocities. The maximum wind speed of 89 m/s occurs directly over the polar region. Vortex development occurs on the morningside of the polar cap, obstructing the seasonal flow from the high-to-low temperature regions. The effect of magnetospheric convection is to redirect the overall flow pattern, resulting in a jet over the polar cap.

Results for winter conditions in the northern hemisphere at 120 km are given in Figure 17-34. In each case, a counterclockwise circulation is driven throughout the high latitude region by a low-pressure system over the pole. Maximum wind speeds increase from 108 m/s to 117 m/s to 120 m/s as the cross-tail potential increases from zero kV to 20 kV to 60 kV. Magnetospheric convection effects are less than in summer because of the lower electron density and consequently decreased ion drag momentum source.

Results for the altitude of approximately 300 km for southern hemisphere summer winds are given in Figure 17-35. Maximum winds increase from 110 m/s for the zero kV case (Figure 17-35a) to 200 m/s for the 20 kV case (Figure 17-35b). For both cases the neutral winds tend to follow the two-cell pattern. For the 60 kV case (Figure 17-35c) anti-sunward winds increase to 380 m/s. Further, at the boundary of the polar cap, the wind direction is sunward, following the pattern of magnetospheric convection. An equatorward surge in wind velocities is also observed near local midnight.

Circulation patterns for the 300 km winter case are given

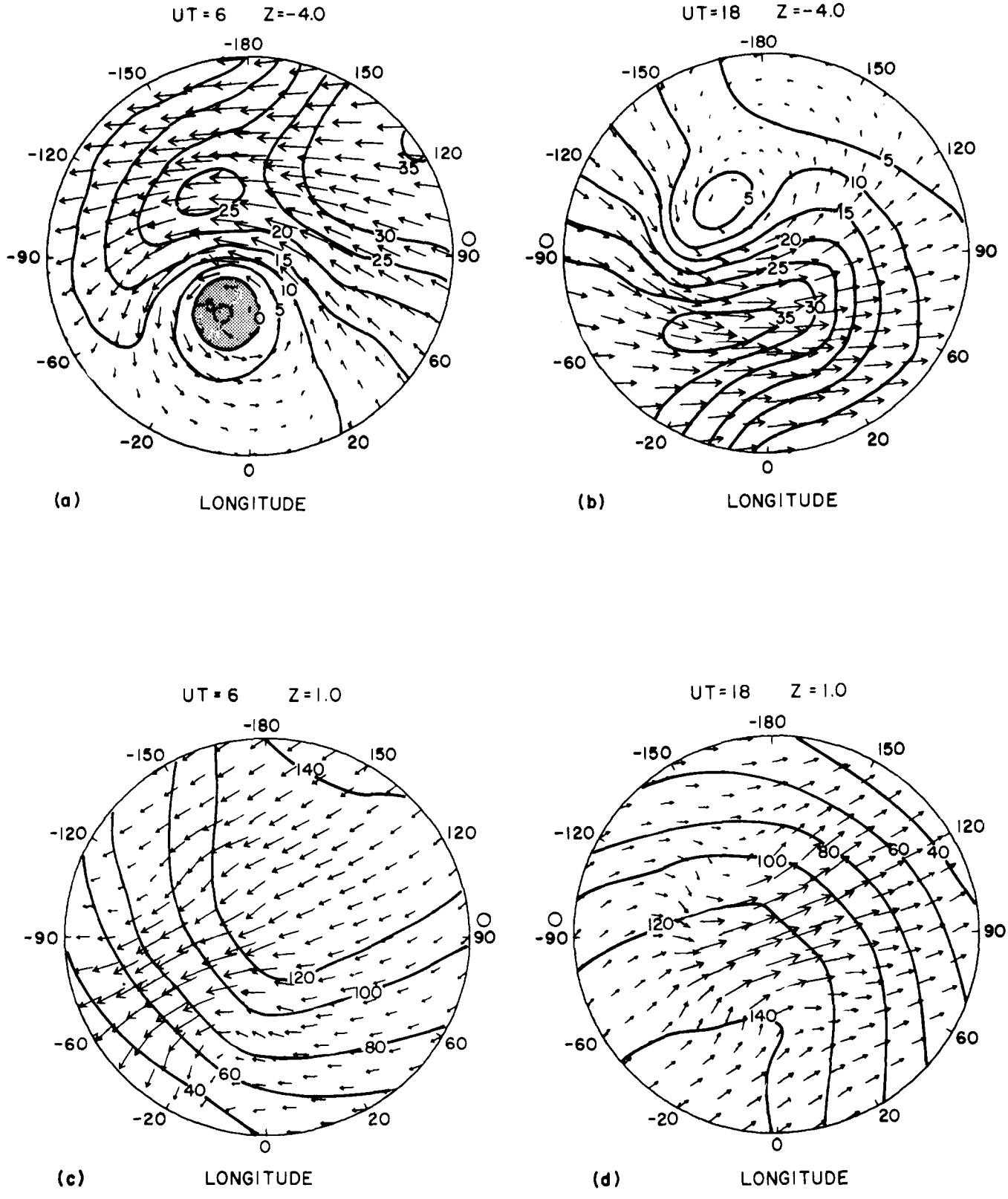

Figure 17-30. Winds and contours of perturbation temperature (K) along the z = −4 (130 km) surface for two universal times, 0600 UT (a) and 1800 UT (b), and along the z = +1 (300 km) surface at 0600 UT (c) and 1800 UT (d) for the case where the geographic and geomagnetic poles are displaced and the cross-tail potential for the magnetospheric convection model is 20 kV. The circulation is indicated by the arrows giving direction, and the length is the magnitude of the winds. The length of the maximum arrow represents 76 m/s in (a), 87 m/s in (b), 219 m/s in (c), and 222 m/s in (d), respectively. Local noon is inuicated by an open circle on the boundary [Roble et al., 1982].

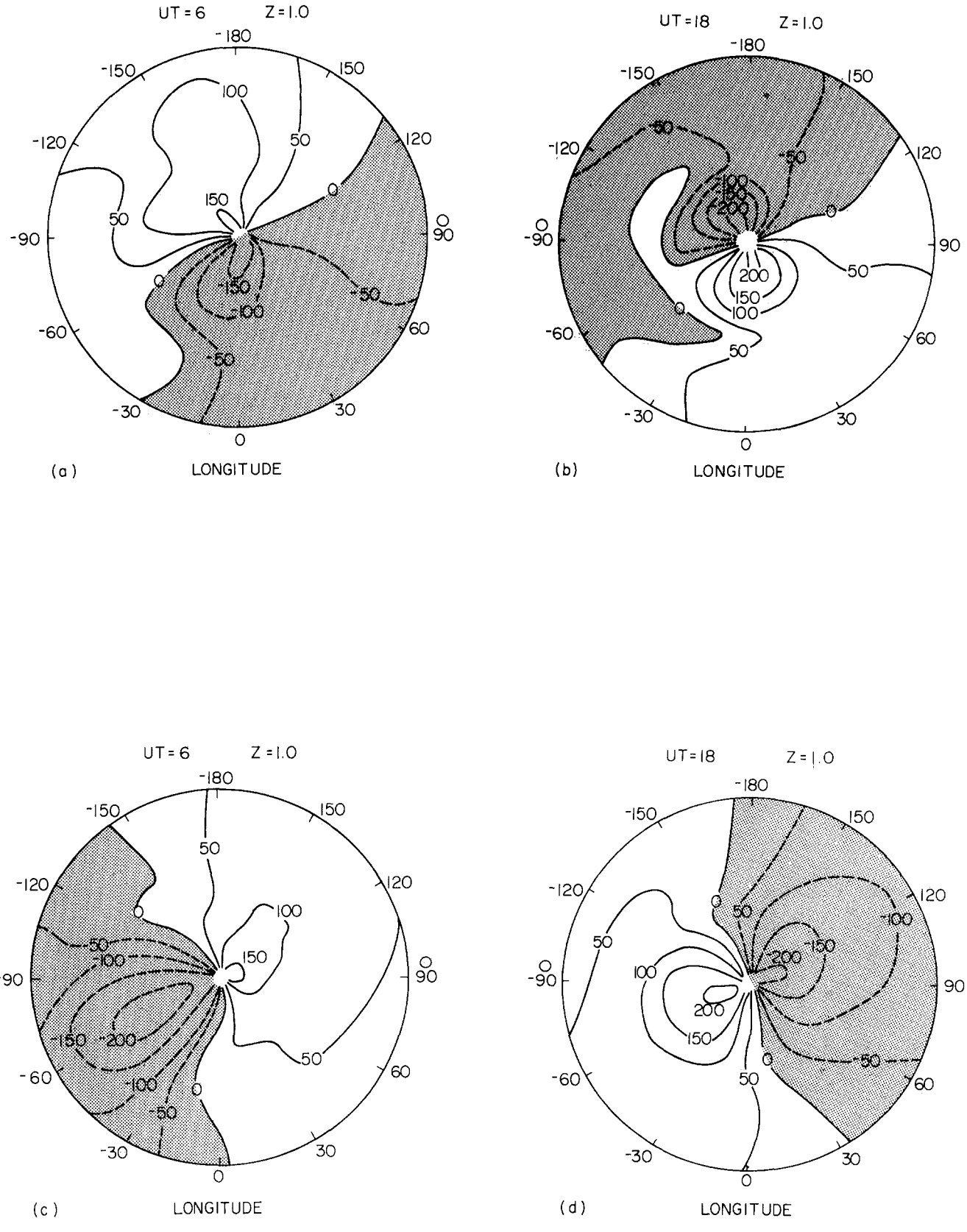

Figure 17-31. Contours of the zonal and meridional wind components at 0600 UT, (a) and (c), and 1800 UT, (b) and (d), respectively, along the z = +1 (300 km) surface for the case where the poles are displaced and the cross-tail potential is 20 kV. Local noon is indicated by an open circle on the boundary [Roble et al., 1982].

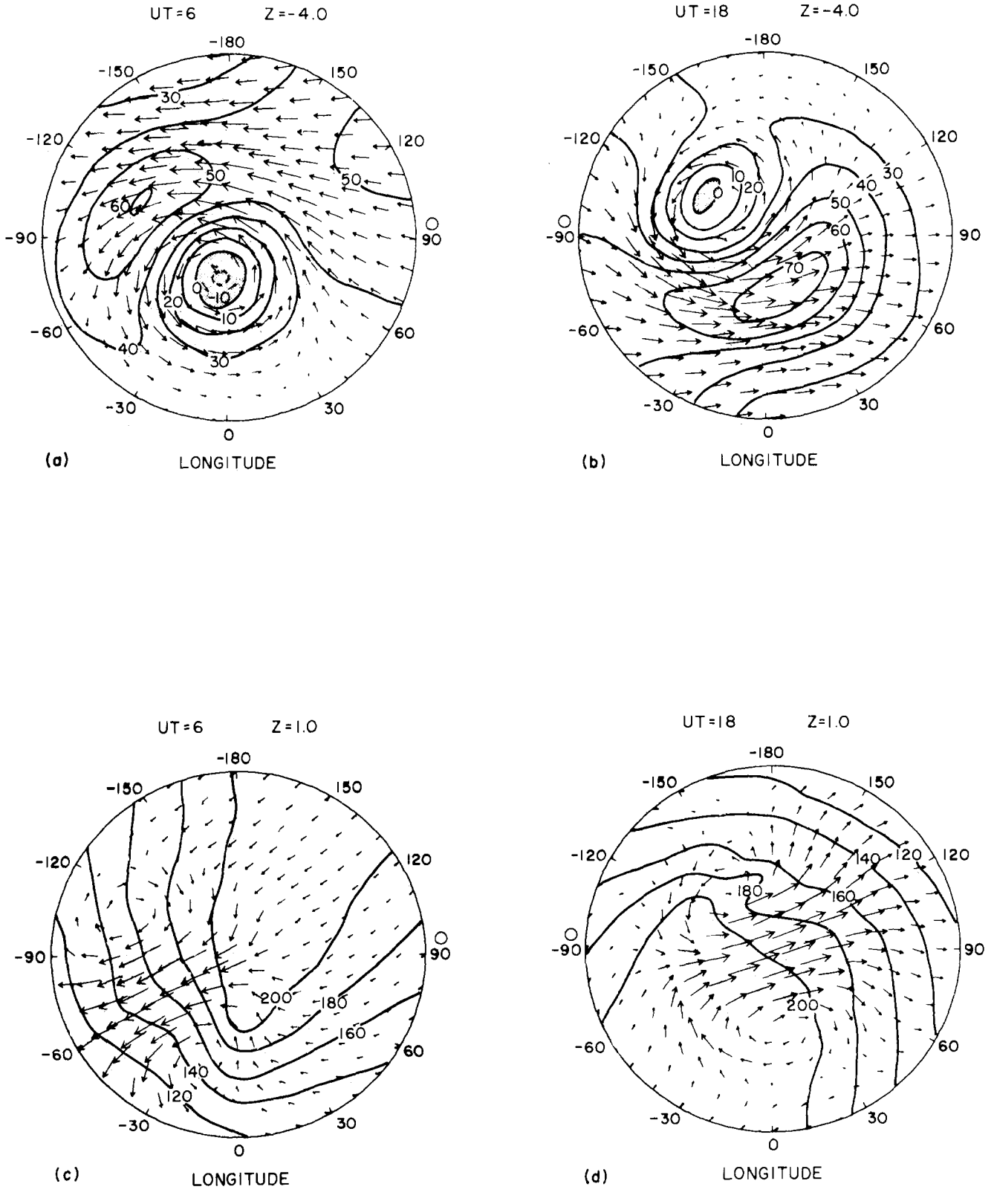

Figure 17-32. Winds and contours of perturbation temperature (K) along the z = −4 (130 km) surface for two universal times, 0600 UT (a) and 1800 UT (b), and along the z = +1 (300 km) surface at 0600 UT (c) and 1800 UT (d) for the case where the geographic and geomagnetic poles are displaced and the cross-tail potential for the magnetospheric convection is 60 kV. The circulation is indicated by the arrows giving direction, and the length is the magnitude of the winds. The length of the maximum arrow represents 100 m/s in (a), 109 m/s in (b), 395 m/s in (c), and 373 m/s in (d). Local noon is indicated by an open circle on the boundary [Roble et al., 1982].

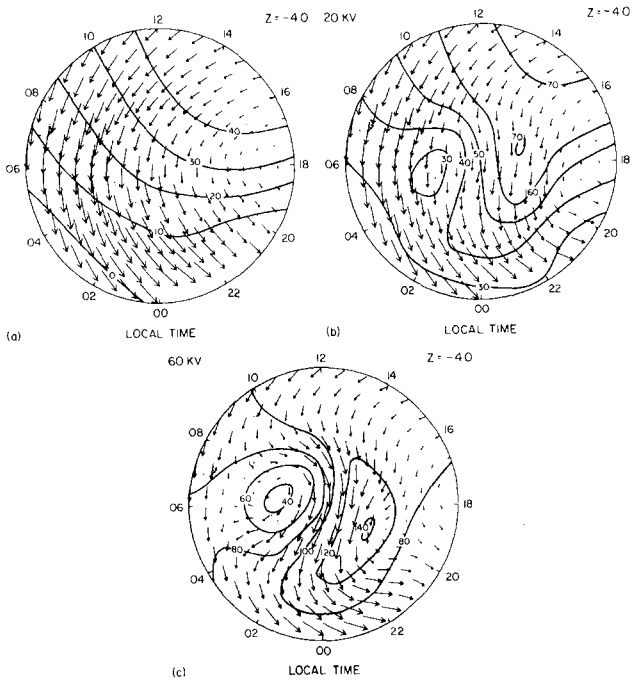

Figure 17-33. Polar plots giving the direction and magnitude of the calculated southern hemisphere (summer) high-latitude circulation and contours of perturbation temperature (K) along the z = −4 (130 km) constant-pressure surface at December solstice for (a) solar heating only, (b) solar heating plus magnetospheric convection with a cross-tail potential of 20 kV, and (c) solar heating plus magnetospheric convection with a cross-tail potential of 60 kV. The wind speed associated with the maximum arrow is 75 m/s in (a), 77 m/s in (b) and 89 m/s in (c) [Roble et al., 1983]. (Reprinted with permission from Pergamon Press Ltd. © 1983.)

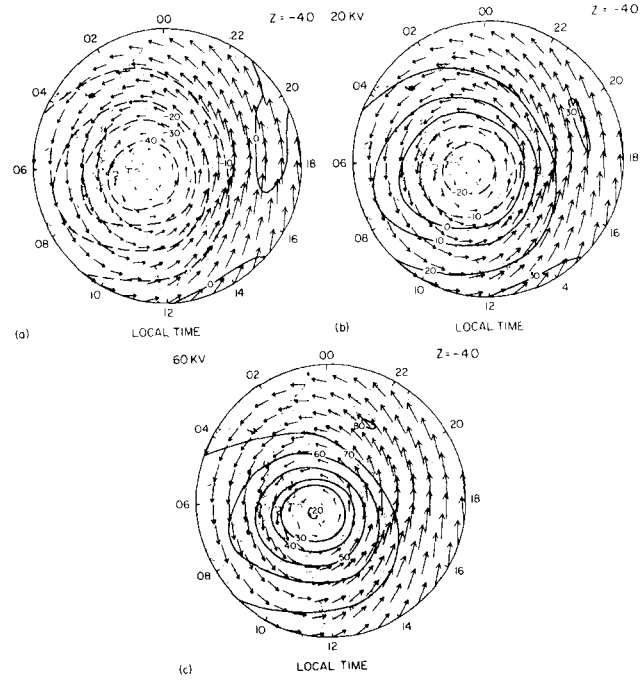

Figure 17-34. Polar plots giving the direction and magnitude of the calculated northern hemisphere (winter) high-latitude circulation and contours of perturbation temperature (K) along the z = −4 (130 km) constant-pressure surface at December solstice for (a) solar heating only, (b) solar heating plus magnetospheric convection with a cross-tail potential of 20 kV, and (c) solar heating plus magnetospheric convection with a cross-tail potential of 60 kV. The wind speed associated with the maximum arrow is 108 m/s in (a), 117 m/s in (b) and 120 m/s in (c) [Roble et al., 1983]. (Reprinted with permission from Pergamon Press Ltd. © 1983.)

in Figure 17-36. As for the corresponding case at 120 km, the circulation patterns for the zero and 20 kV cases are similar, with the maximum wind increasing from 181 (Figure 17-36a) to 200 m/s (Figure 17-36b). For the 60 kV case (Figure 17-36c) polar winds increase to 330 m/s. These winds also show a surge near 0200 LT. There is again a tendency to follow the two-cell pattern of magnetospheric convection with a reduced effect due to the lower winter electron densities.

Pole-to-pole cylindrical equidistant projections of winds and temperatures as a function of local time as given by Roble et al. [1983] are shown in Figure 17-37 for 120 km and Figure 17-38 for 300 km. Figure 17-37 shows that the major effect of magnetospheric convection in the lower thermosphere occurs at high latitudes in the summer with a 60 kV potential as discussed previously. In the upper thermosphere (Figure 17-38) the 60 kV potential has a much more pronounced influence on the high-latitude circulation. Maximum winds of about 400 m/s occur at high latitudes near local midnight and are equatorward. Changes are observed even at lower latitudes, indicating that the high-latitude energy input is redistributed globally by the thermospheric wind system.

Roble et al. [1983] also give meridional winds and temperature data in altitude-latitude coordinates. Results are given for the cases of a zero and a 60 kV potential for local times of 1200 h and 0000 h. In Figures 17-39 (1200 LT) and 17-40 (0000 LT) the top two plots show temperatures for the two heating cases and the bottom two plots show the corresponding wind fields. At 1200 LT, maximum velocities for solar heating only are 75 m/s and 125 m/s over the summer and winter poles respectively. The inclusion of magnetospheric convection increases the flow over the pole to 150 m/s and 300 m/s for the summer and winter cases respectively. Also, the higher summer electron densities permit the ion drag acceleration source to accelerate the winds down to about 130 km in the summer hemisphere compared to about 180 km in the winter hemisphere. Along the 0000 LT meridian, comparison of Figures 17-40a and b shows the magnetospheric convection greatly enhances equatorward flow. As the cross-tail potential is increased from zero to 60 kV, winds over the summer pole increase from 100 m/s to 400 m/s while over the winter pole they increase from 100 m/s to 300 m/s. The sharp wind gradient near 60° in both hemispheres indicates the equatorward limit of magnetospheric convection forcing for this local time.

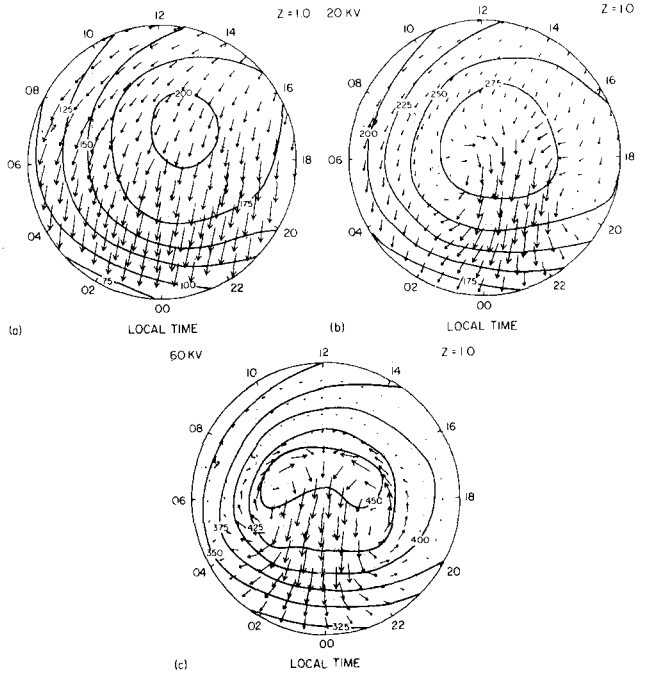

Figure 17-35. Polar plots giving the direction and magnitude of the calculated southern hemisphere (summer) high-latitude circulation and contours of perturbation temperature (K) along the z = +1 (~300 km) constant-pressure surface at December solstice for (a) solar heating only, (b) solar heating plus magnetospheric convection with a cross-tail potential of 20 kV, and (c) solar heating plus magnetospheric convection with a cross-tail potential of 60 kV. The wind speed associated with the maximum arrow is 110 m/s in (a), 200 m/s in (b), and 380 m/s in (c) [Roble et al., 1983]. (Reprinted with permission from Pergamon Press Ltd. © 1983.)

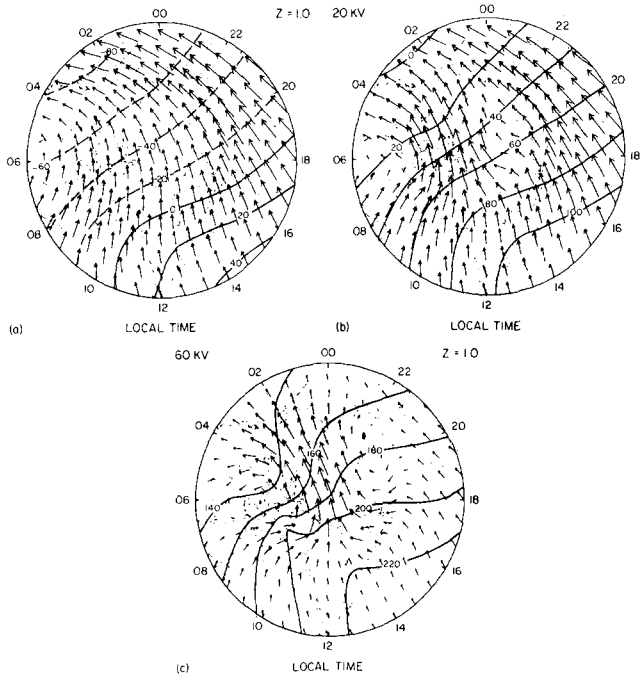

Figure 17-36. Polar plots giving the direction and magnitude of the calculated northern hemisphere (winter) high-latitude circulation and conturs of perturbation temperature (K) along the z = +1 (~300 km) constant-pressure surface at December solstice for (a) solar heating only, (b) solar heating plus magnetospheric convection with a cross-tail potential of 20 kV, and (c) solar heating plus magnetospheric convection with a cross-tail potential of 60 kV. The wind speed associated with the maximum arrow is 181 m/s in (a), 200 m/s in (b), and 339 m/s in (c) [Roble et al., 1983]. (Reprinted with permission from Pergamon Press Ltd. © 1983.)

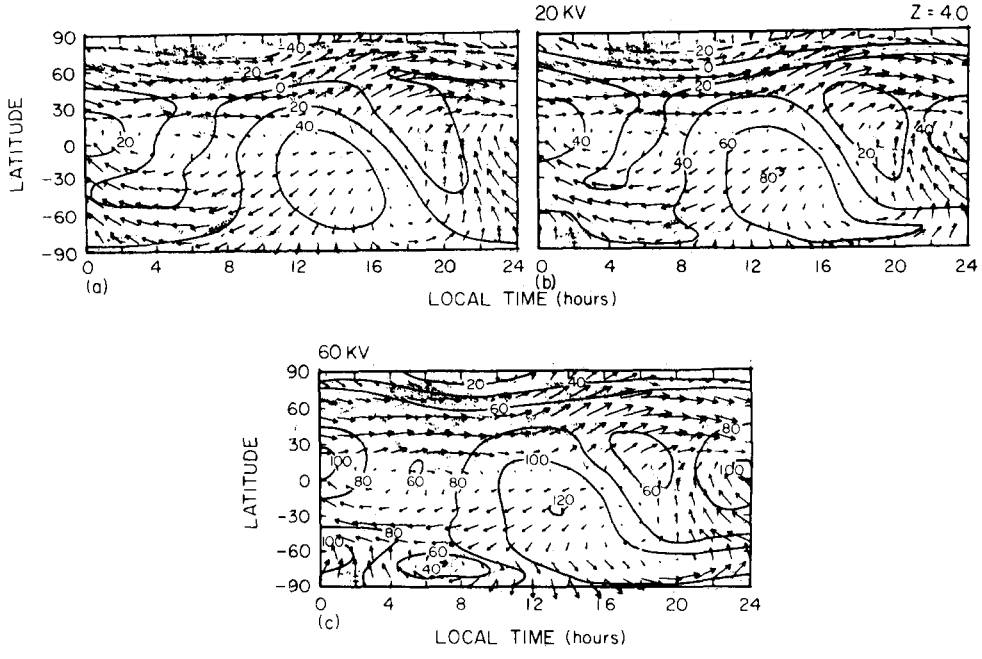

Figure 17-37. Cylindrical equidistant projections giving the direction and magnitude of the calculated circulation and contours of perturbation temperature (K) along the z = −4 (130 km) constant-pressure surface for December solstice for (a) solar heating only, (b) solar heating plus magnetospheric convection with a cross-tail potential of 20 kV, and (c) solar heating plus magnetospheric convection with a cross-tail potential of 60 kV. The wind speed associated with the maximum arrow is 108 m/s in (a), 117 m/s in (b) and 120 m/s in (c) [Roble et al., 1983]. (Reprinted with permission from Pergamon Press Ltd. © 1983.)

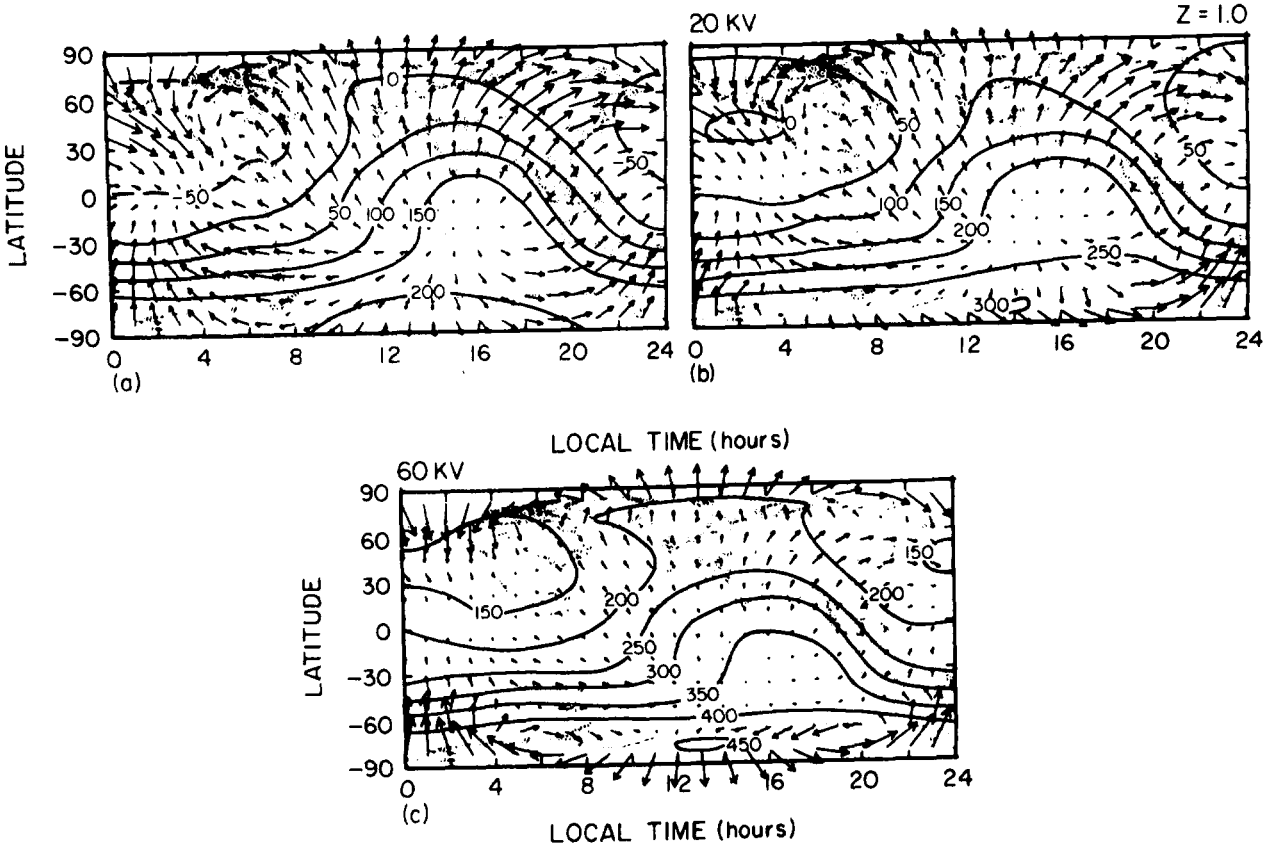

Figure 17-38. Cylindrical equidistant projections giving the direction and magnitude of the calculated circulation and contours of perturbation temperature (K) along the z = +1 (300 km) constant-pressure surface for December solstice for (a) solar heating only, (b) solar heating plus magnetospheric convection with a cross-tail potential of 20 kV, and (c) solar heating plus magnetospheric convection with a cross-tail potential of 60 kV. The wind speed associated with the maximum arrow is 181 m/s in (a), 220 m/s in (b) and 380 m/s in (c) [Roble et al., 1983]. (Reprinted with permission from Pergamon Press Ltd. © 1983.)

The TGCM model has been run to simulate conditions encountered by the Dynamics Explorer (DE-2) satellite. Results from two on-board wind sensors [Killeen et al., 1982; Spencer et al., 1982] were combined to provide thermospheric winds along the spacecraft path, at an altitude of about 300 km. These data were then compared to the TGCM predictions. Experimental data obtained on the four orbits over high southern latitudes, shown in Figure 17-41a are considered representative of summer conditions. Local times are between night and early morning hours. Data are shown in polar plots and in geomagnetic coordinates. Further details of these data are in the paper by Roble et al. [1983]. This figure shows strong control of the winds by magnetospheric convection and the characteristic two-cell convection pattern. Maximum winds are over the polar cap and have velocities between 500 and 750 m/s. Winter (northern hemisphere) polar data for three passes are shown in Figure 17-41b. Local times are during twilight and daytime hours. Magnetospheric convection control of the winds is evidenced by their similarity with those for summer conditions. Maximum speeds of 500–800 m/s are found in the polar cap. In the auroral oval, the winds are sunward with speeds of about 300 m/s. The TGCM simulations used a 60 kV potential and displaced geographic and geomagnetic poles. Results for the summer and winter cases are given in Figures 17-42a and b respectively. The model data generally agree with the direction of the experimental data. However, the model wind magnitudes underestimate the measured winds. Maximum model values are 400–500 m/s. Roble et al. [1983] note that better agreement could be obtained by increasing the cross-tail potential and ion-drift velocities in the magnetospheric convection model, but that such a modification is not warranted until the ion-drag momentum source is better defined (from DE-2 satellite plasma measurements).

Roble et al. [1983] have also examined whether a linear combination of solar-driven and high-latitude auroral-driven circulation and temperature structures reproduce the total structure. Such a linear combination would allow high-latitude plasma-dynamic interactions with neutral gas to be analyzed independently, with the results superimposed linearly on the solar-driven results. This would have the advantages of simplifying analyses of Dynamics Explorer data and placing more confidence in linear perturbation model approaches to thermospheric dynamic studies. Their finding

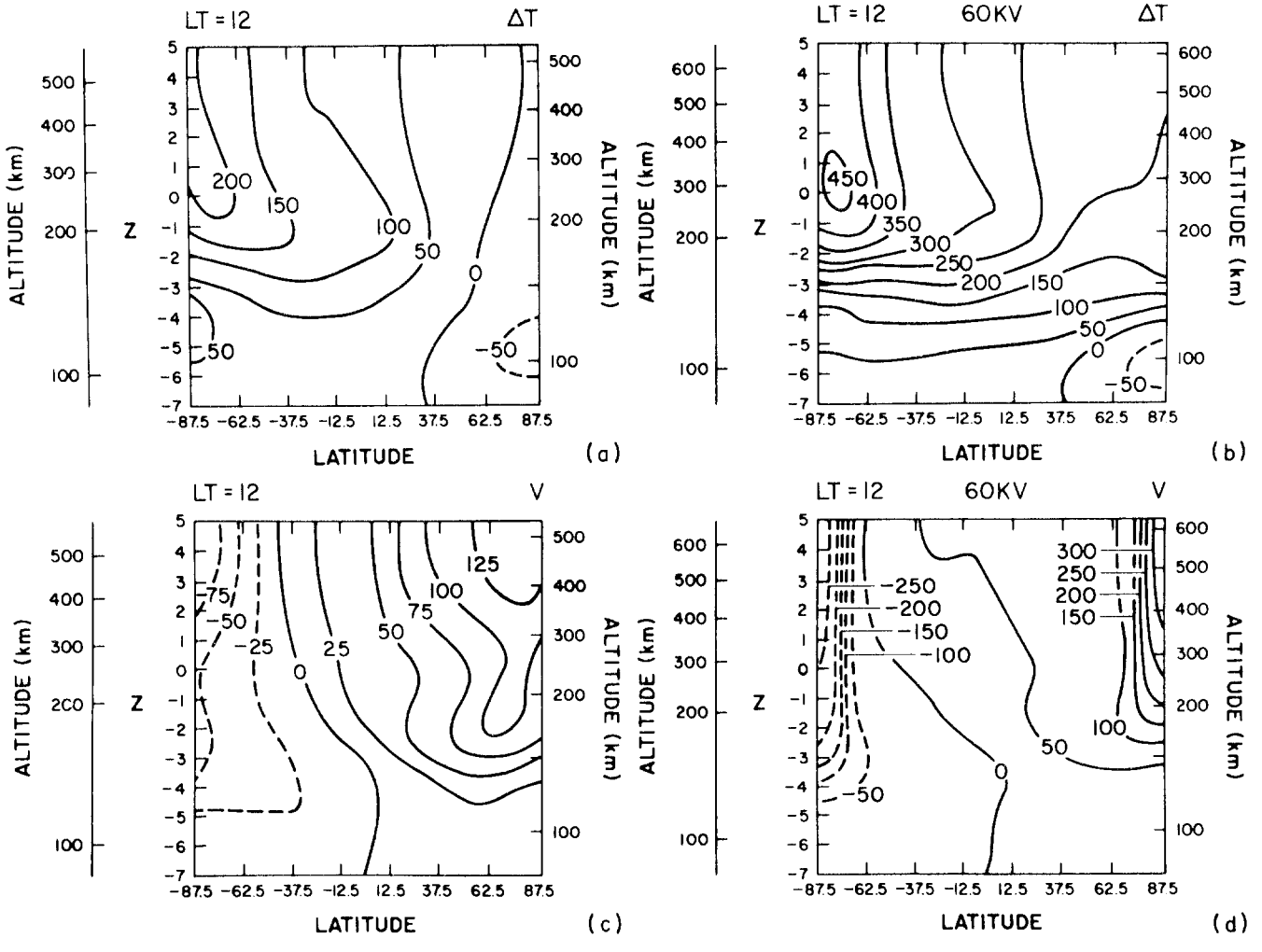

Figure 17-39. Meridional cross sections giving contours of the calculated perturbation temperature (K) [(a) and (b)] and meridional wind speed (m/s, positive northward) [(c) and (d)], respectively. The local time of the meridional slice is 1200 LT. (a) and (c) are the perturbation temperature and meridional wind for the case of solar heating only, and (b) and (d) are the perturbation temperature and meridional wind for the case of solar heating plus magnetospheric convection with a cross-tail potential of 60 kV [Roble et al., 1983]. (Reprinted with permission from Pergamon Press Ltd. © 1983.)

was that a linear superposition is accurate to within 10%–20% at F region heights, where motion is mainly controlled by the ion drag momentum source. In the lower thermosphere the linear combination is not a good approximation, apparently because of the non-linear nature of energy transport by winds and of Joule heating which is a function of the square of the difference between neutral and ion velocities. It therefore appears that non-linear models are required for lower thermospheric studies.

Thermospheric wind variations as a function of time due to a substorm corresponding to moderate geomagnetic activity have been calculated by Fuller–Rowell and Rees [1981]. These results were derived using the global three-dimensional, time-dependent numerical model of Rees et al. [1980]. Fuller-Rowell and Rees [1981] estimate that their input cross-tail potentials for the example given here represent a variation in Kp from about one to about six and back to about one in successive 3-h intervals. Equinoctial solar maximum conditions and coincident geographic and geomagnetic poles are assumed. Winds are calculated for altitudes 120 and 240 km from onset of the storm to 4.5 h after onset at 20-min intervals. Results are shown here at t = 0, 1, and 2 h to indicate the complex nature of the time-varying response. Longer term effects are also noted in the text. Data are again presented as polar plots from 50°–90° north geographic latitude. Arrows representing winds are scaled to 40 m/s = 2° latitude at 120 km and 160 m/s = 2° latitude at 240 km.

Pre-storm conditions, t = 0, at 120 km (Figure 17-43a) show a strong anti-solar flow in the evening polar cap which partially returns via a ~40 m/s sunward flow in the morning auroral oval. It is partially deflected in the midnight region into the westward flow of the evening auroral oval (2000–0200 LT) to eventually rejoin the general anti-sunward flow. These results are in general agreement with the 20 kV data of Roble et al. [1982] shown in Figure 17-29a. At t = 1 h (Figure 17-43b) peak wind amplitudes of ~180 m/s occur.

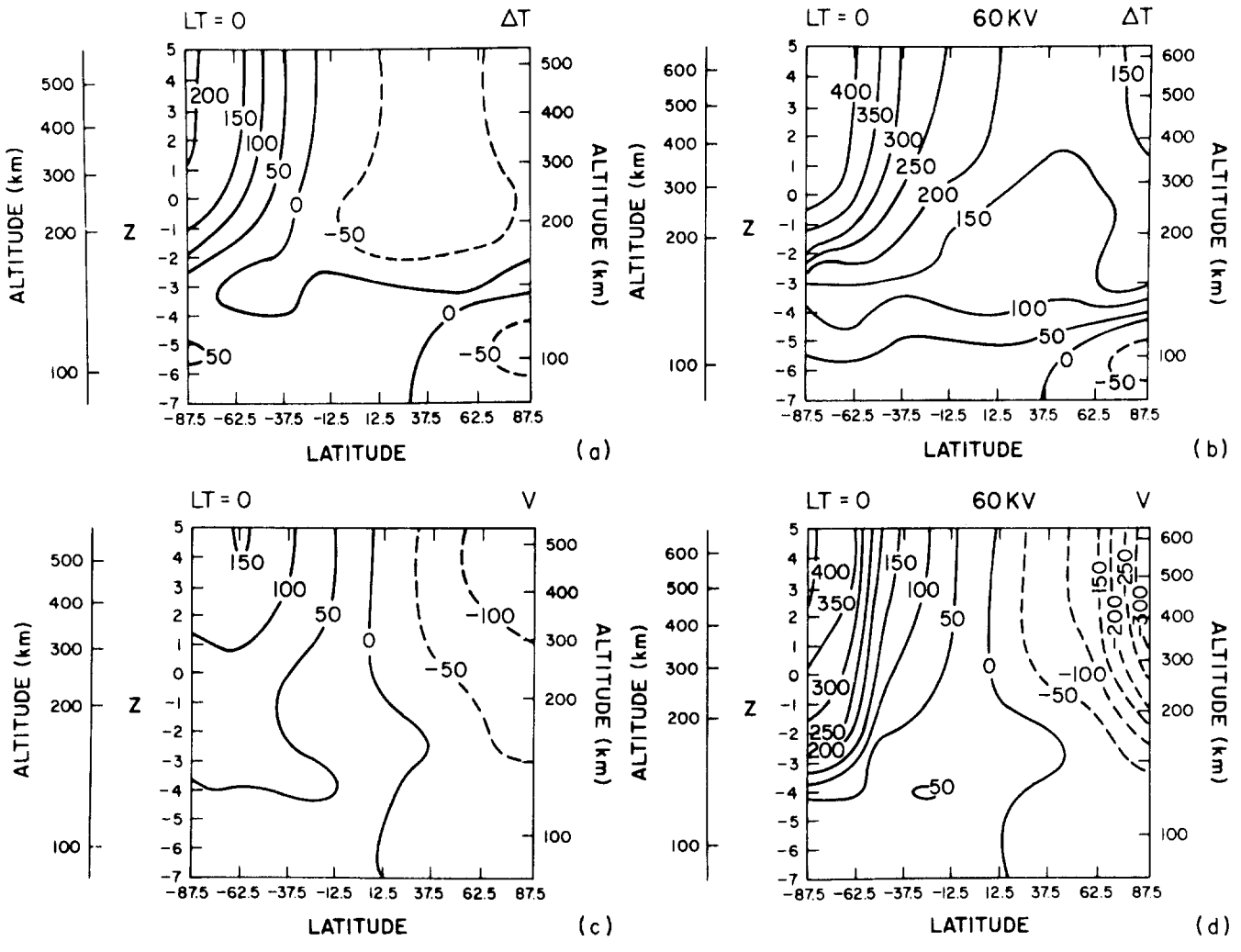

Figure 17-40. Meridional cross sections giving contours of the calculated perturbation temperature (K) [(a) and (b)] and meridional wind speed (m/s, positive northward) [(c) and (d)], respectively. The local time of the meridional slice is 0000 LT. (a) and (c) are the perturbation temperature and meridional wind for the case of solar heating only, and (b) and (d) are the perturbation temperature and meridional wind or the case of solar heating plus magnetospheric convection with a cross-tail potential of 60 kV [Roble et al., 1983]. (Reprinted with permission from Pergamon Press Ltd. © 1983.)

Other significant features are poleward winds in the afternoon sector south of 70°N latitude, equatorward winds from midnight to midday in the morning region south of 65°N latitude and a steadily increasing surge from dusk to dawn over the polar cap. At t = 2 h (Figure 17-43c) velocities have fallen to about half their maximum values. Also, an anti-cyclone circulation has been established with center near 2200 LT and 74° latitude. There is also a complimentary cyclonic cell centered near 1000 LT and 74° latitude. These cells have velocities of 160 m/s and decrease very slowly with time. At 4.5 h after onset the winds south of 65°N latitude revert to essentially pre-storm conditions in the afternoon and evening. In the morning sector equatorward winds of 60 m/s persist. Poleward of 65° latitude the anticyclonic nighttime and weaker cyclonic daytime vortices continue, along with the connecting dusk to dawn flow. Fuller-Rowell and Rees [1981] indicate that these vortices may persist for several more hours.

Greater wind magnitudes are observed at 240 km. The anti-sunward flow over the polar cap at t = 0 (Figure 17-44a) is about 300 m/s (compared with 150 m/s when solar heating is the only source in the thermosphere). Also, in the late evening auroral oval (1600-2400 LT) there is a significant sunward flow which forms a cell centered about 72° latitude with closure over the polar cap. South of 60°N latitude the wind circulation is only slightly modified by the electric field. One hour into the substorm (Figure 17-44b), winds in the evening auroral oval and over much of the polar cap exceed 300 m/s. Near 1500 LT and 73° latitude the velocity is 450 m/s. Horizontal winds converge near 70°–75° latitude and 1200 LT due to the auroral oval jets. While not evident in the limited data shown here, there are strong oscillations due to gravity waves which have already propagated to 50° latitude in the early morning hours, affecting both zonal and meridional winds. Wind magnitudes in the midday region have been significantly decreased but

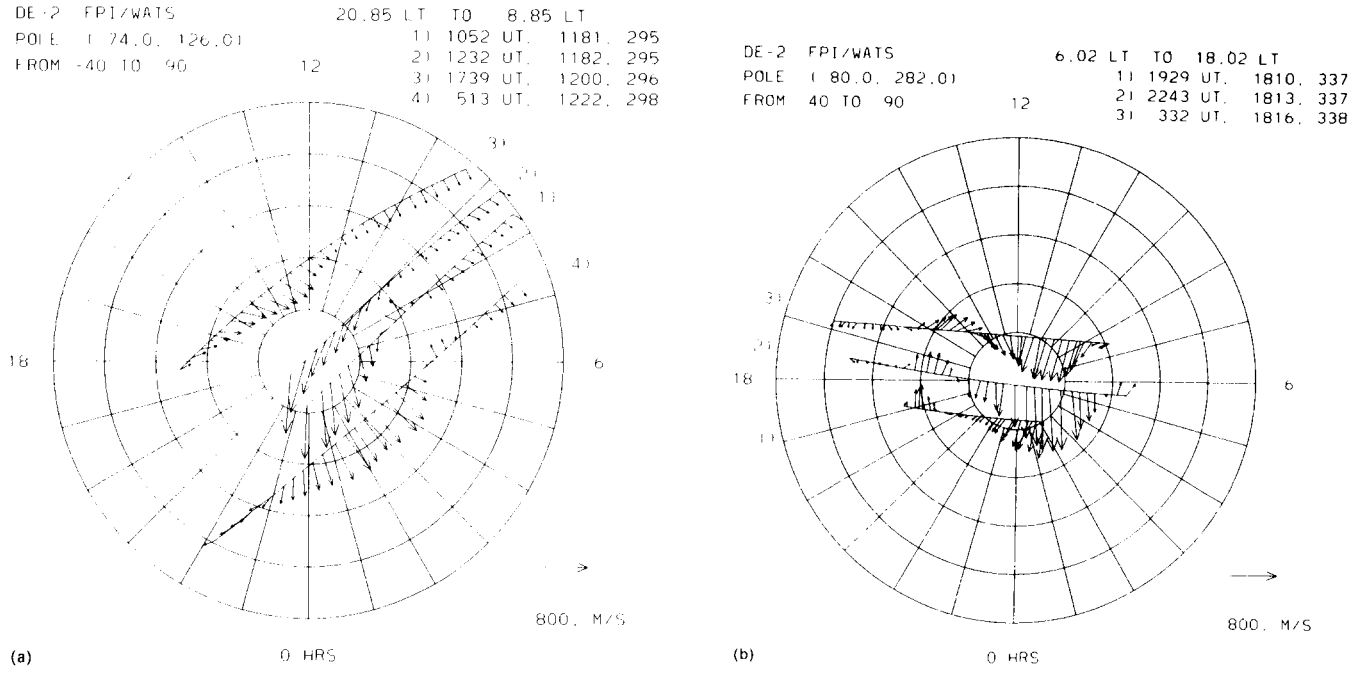

Figure 17-41. Polar plots of the measured wind vector at F-region heights along the DE-2 satellite path: (a) winds on four orbits measured over the southern magnetic polar cap on 22-23 Oct 1981 and (b) winds measured on three orbits over the northern magnetic polar cap on 3-4 Dec 1981 [Roble et al., 1983]. (Reprinted with permission from Pergamon Press Ltd. © 1983.)

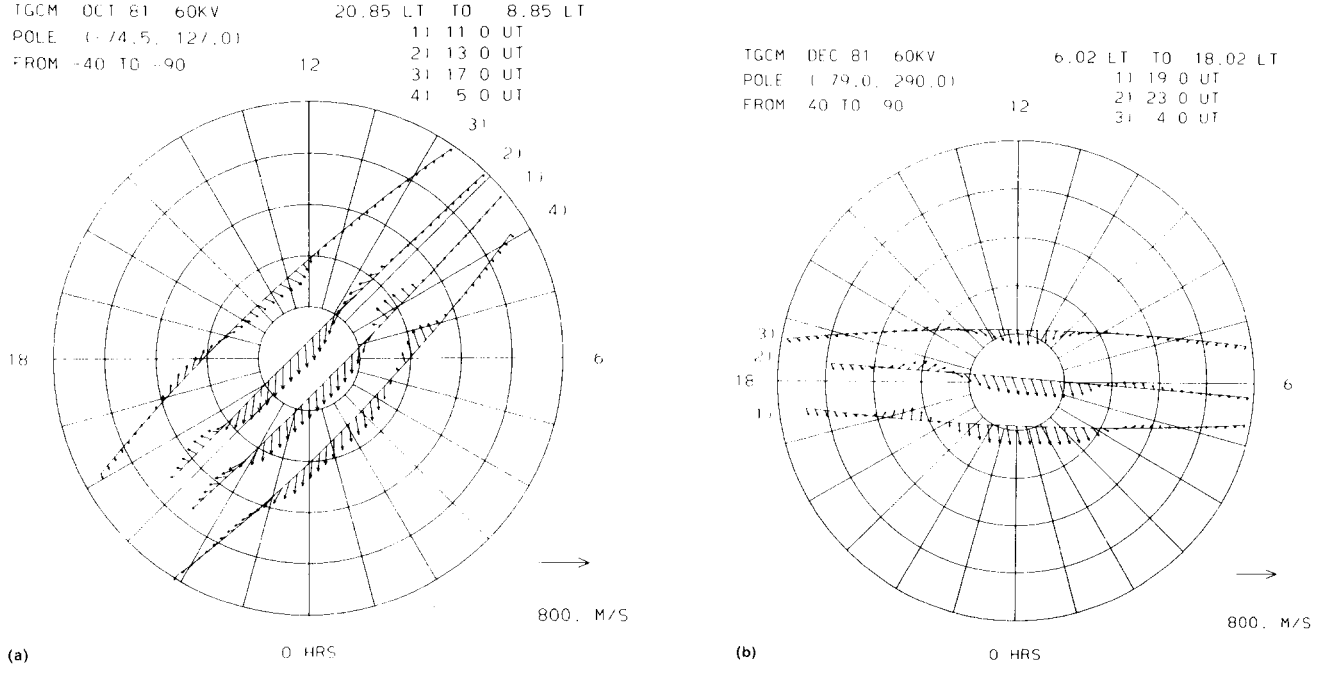

Figure 17-42. Polar plots of the calculated wind vector at F region heights along the same DE-2 satellite paths shown in Figure 17-31: (a) winds for the same four orbits over the southern hemisphere magnetic polar cap in October and (b) winds for the same three orbits over the northern magnetic polar cap in December [Roble et al., 1983]. (Reprinted with permission from Pergamon Press Ltd. © 1983.)

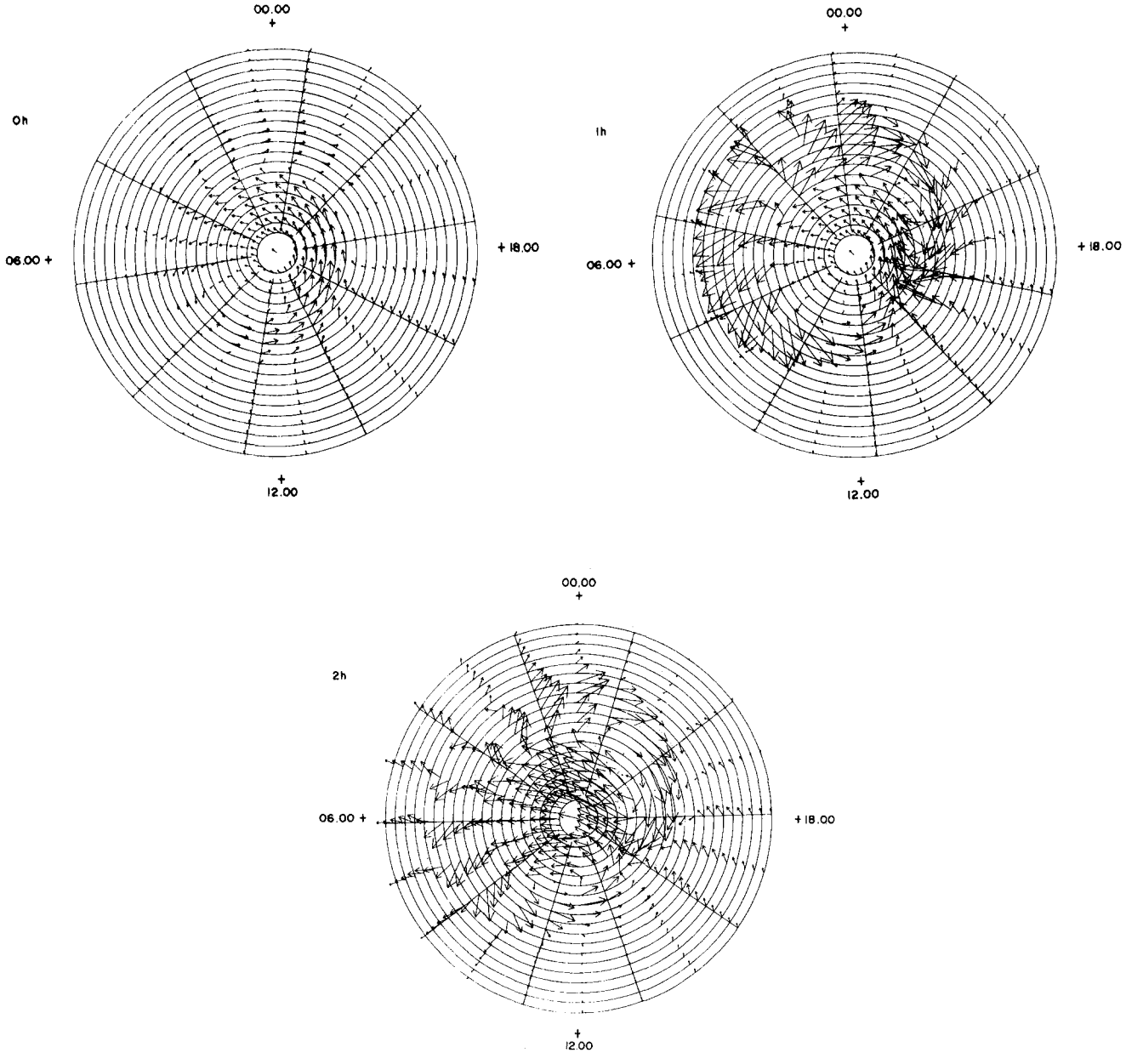

Figure 17-43. Polar plot of dynamical response of winds at 120 km to a large geomagnetic storm at (a) t = 0 h, (b) t = 1 h, and (c) t = 2 h. Winds are scaled to 40 m/s = 2° latitude [Fuller-Rowell and Rees, 1981]. (Reprinted with permission from Pergamon Press Ltd. © 1981.)

not reversed. Wind vectors over the polar cap appear to converge toward the midnight part of the auroral oval. This is due to the poleward gravity wave launched by the dayside auroral oval. The high velocity ion flow over the polar cap also provides momentum to drive surges of equatorward winds at midlatitude, particularly between midnight and dawn. At t = 2 h (Figure 17-44c) the morning circulation cell is tending to collapse, but the evening cell is hardly reduced. Polar cap winds have steadily increased to maximum values greater than 600 m/s in the night sector between 64°–70° latitude. Evidence of gravity wave characteristics are again observed. On the nightside (2200 LT to 0900 LT) strong oscillations of both meridional and zonal winds occur with latitude and longitude. Also, the dayside anti-solar circulation has been stopped, or "deflected" since the late morning winds are strongly enhanced relative to the case for solar heating only. At t = 4 h, the model runs show that the late morning circulation is still enhanced and that gravity waves reach mid to low latitudes. Simulations run out to 12 h after onset show that the wind circulation has not yet returned to prestorm conditions.

An improved version of this model has been developed

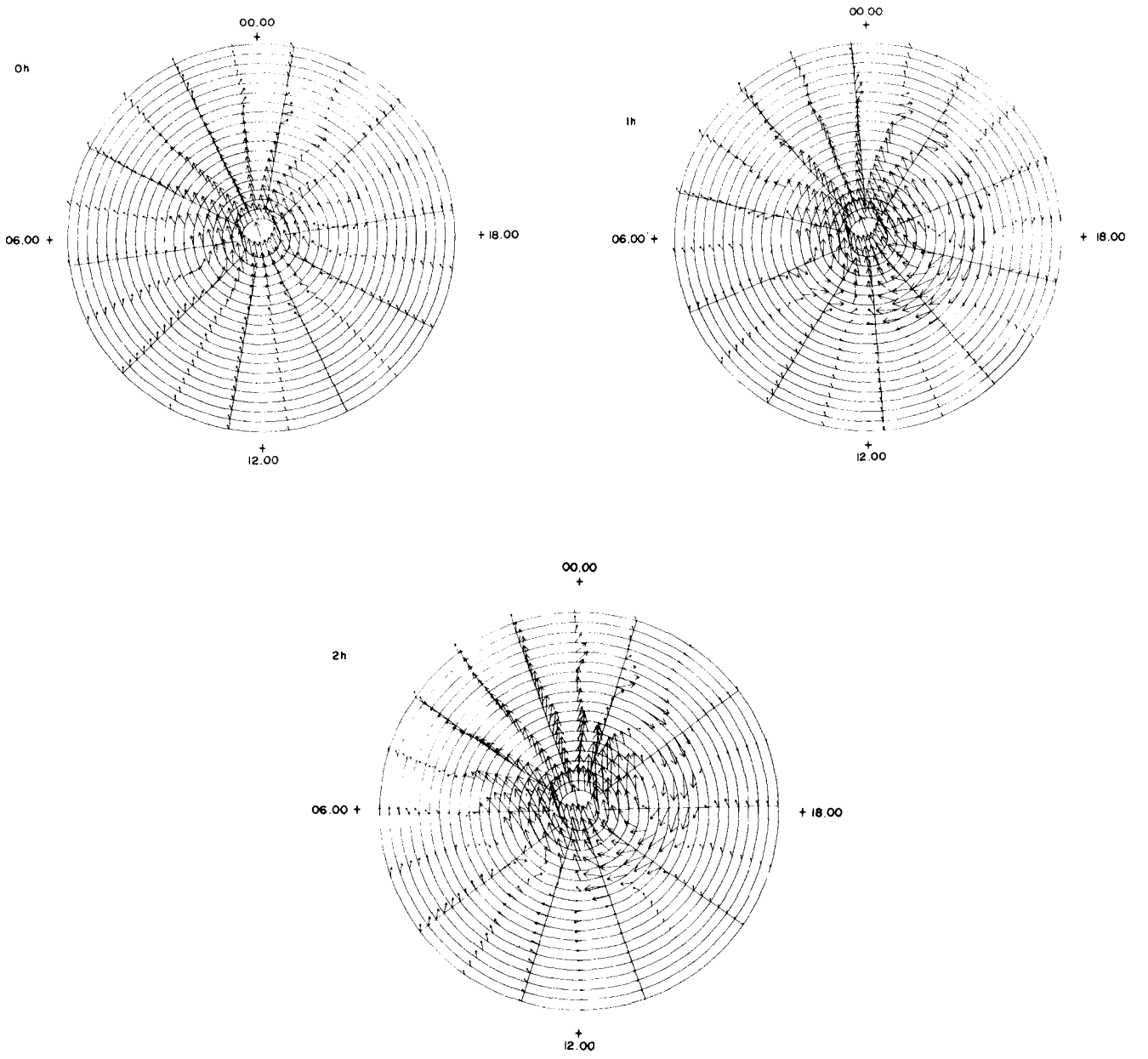

Figure 17-44. Polar plot of dynamical response of winds at 240 km to a large geomagnetic storm at (a) t = 0 h, (b) t = 1 h, and (c) t = 2 h. Winds are scaled to 160 m/s = 2° latitude [Fuller-Rowell and Rees, 1981]. (Reprinted with permission from Pergamon Press Ltd. © 1981.)

[Rees et al., 1983]. It incorporates the theoretical treatment by Quegan et al. [1982] of the polar and auroral ionosphere. This results in a much more realistic electron density distribution at high latitudes during other than low geomagnetic conditions since ionization enhancements due to magnetospheric phenomena are reflected. This second dynamical model and the earlier version [Rees et al., 1980] have been compared to the same DE-2 Oct 81 and Dec 81 data shown in Figure 17-41. Only a brief description of the extremely comprehensive analyses given by Rees et al. [1983] is presented below.

The DE-2 wind data, denoted "KVEC", are shown for each orbit in Figures 17-45 and 17-46 as a function of geographic latitude. The left side of the graph shows evening data and the right side of the graph shows morning data for the October data (Figure 17-45) while the reverse occurs for the December data (Figure 17-46). Model data for quiet geomagnetic conditions (labeled "CHIU") and moderately disturbed conditions (labeled "SHEFFIELD") are shown respectively above and below the experimental data for each orbit. The "SHEFFIELD" results are from the new dynamical model using variable electron densities. The following

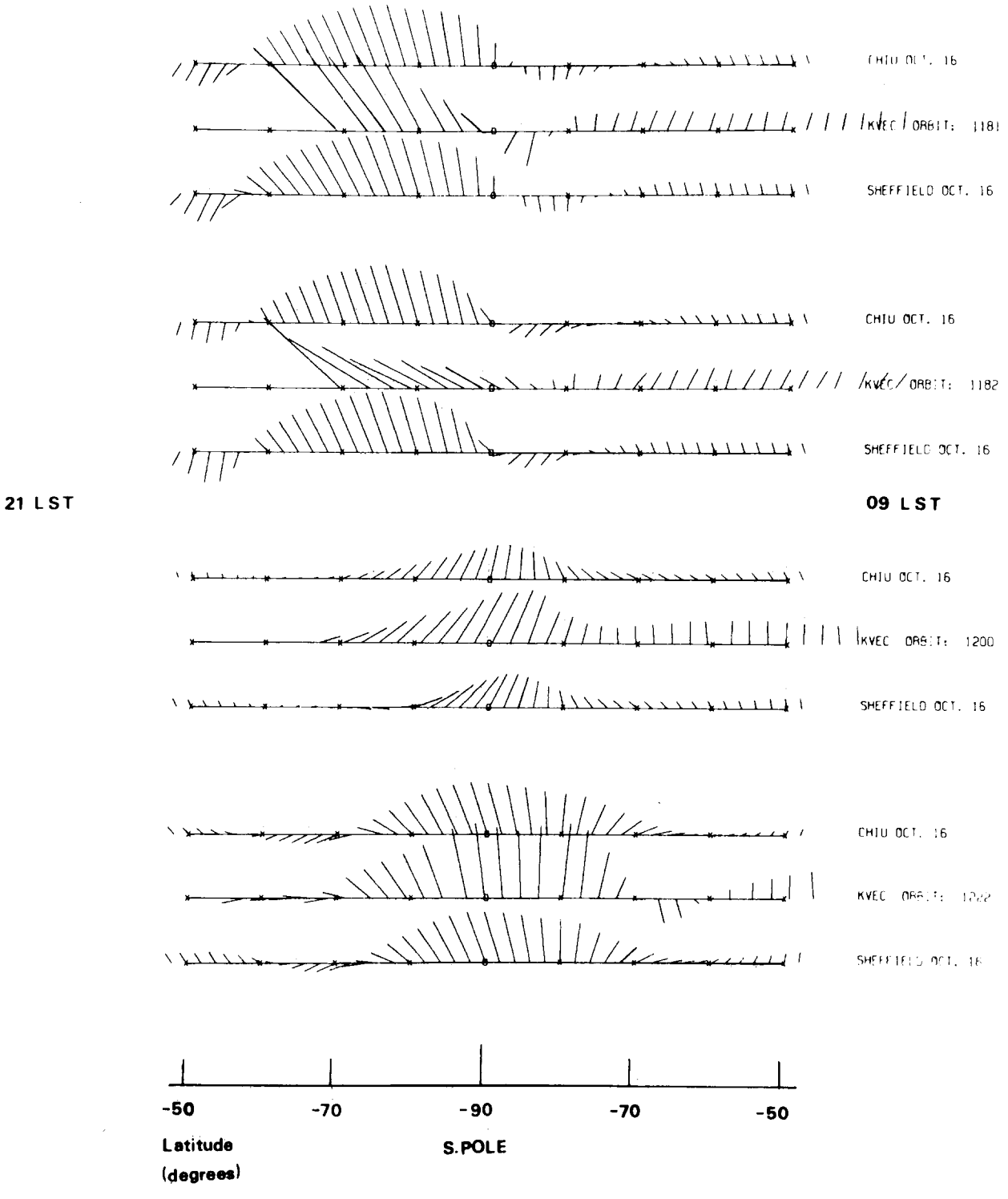

Figure 17-45. Comparison between each individual southern (Oct 1981) polar pass (marked KVEC orbit No.) and the corresponding polar slices from two theoretical global (three-dimensional time-dependent) model simulations at 320 km. Chiu—Quiet geomagnetic conditions. Sheffield—Moderately-disturbed geomagnetic conditions. Scale; 10° latitude ≡ 667 m s [Rees et al., 1983]. (Reprinted with permission from Pergamon Press Ltd. © 1983.)

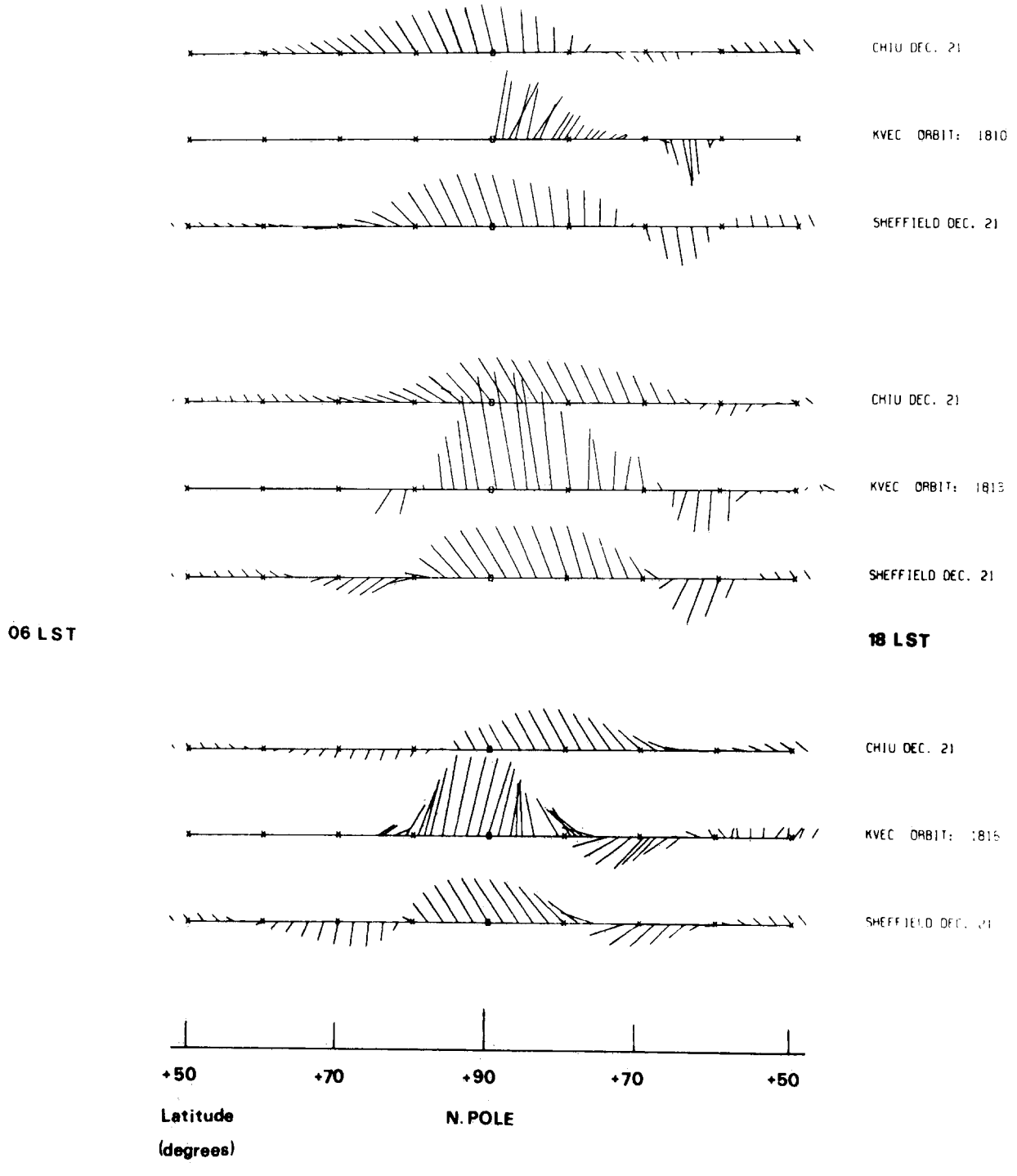

Figure 17-46. Comparison between each individual northern (Dec 1981) polar pass (marked KVEC orbit No.) and the corresponding polar slices from two theoretical global (three-dimensional time-dependent) model simulations at 320 km. Chiu—Quiet geomagnetic conditions. Sheffield—Moderately-disturbed geomagnetic conditions. Scale: 10° latitude ≡ 667 m s [Rees et al., 1983]. (Reprinted with permission from Pergamon Press Ltd. © 1983.)

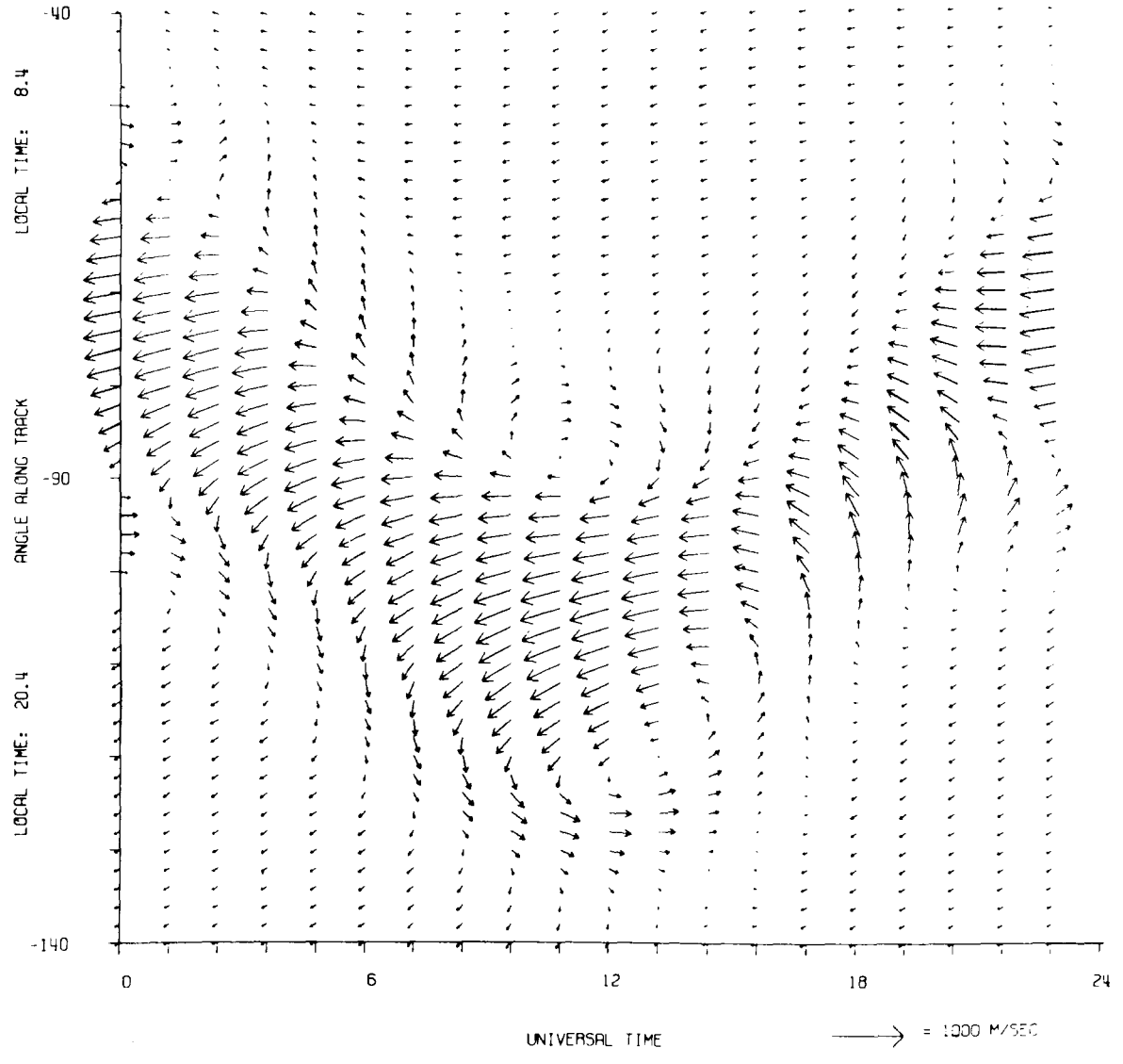

Figure 17-47. University College London three-dimensional, time-dependent neutral wind model. Separate geographic and geomagnetic poles. South geomagnetic pole: 74° Lat., 126° Long. Sheffield Electron Density Model plus Volland V2 Electric Field Model. 16 October simulation. Altitude 320 km; local time sector: 2040-0840 h. This presentation allows the UT geomagnetic dependence of vector winds from DE-2 to be compared orbit by orbit. Note this is not a flow pattern. Each slice is taken from the model at the same local time at 1.2 (U.T.) intervals as the earth rotates under the plane of the satelite orbit [Rees et al., 1983]. (Reprinted with permission from Pergamon Press Ltd. © 1983.)

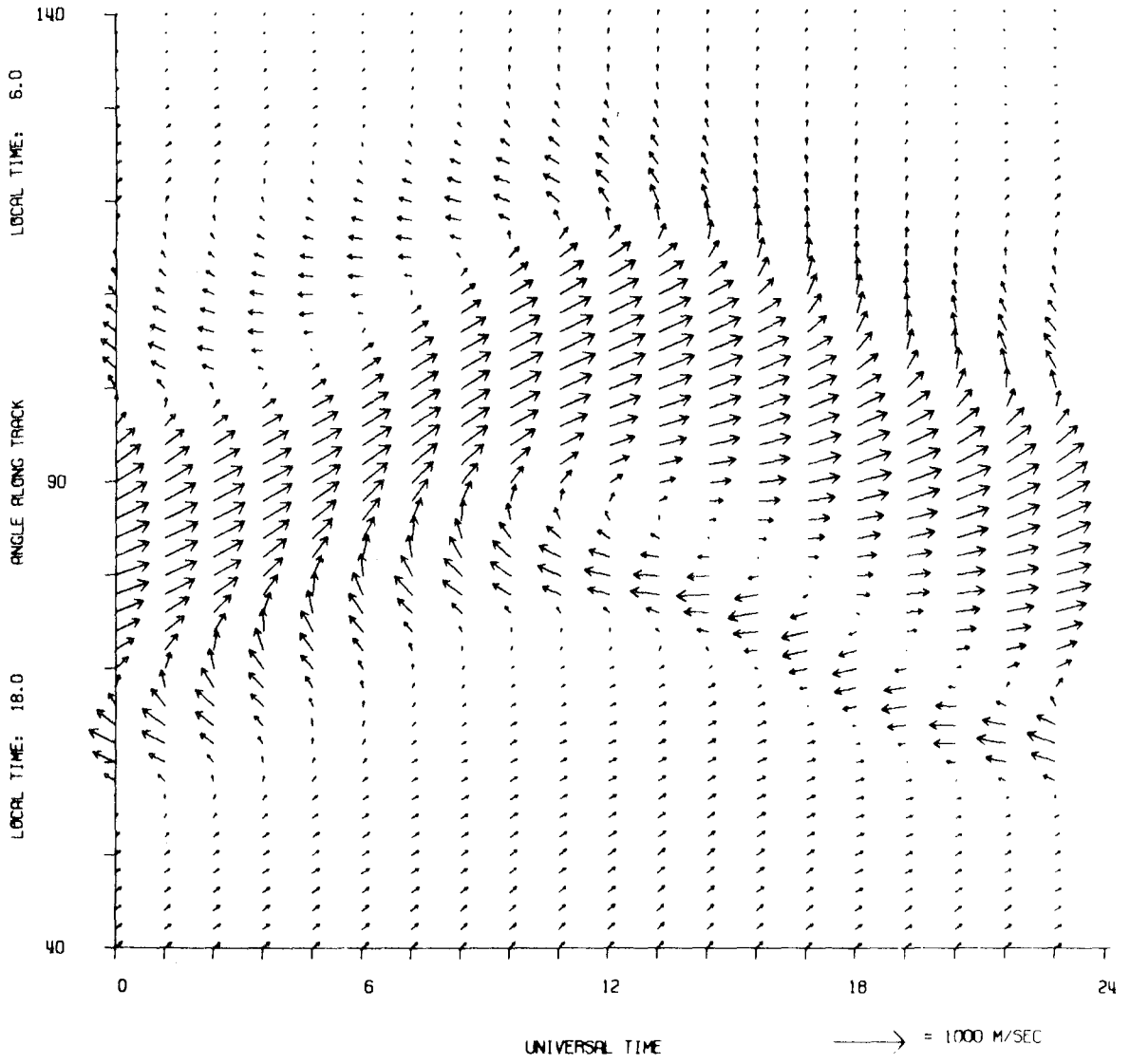

Figure 17-48. University College London three-dimensional, time-dependent neutral wind model. Separate geographic and geomagnetic poles. North geomagnetic pole: 80° Lat., 272° Long. Sheffield Electron Density Model plus Volland V2 Electric Field Model. 21 December simulation allows the UT geomagnetic dependence of vector winds from DE-2 to be compared orbit by orbit. Note this is not a flow pattern. Each slice is taken from the model at the same local time at 1.2 (UT) intervals as the earth rotates under the plane of the satellite orbit [Rees et al., 1983]. (Reprinted with permission from Pergamon Press Ltd. © 1983.)

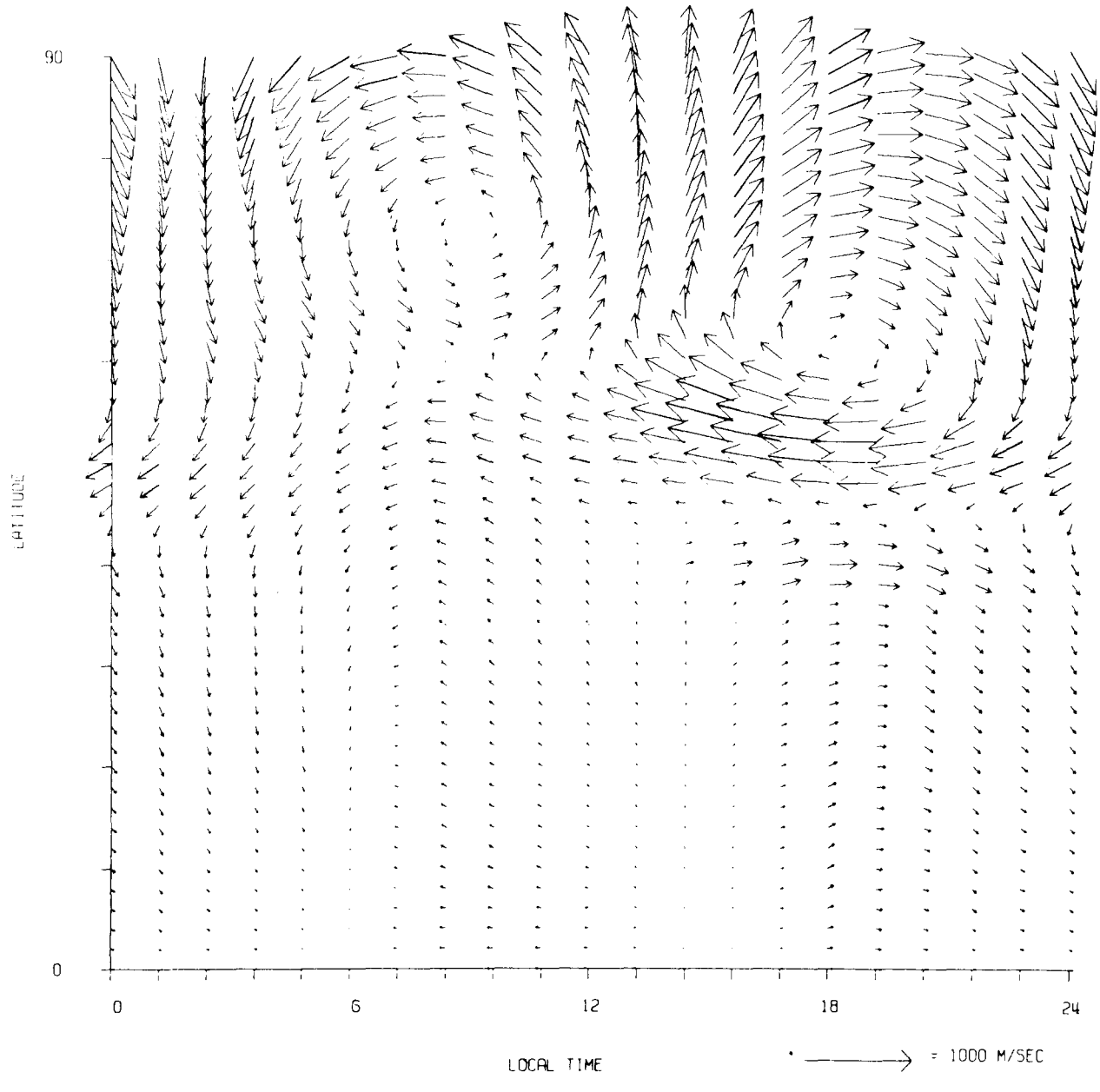

Figure 17-49. Storm-time simulation, University College London three-dimensional time-dependent neutral wind model. Separage geographic and geomagnetic poles. North geomagnetic pole: 80° Lat.; 272° Long. Sheffield Electron Density Model; LEF2 Large Electric Field Model; Expanded auroral oval and cross-cap potential, Altitude 320 km; U.T. 22.80. Note: This diagram shows the actual thermospheric flow pattern at 22.80 U.T. In December 1981, the DE-2 satellite was (approx.) in the 0600-1800 Local Solar Time plane and thus crossing the region of peak westward winds (~50°–60° geographical latitude at 22.80 U.T., over North America) [Rees et al., 1983]. (Reprinted with permission from Pergamon Press Ltd. © 1983.)

wind features were identified for each polar pass: (a) a region of strong antisunward flow over the geomagnetic polar cap with considerable variability within an orbit and from orbit to orbit, (b) sunward winds (or strongly reduced antisunward winds) in the dawn and dusk auroral ovals, (c) antisunward winds below the latitude of the auroral oval, as expected from a solar-driven source, and (d) highly variable high latitude winds with only a general correlation of velocity with geomagnetic activity.

The wind velocities in the different flow regimes and their dependence on Universal Time and geomagnetic events were studied further. The relation between ion drifts and neutral velocities showed that wind velocities are 30%–60% of ion velocities in the afternoon/evening auroral oval, greater than ion velocities over the polar cap, and not well correlated with ion velocities in the dawn/morning auroral oval. More detailed studies of the relationship between ion convection and neutral winds are planned using simultaneous electric field and ion drift data from DE-2. The UT variations in neutral winds as calculated from the moderate activity model for the local time planes of the Oct 81 and Dec 81 data are given in Figures 17-47 and 17-48 respectively. These plots are necessary to explain many features of the wind data related to locations of auroral oval boundaries. There is a modulation of about 45° in the geographic location of these boundaries as a function of Universal Time. Results of a simulated polar electric field enhanced to 130 kV, corresponding to a Kp value between ~5 and 7, are given in Figure 17-49. The predicted winds have been compared to those obtained during the disturbed Dec 81 period. At auroral oval latitudes the predicted winds exceed the measured data, but in the polar cap the maximum DE-2 winds (orbit 1813) are greater than the model values. The figure illustrates that during very disturbed periods the wind patterns and magnitudes accommodate to the expansion of the auroral oval and the increasing ion convection. Future studies are planned to examine these affects and to attempt to distinguish between effects of high latitude momentum and heating (Joule and particle heating) processes.

ACKNOWLEDGEMENTS

The critical comments of R. G. Roble, National Center for Atmospheric Research, Capt. D. V. Ridge, AFGL, and J. M. Forbes, Boston University, are greatly appreciated.

REFERENCES—CHAPTER 17

Abbey, R.F., Jr., "Risk Probabilities Associated with Tornado Windspeeds," *Proc. Symp. on Tornadoes,* Institute for Disaster Research, Texas Tech. Univ., Lubbock, Texas, 1976.

Amayenc, P., "Tidal Oscillations of the Meridional Neutral Wind at Midlatitudes," *Radio Sci.*, **9:** 281–294, 1974.

Arnold, A., and R. Bellucci, "Variability of Ballistic Meteorological Parameters," Tech Memo. No. M-1913, Ft. Monmouth, U.S. Army Sig. Eng. Lab, 1957.

Balsley, B.B., and K.S. Gage, "The MST Radar Technique: Potential for Middle Atmospheric Studies," *Pure Appl. Geophys.*, **118:** 452–493, 1980.

Bean, S.J., and P.N. Somerville, "Some Models for Windspeed," 4, AFGL-TR-79-0180, AD A077048, 1979.

Brekke, A.J., J.R. Doupnik, and P.M. Banks, "Observations of Neutral Winds in the Auroral-E Region During the Magnetospheric Storm of Aug 3–9, 1972," *J. Geophys. Res.*, **79:** 2248–2256, 1974.

Ching, B.K., and Y.T. Chiu, "A Phenomenological Model of Global Ionospheric Electron Density in the E, F1, and F2 Regions," *J. Atmos. Terr. Phys.*, **35:** 1616–1630, 1973.

Crutcher, H.L., "Upper Wind Statistics Charts of the Northern Hemisphere," NAVAIR 50-1C-535, 1959.

DeVries, L.L., "Analysis and Interpretation of Density Data from the Low-G Calibration System (Logacs)," *Space Res.*, **12:** 777–789, 1972.

Dickinson, R.E., E.C. Ridley, and R.G. Roble, "Medidional Circulation in the Thermosphere. I, Equinox Conditions," *J. Atmos. Sci.*, **2:** 1737–1754, 1975.

Dickinson, R.E., E.C. Ridley, and R.G. Roble, "Medidional Circulation in the Thermosphere. II, Solstice Conditions," *J. Atmos. Sci.*, **34:** 178–192, 1977.

Dickinson, R.E., E.C. Ridley, and R.G. Roble, "A Three-Dimensional General Circulation Model of the Thermosphere," *J. Geophys. Res.*, **86:** 1499–1512, 1981.

Ellsaesser, H.W., "Wind Variability," AWS Tech. Rept. No. 105-2, HQ Air Weather Service, Scott AFB, Ill., 1960.

Evans, J.V., "Ionospheric Movements Measured by Incoherent Scatter: A Review," *J. Atmos. Terr. Phys.*, **34:** 175, 1972.

Evans, J.V., "A Review of F Region Dynamics," *Res. Geophys. Space Phys.*, **13:** 887, 1975.

Evans, J.V., "Incoherent Scatter Contributions to Studies of the Dynamics of the Lower Thermosphere," *Rev. Geophys. Space Phys.*, **16:** 195, 1978.

Fichtl, G.H., "Small-Scale Wind Shear Definition for Aerospace Vehicle Design," *J. Spacecraft Rockets*, **9:** 79, 1972.

Forbes, J.M., "Atmospheric Tides 1. Model Descriptions and Results for the Solar Diurnal Components," *J. Geophys. Res.*, **87:** 5222–5240, 1982a.

Forbes, J.M., "Atmospheric Tides 2. The Solar and Lunar Semidiurnal Components," *J. Geophys. Res.*, **87:** 5241–5252, 1982b.

Forbes, J.M., and H.B. Garrett, "Theoretical Studies of Atmospheric Tides," *Rev. Geophys. Space Phys.*, **17:** 1951–1981, 1979.

Fuller-Rowell, T.J., and D. Rees, "A Three-Dimensional Time-Dependent Global Model of the Thermosphere," *J. Atmos. Sci.*, **37:** 2545–2567, 1980.

Fuller-Rowell, T.J., and D. Rees, "A Three-Dimensional Time-Dependent Simulation of the Global Dynamical Response of the Thermosphere to a Geomagnetic Substorm," *J. Atmos. Terr. Phys.*, **43:** 701, 1981.

Gage, K.S., and B.B. Balsley, "Doppler Radar Probing of the Clear Atmosphere," *Bull. Amer. Meteor. Soc.*, **59:** 1074–1092, 1978.

Golden, J.H., "An Assessment of Windspeeds in Tornadoes," *Proc. Symp. on Tornadoes,* Institute for Disaster Research, Texas Tech. Univ., Lubbock, Texas, 5–42, 1976.

Green, J.L., K.S. Gage, and T.E. Van Zandt, "Atmospheric Measurements by VHF Pulsed Doppler Radar," *IEEE Trans. Geosci. Elec.*, **GE-17:** 262–280, 1979.

Gregg, W.R., "An Aerological Survey of the United States," *Monthly Weather Review,* Supplement No 20: 1922.

Hays, P.B., and R.G. Roble, "Direct Observations of Thermospheric Winds during Geomagnetic Storms," *J. Geophys. Res.*, **76:** 5316–5321, 1971.

Hays, P.B., J.W. Meriwether, and R.G. Roble, "Nighttime Thermospheric Winds at High Latitudes," *J. Geophys. Res.*, **84:** 1905–1913, 1979.

Hays, P.B., T.L. Killeen, and B.C. Kennedy, "The Fabry-Perot Interferometer on Dynamics Explorer," *Space Sci. Instr.*, **5:** 395–416, 1981.

Heppner, J.F., "Empirical Models of High-Latitude Electric Fields," *J. Geophys. Res.*, **82:** 1115, 1977.

Heppner, J.F., and M.L. Miller, "Thermospheric Winds at High Latitudes from Chemical Release Observations," *J. Geophys. Res.*, **87:** 1633–1647, 1982.

Hernandez, G., and R.G. Roble, "Direct Measurements of Nighttime Thermospheric Winds and Temperatures. I. Seasonal Variations during Geomagnetic Quiet Periods," *J. Geophys. Res.*, **81:** 2065–2074, 1976a.

Izumi, Y., "Kansas 1968 Field Program," AFCRL-72-0041, AD739165, 1971.

Kantor, A.J., and A.E. Cole, "Wind Distributions and Interlevel Correlations, Surface to 60 Km," AFGL-TR-80-0242, ADA092670, 1980.

Kaufman, J.W. (ed.), "Terrestrial Environment (Climatic) Criteria Guidelines for Use in Aerospace Vehicle Design," NASA Tech. Memor. 78118, MSFC, 1977.

Kelley, M.C., T.S. Jorgensen, and I.S. Mikkelsen, "Thermospheric Wind Measurements in the Polar Region," *J. Atmos. Terr. Phys.*, **39:** 211–219, 1977.

Kelly, D.L., J.T. Schaeffer, R.P. McNulty, C.A. Doswell III, and R.F. Abbey Jr., "An Augmented Tornado Climatology," *Mon. Wea. Rev.*, **106:** 1172–1183, 1978.

Killeen, T.L., P.B. Hays, N.W. Spencer, and L.E. Wharton, "Neutral Winds in the Polar Thermosphere as Measured from Dynamics Explorer," *Geophys. Res. Lett.*, **9:** 957–960, 1982.

Knutson, J.R., D.C. Kayser, and W.E. Potter, "Mass Spectrometric Measurement of Thermospheric Wind," *J. Geophys. Res.*, **82:** 5253, 1977.

Lettau, H., *Atmospharische Turbulenz,* Akademische Verlagsgesellschaft M.B.H., Leipzig, 114, 1939.

Lettau, H., "A Re-examination of the 'Leipsig Wind Profile' Considering Some Relations Between Wind and Turbulence in the Frictional Layer," *Tellus,* **2:** 125, 1950.

Lettau, H.H., and B. Davidson (eds.), *Exploring the Atmosphere's First Mile*, Pergamon Press, New York, 1957.

Marcos, F.A., and E.R. Swift, "Application of the Satellite Triaxial Accelerometer to Atmospheric Density and Wind Studies," AFGL-TR-82-0091, ADA120852, 1982.

Mayr, H.G., I. Harris, and N.W. Spencer, "Some Properties of Upper Atmosphere Dynamics," *Rev. Geophys. Space Phys.*, **16:** 539–566, 1978.

McLean, G.S., "The Jet Stream and Associated Turbulence," in *Winds for Aerospace Vehicle Design*, Sissenwine and Kasten, editors, AFCRL-62-273(I), 1962.

Meriwether, J.W., C.A. Tepley, F.A. Price, P.B. Hays, and L.L. Cogger, "Remote Ground-based Observations of Terrestrial Airglow Emissions and Thermospheric Dynamics at Calgary, Alberta," *Opt. Engr.*, 1982.

NOCD (Naval Oceanography Command, Detachment), *Guide to Standard Weather Summaries and Climatic Services*, NAVAIR 50-1C-534, Asheville, N.C., 1980.

Quegan, S., G.J. Bailey, R.J. Moffett, R.A. Heelis, T.J. Fuller-Rowell, D. Rees, and R.W. Spiro, "A Theoretical Study of the Distribution of Ionization in the High Latitude Ionosphere and the Plasmasphere: First Results on the Midlatitude Trough and the Light-Ion Trough," *J. Atmos. Terr. Phys.*, **44:**619, 1982.

Rees, D., T.J. Fuller-Rowell, and R.W. Smith, "Measurements of High-Latitude Thermospheric Winds by Rocket and Ground-Based Techniques and Their Interpretation using a Three-Dimensional Time-Dependent Dynamical Model," *Planet. Space Sci.*, **28:** 919, 1980.

Rees, D., T.J. Fuller-Rowell, R. Gordon, T.L. Killeen, P.B. Hays, L. Wharton, and N. Spencer, "A Comparison of Wind Observations of the Upper Thermosphere from the Dynamics Explorer Satellite with the Predictions of a global Time-Dependent Model," *Planet. Space Sci.*, **31:** 1299–1314, 1983.

Reiff, P.H., R.W. Spiro, and T.W. Hill, "Dependence of Polar Cap Potential Drop on Interplanetary Parameters," *J. Geophys. Res.* **86:** 7639–7648, 1981.

Rieger, E., "Neutral Air Motions Deduced from Barium Release Experiments. 1. Vertical Winds," *J. Atmos. Terr. Phys.*, **36:** 1377, 1974.

Richmond, A.D., and S. Matsushita, "Thermospheric Response to a Magnetic Substorm," *J. Geophys. Res.*, **80:** 2839–2850, 1975.

Rishbeth, H. "Thermospheric Winds and the F-Region: A Review," *J. Atmos. Terr. Phys.*, **34:** 1–48, 1972.

Roble, R.G., "The Thermosphere," in *Physics of the Upper Atmosphere and Magnetosphere*, National Academy of Sciences, Washington, D.C., **68:** 1977.

Roble, R.G., "Dynamics of the Earth's Thermosphere," *Rev. Geophys. Space Phys.*, **21:** 217–233, 1983.

Roble, R.G., R.E. Dickinson, and E.C. Ridley, "Seasonal and Solar Cycle Variations of the Zonal Mean Circulation in the Thermosphere," *J. Geophys. Res.*, **82:**5493–5504, 1977.

Roble, R.G., R.E. Dickinson, and E.C. Ridley, "Global Circulation and Temperature Structure of Thermosphere and High-Latitude Plasma Convection," *J. Geophys. Res.*, **87:** 1599–1614, 1982.

Roble, R.G., R.E. Dickinson, E.C. Ridley, B.A. Emery, P.B. Hays, T.L. Killeen, and N.W. Spencer, "The High Latitude Circulation and Temperature Structure of the Thermosphere Near Solstice," *Planet. Space Sci.*, **31:** 1479–1499, 1983.

Rottger, J., "VHF Radar Observations of a Frontal Passage," *J. Appl. Meteorol.*, **18:** 85–91, 1979.

Scoggins, J.R., and W.W. Vaughan, "Cape Canaveral Wind and Shear Data (1 through 80 km) for Use in Vehicle Design and Performance Studies," *Tech. Note D-1274*, NASA, 1962.

Shellard, H.C., "The Estimation of Design Wind Speeds, Win Effects on Buildings and Structures," *Nat'l Phys. Lab. Symp., Teddington, England*, **16:** 30–51, 1965.

Sherlock, R.H., "Variation of Wind Velocity and Gusts with Height," Paper No. 2553, *Proc. Am. Soc. Civil Eng.*, **1:** 463–508, 1952.

Sherlock, R.H., "Gust Factors for the Design of Buildings," *Int. Assoc. for Bridge and Structural Engineering*, **8:** 207–235, 1947.

Sipler, D.P., and M.A. Biondi, "Midlatitude F-Region Netural Winds and Temperatures during the Geomagnetic Storm of March 26, 1976," *J. Geophys. Res.*, **84:** 37–40, 1979.

Sipler, D.P., B.B. Lukkala, and M.A. Biondi, "Fabry-Perot Determinations of Mid-Latitude F-Region Neutral Winds and Temperatures from 1975 to 1979," *Planet. Space Sci.*, **30:** 1025–1032, 1982.

Sissenwine, N., P. Tattelman, D.D. Grantham, and I.I. Gringorten, "Extreme Wind Speeds, Gustiness, and Variations with Height for MIL-STD-210B," AFCRL-TR-73-0560, AD774044, 1973.

Spencer, N.W., R.F. Theis, L.E. Wharton, and G.R. Carignan, "Local Vertical Motions and Kinetic Temperature from AE-C as Evidence for Aurora-Induced Gravity Waves," *Geophys. Res. Lett.*, **3:** 313, 1976.

Spencer, N.W., L.E. Wharton, H.B. Niemann, A.E. Hedin, G.R. Carignan, and J.C. Maurer, "The Dynamics Explorer Wind and Temperature Spectrometer," *Space Sci. Instr.*, **5:** 417–428, 1981.

Spencer, N.W., L.E. Wharton, G.R. Carignan, and J.C. Maurer, "Thermosphere Zonal Winds, Vertical Motions and Temperature as Measured from Dynamics Explorer," *Geophys. Res. Lett.*, **9:** 953–956, 1982.

Straus, J.M., "Dynamics of the Thermosphere at High Latitudes," *Rev. Geophys. Space Phys.*, **16:** 183–194, 1978.

Tattelman, P., "Surface Gustiness and Wind Speed Range as a Function of Time Interval and Mean Wind Speed," *J. Appl. Meteorol.*, **14:** 1271–1276, 1975.

Volland, H., "Models of Global Electric Fields Within the Magnetosphere," *Ann. Geophys.*, **31:** 154–173, 1975.

Volland, H., "Semiempirical Models of Magnetospheric Electric Fields," in *Quantitative Modeling of Magnetospheric Processes*, Geophys. Monogr. Ser., Vol. 21, edited by W.P. Olson, 261-280, American Geophysical Union, Washington, D.C., 1979a.

Volland, H., "Magnetospheric Electric Fields and Currents and Their Influence on Large Scale Thermospheric Circulation and Composition," *J. Atmos. Terr. Phys.*, **41:** 853–866, 1979b.

Wu, S.T., S. Matsushita, and L.L. DeVries, "An Analysis of the Upper Atmospheric Wind Observed by Logacs," *Planet. Space Sci.*, **22:** 1036, 1974.